CHAPTER 2

SOIL USED IN THE INVESTIGATION

2.1 Geological Origin of the Material and Mineralogy

2.1.1 Origin of the material

The soil used in the experiments was artificially prepared (dry side statically compacted) powder obtained from natural Boom clay taken from a location 223 m below surface at the HADES underground laboratory (SCK·CEN experimental repository) at Mol in Belgium. The Boom clay arrived at the laboratory in two sealed barrels of approximately 100-kg capacity in the form of a greyish powder at a hygroscopic humidity of approximately 3%. The clayey soil arrived in a destructured state, which is observed because the initially intact sample has been submitted to large deformations that have broken the original structure.

The Tertiary Boom clay formation is the youngest of a sea sediment sequence, which were deposited in the northern European sedimentary province over the EN of Belgium and the whole on- and off-shore area of The Netherlands during the Middle Oligocene (Rupelian age), 30 million years ago (Horseman *et al.*, 1987). The marine clays were formed during one of the successive transgressional phases and subsequent regressions, which were believed to be the result of tectonics movements during the Tertiary (Schokking and Nooy van der Kolff, 1995). The clays were formed in water depths less than 150 m (Letsch and Sissingh, 1983 in Schokking and Nooy van der Kolff, 1995) with an assumed average thickness of this sequence of approximately 100 m. At the end of the Oligocene a major uplift occurred causing erosion of the last deposits and the Boom clay in large areas. Following the Boom clay sequence a cover of late-Oligocene, Miocene and Pliocene sandy deposits were laid down in approximately the same area of clay occurrence. Fig. 2.1 shows the distribution of the Boom clay formation and the position of SCK·CEN site at Mol, where the clay lies at about 160 m below surface under the Antwerp sandy formation, has a thickness of approximately 110 m and dips 1% to 2% (Heremans, 1980 in Horseman *et al.*, 1987). Boom clay units, predominantly consisted of mixed clay and silt, characterised by its stratigraphy, lithostratigraphy and on basis of geotechnical properties have been described by Vandenberghe (1978) (referred in Horseman *et al.*, 1987). The clay sequence is characterised by the presence of beds containing levels of carbonates (calcareous concretions of septarian limestone nodules) and also pyrite and marcasite concretions, as well as a fraction of organics (Vandenberghe and Laga, 1986 in Volckaert *et al.*, 1994; Horseman *et al.*, 1987). The clay fissuring observed near surface and which reduces with burial depth, is thought to be due to stress relief during tectonic uplift and subsequent erosion (Schokking and Nooy van der Kolff, 1995).

The in situ pore water chemistry of the sodium bicarbonate type, which is slightly basic (pH = 8.2-8.5), is dominated by sodium cation Na^+ (12.6 mmol/l) and in lesser content by K^+, Ca^{2+} and Mg^{2+} cations, with concentrations of 0.20 mmol/l, 0.05 mmol/l and 0.10 mmol/l respectively (Griffault *et al.*, 1994). The main anions are carbonates and in lesser concentration chloride ions (0.5 mmol/l) (Griffault *et al.*, 1994). The total alkalinity is 12 mmol/l. It is believed that after the uplift and subsequent erosion the saline pore water of the marine deposits has been replaced by fresh water, and in the following transgressional period saline interstitial fluid has again been infiltrated along the fissures developed during uplift. In general, decreasing salt content with depth is observed, probably related to a decrease in fissure density (Schokking and Nooy van der Kolff, 1995).

The cation concentrations of the pore water reported in Griffault *et al.* (1994), as well as the synthetic interstitial water composition used in SCK·CEN experiments (RESEAL Project Report, 1997), allow to estimate the sodium adsorption ratio (SAR) of the in situ equilibrium solution, which is

approximately SAR = 33 $(meq/l)^{1/2}$. The proportion of sodium in the adsorbed layers can also be estimated from the previous value, being the exchangeable sodium percentage (ESP) around 33% according to Sherard *et al.* (1972) plot, thus showing demixing of cations (sodium and calcium ions separate into distinct regions) in the interlayer exchange sites (Mitchell, 1993).

One-dimensional consolidation tests on block samples taken at 247 m reported by Horseman *et al.* (1987) showed that compression curves cross their corresponding ICL (intrinsic compression line) and attain their yield point before reaching the SCL (sedimentation compression line), thereafter dropping towards the ICL and appearing to join the extension of it. The ICL of a reconstituted clay at a water content equal or greater than the liquid limit and the SCL of the natural sedimentation curve are defined as proposed by Burland (1990). The in situ state at 247 m corresponding to a vertical effective stress of 2.5 MPa (Horseman *et al.*, 1987) lies between the ICL and the SCL, suggesting that the soil is slightly overconsolidated (Burland, 1990). Horseman *et al.* (1987) reported an OCR_v of circa 2.4 at the sampling elevation in the experimental repository, stating the difficulty of reconciling this preconsolidation pressure of 6.0 MPa with geological evidence. This evidence indicates only limited preloading, which is attributed to the erosion of about 40 m in the Antwerp area during the Pleistocene (Horseman *et al.*, 1987; Schokking and Nooy van der Kolff, 1995). The excess is attributed by Horseman *et al.* (1987) due to creep and diagenesis mechanisms. However, the position of yield points with respect to SCL, suggest that fabric and bonding mechanisms are not of major significance (Burland, 1990). Schokking and Nooy van der Kolff (1995) have suggested that this lost of structure could be due to swelling caused by stress relief and infiltration of NaCl (cation exchange of Na^+), when during the latest transgressional periods the fresh pore-water was replaced by saline water.

2.1.2   X-ray diffraction analysis

To qualitatively characterise the mineralogical composition of the material used in this research, an X-ray diffraction analysis (Willard *et al.*, 1974) has been performed on air-dried randomly oriented powdered sample of a representative silt/clay size fraction of the soil (first passing No.200-75 µm and then ground to a finer powder). The equipment is a D-500 Siemens diffractometer with CuK anode (incident radiation wavelength of $\lambda = 1.5406$ Å) with a step size of 0.05°, a scan speed of 3°/min, and a starting value of $2\theta = 3.976°$ up to 69.976°. Powder specimen containing particles randomly orientated at all directions insures that some will be properly oriented with respect to the X-ray beam to produce a characteristic set of continuous reflections (both first and higher orders) and at values of θ (angle of the diffracted rays) corresponding to the basal spacing of the prominent planes. Since no minerals have the same spacing of basal planes (d), the angle θ at which diffraction occurs (which is related to the distance d by Bragg's law: Mitchell, 1993; Yong and Warkentin, 1975) is used for identification, being the diffraction pattern a 'fingerprint' of the crystalline components. Details of specimen mounting and general instructions for the operation of the diffraction unit are described in Willard *et al.* (1974).

The complete X-ray diffraction patterns, consisting in a series of reflections of different intensities (expressed in counts) and θ values, is presented in Fig. 2.2. A computer program, with a file of patterns for known materials, identified the first order most intense basal reflections related to the (001) spacing (7, 10 or 14 Å), as well as the higher order reflections, which are characteristics for the different clay mineral groups constituting the powdered sample. The most intense reflections for minerals found in the powdered sample of Boom clay are also indicated in Fig. 2.2, where the following clayey mineralogical components can be identified: kaolinite ($d_{(001)} \approx 7.2$ Å), illite ($d_{(001)} \approx$ 10 Å) and muscovite, as well as the following non-clayey minerals: quartz, microcline (potassium feldspar) and orthoclase, characteristics of the weathering of acid rocks. In a first attempt of characterisation, the mineral gismondine and merlinoite of the zeolite group were also identified, but they were disregarded because they are formed from basic rock weathering, which is not the case of the Boom clay formation.

2.1.3 Mineralogy

The mineral composition obtained from different studies is summarised in Table 2.1. It can be seen that the clay mineralogy for the distinct samples differs considerably from one report to another. Independently from test repeatability and reproducibility, the clay spatial variability with depth has also been accounted for by Horseman *et al.* (1987), where the mineralogy of a sample for a depth of 247 m differed considerably from that reported in the Beer *et al.* (1977) (referred in Horseman *et al.*, 1987) for the clay at 220 m at the same site. These variations appear to be due to lithological and stratigraphic differences of the various geotechnical units identified for the Boom clay formation. Nevertheless to what previously is outlined, it seems that the dominant composition of the clay fraction, which represents 65% to 70% of weight of the total solids, is the kaolinite / mica group (kaolinite / illite minerals with 27% to 48% of total solids weight), with some interstratified or alternate random (disordered) or regular (ordered) stacking of two mineral layers having properties intermediate between the components: bravaisite (interstratified smectite / illite with 10% to 35% of total solids weight) and interstratified chlorite / smectite (max. 10% of total solids weight). In addition, the non-clayey fraction is dominated by quartz (15% to 25%) with other components: pyrite (< 5%), microcline (potassium feldspar: < 5%), plagioclase (calcium-sodium feldspar: < 5%) and calcite (< 5%). The presence of gypsum reported by ANDRA 1993 (Rhattas, 1994) and sulphates by CEE-Project ARCHIMED (Griffault *et al.*, 1994) makes evident the oxidation of the pyrite FeS_2 to form SO_4^{2-} (Mitchell, 1993).

Analytical characterisation of the Boom clay powder has been reported applying X-ray fluorescence method with the following identified components (% in dry weight; Robinet *et al.*, 1996b): SiO_2 (57.58 %), Al_2O_3 (12.93%), Fe_2O_3 (7.57%), CaO (2.22%), MgO (2.40%), Na_2O (0.12%), K_2O (1.96%), MnO (0.01%), TiO_2 (0.88%), P_2O_5 (0.18%). Chemical composition in % dry weight is also reported in Griffault *et al.* (1994).

2.2 Classification and Geotechnical Characteristics of Clay Powder and Packings

2.2.1 Geotechnical classification tests

2.2.1.1 *General tests on clay powder and clay packings*

A number of general geotechnical tests have been carried out in order to characterise the properties of the clay powder and different soil packings used in this study:
- particle size distribution analysis
- specific gravity of soil particles
- specific surface of soil particles
- consistency limits
- pore water extraction (squeezing technique)
- static compaction tests
- soaking under constant vertical load (conventional oedometer cell)
- resonant column tests
- pore size distribution analysis

The first three analysis were carried out to describe Boom clay destructured powder (apparent particle size, grain specific gravity and specific surface) characteristics. Consistency tests are more representative of a

Table 2.1 Mineralogy of Boom clay (all values in % weight of the total solids).

British Geological Survey; Horseman *et al.* (1987)

Clay minerals: ≈ 70 %			Other minerals: 30 %
Kaolinite	Smectite	Mica[a]	Quartz
29 %	22 %	19 %	30 %

[a] The mica fraction can probably be equated with illite, but chemical analysis would be necessary to confirm its presence

ISMES; Pellegrini *et al.* (1989)

Clay minerals: 60-70 %					Other minerals: 30-40 %		
Kaolinite	Illite	Chlorite	Smectite	Interstrat.[b]	Quartz	Feldspar	Organic
20-25 %	20-25 %	5-10 %	≥5 %	≤5 %	20-25 %	≥5 %	5-10 %

[b] Chlorite/vermiculite and/or smectite type

ANDRA 1993; Rhattas (1994)

Clay minerals: 65-70 % [c]				Other minerals: 30-35 %					
Kaolinite	Illite+mica	Interstrat. illite/smectite	Chlorite	Quartz	Micro-cline	Plagio-clase	Pyrite	Siderite	Gyp-sum
16-17 %	11-12 %	35-38 %	3-4 %	15-20 %	5 %	< 5 %	< 5 %	< 5 %	5 %

[c] Values of the clayey fraction are converted to % weight of the total solids

CCE-Project ARCHIMED; Robinet *et al.* (1996b)

Clay minerals: ≈ 65 % [d]					Other minerals: ≈ 35 %					
Kaolinite	Illite+ mica	Interstrat disorder. illite/ smectite	Interstrat Ordered Illite/ smectite	Chlorite	Quartz	Micro-cline	Plagio-clase	Pyrite	Carbo-nate	Sul-phate
13 %	16 %	33 %	Traces	traces	20-25%	4-5 %	4-5 %	4-5 %	traces	traces

[d] Values of the clayey fraction are converted to % weight of the total solids

Final Report EUR 16744 EN; Volckaert *et al.* (1996a)

Clay minerals: ≥ 60 %					Other minerals: ≤ 40 %				
Kaolinite	Illite	Smectite	Interstrat. Chlorite/ Smectite	Interstrat. illite/ smectite	Quartz	Feldspars	Pyrite	Calcite	Organic carbon
20-30 %	20-30 %	10-20 %	5-10 %	5-10 %	20 %	5-10 %	1-5 %	1-5 %	1-5 %

Laboratoire de Géomécanique du BRGM; Lagny (1996)

Clay minerals: ≈ 75 % [e]				Other minerals: ≈ 25 %			
Kaolinite	Chlorite	Interstratified Disordered illite/smectite	Illite+mica and interstrat. Ordered illite/smectite	Quartz	Carbonate	Microcline	Plagioclase
19 %	10 %	24 %	22 %	20 %	< 2 %	traces	infratraces

[e] Values of the clayey fraction are converted to % weight of the total solids

remoulded state, obtained when thoroughly mixing at a water content greater than the plastic limit with sufficient mechanical energy to reduce the clay strength to a minimum. Pore water extraction (presented in section 2.2.2), which is also determined at a remoulded state, is related to the measurement of the soluble salt contents, which at the same time is associated with the osmotic suction of the soil. The four remaining tests, which are presented in the following sections, refer mainly to the characterisation of the different artificially prepared soil packings used in this research.

2.2.1.2   *Clay powder and remoulded state characterisation*

Particle size distribution, both sieve analysis and sedimentation process (ASTM D422), have been done for a basic understanding of the nature of the soil powder. Sedimentation analysis is effective for separating soil fractions from 74 μm down to a size of about 200-500 nm. Particle size description, mainly related to the particle aggregation, is complemented with scanning electron micrographs at ×5000 enlargement (refer to section 2.5.6). Due to the fact that the soil is mostly clay and silt size, special care was taken to the dispersion of the sample. Fig. 2.3 shows the result of Boom clay particle size distribution compared to that obtained from different studies using conventional techniques (Baldi *et al.*, 1988; Lagny, 1996; Wan, 1996) and laser granulometry (Rhattas, 1994; Lagny, 1996). The contrast observed between the distributions are thought to be due to the different chemical (dispersing agent) and mechanical (dispersion device) treatments given to powder prior to the sedimentation analysis in order to cause the breakdown of the aggregates. These differences are more marked for sizes lower than 20 μm. Particle size curves reported by instruments utilising laser light interaction with suspended soil particles based on diffraction patterns tend to lie bellow curves determined by sedimentation process, according to results presented by Vitton and Sadler (1997), which is the general trend observed in Fig. 2.3 for particle sizes smaller than 10 μm. In general, it can be seen that the clay is well graded with a $C_u = D_{60}/D_{10} \approx 7$, which indicates that the grain size distribution extends over a wide range. The effective size of the soil is $D_{10} \approx 1$ μm for predominantly flocculated particles and around 100 nm for predominantly dispersed states. The clay size content (< 2 μm) varied between $(22 \pm 4)\%$ for the apparently flocculated particles and $(54 \pm 5)\%$ for the dispersed states.

The different granulometric cumulative distribution results presented in the previous figure were digitised [log x_i, f(log x_i)], where x_i represents the midpoint of each class width corresponding to the apparent particle size and f(log x_i) the density function, and subsequently interpolated to curve-fit these data points in order to obtain the particle size density function, which is represented in Fig. 2.4. The relative particle size density function can be approximated following a procedure similar to that described in Eq. (2.16) for the pore size density function. In spite of the fact that some curves show a monomodal common trend, purportedly related to a dominant flocculated state of the particles corresponding to an apparent particle size of 4 μm - 6 μm, it is possible to identify a bimodal tendency with a dominant particle size at a colloidal state of 0.6 μm (similar to that of kaolinite size: 0.3 μm to 1 μm) and in lesser proportion at a size of approximately 5 μm. Clay size particles are generally defined as particles less than 2 μm. However, in some cases, particles between 2 μm and 5 μm in size are also referred to as clay size (ASTM D653). These cases correspond to the aggregation or flocculation of individual dispersed particles into submicroscopic units or flocs, which are formed during the random motion of the sedimentation process as the particles come close to each other. The effects of concentrations of soluble salts on flocculation, despite the use of a dispersant in sedimentation analysis, has been investigated by Picornell *et al.* (1990).

The specific gravity of the soil grains at 20°C is $Gs = 2.70$, determined according to ASTM D854. Other results reported by different studies varied between: 2.65 (Final Report EUR 16744 EN), 2.67 (Rhattas, 1994; Robinet *et al.*, 1996b) and 2.70 (Lagny, 1996; Horseman *et al.*, 1987).

The specific surface S_S for the Boom clay powder estimated using mercury intrusion porosimetry data presented in section 2.5 is indicated in Fig. 2.5. The calculation of S_S values from porosimetry data assumes cylindrical shape pores applying Eq. (2.12), which relates the apparent pore diameter d with the

applied total pressure p (refer to section 2.5.1). The incremental intruded volume normalised by sample dry weight dV, represented in Fig. 2.19, can be related to the incremental specific surface dS_S by means of the following expression:

$$dS_S = \frac{4dV}{d} = -\frac{pdV}{\sigma_{Hg}\cos\theta_{nw}} \quad ; \quad S_S = -\frac{1}{\sigma_{Hg}\cos\theta_{nw}} \int_0^{Vmax} pdV \qquad (2.1)$$

where σ_{Hg} is the surface tension of the mercury, θ_{nw} the contact angle between mercury and the pore wall and V_{max} the maximum intruded volume normalised by sample dry weight (0.330 cm^3/g for the low-density packing and 0.201 cm^3/g for the high-density fabric). S_S values varied between 18.7 m^2/g for the γ_d = 13.7 kN/m^3 packing and 22.8 m^2/g for the γ_d = 16.7 kN/m^3 packing as observed in Fig. 2.5.

Mercury intrusion technique reports lower specific surface values than nitrogen sorption methods due to the limit accessibility of the apparatus to penetrate the smallest pores in a sample (apparent pore sizes less than 6 nm cannot be intruded). Volckaert *et al.* (1996a) reported a value of S_S = 40 m^2/g and Baldi *et al.* (1988) a value for the primary specific surface of S_S = 52.5 m^2/g and for the secondary specific surface of S_S = 177 m^2/g, the last one corresponding to the value indicated by Horseman *et al.* (1987). Robinet *et al.* (1996b) suggested a value of S_S = 42 m^2/g using BET technique. It appears that a reasonable value for the specific surface could be S_S = 40 m^2/g, which corresponds to an intermediate value between a kaolinite mineral (S_S = 10 to 20 m^2/g) and an illite mineral (S_S = 80 to 100 m^2/g) (Lambe and Whitman, 1979).

The cation exchange capacity reported by the Final Report EUR 16744 EN (Volckaert *et al.*, 1996a) is CEC = (30±4) meq/100g, while Robinet *et al.* (1996b) suggested a basic or actual CEC of 59 meq/100g and a total or potential CEC of 213 meq/100g. Griffault *et al.* (1994) indicated CEC values of (28±4) meq/100g with an estimated ESP of 32%.

Consistency limits were also investigated for the remoulded clay powder following ASTM D4318, due to its related patterns with other soil properties, such as compressibility, swelling and shrinking potentials. The liquid limit and plasticity indices were determined to be w_l = (55.7 ± 0.9)% and PI = (26.9 ± 1.0)%, respectively. Fig. 2.6 shows the plasticity chart, which includes consistency results reported by different studies. In general, great scattering of results can be seen between the different reconstituted states obtained in laboratory, which are believed to be due to the influence of structure changes upon remoulding (dispersed or flocculated states), as well as the effect of exchangeable cations (substitution of divalent for monovalent cations) and salt concentrations on interparticle forces, which have a prominent role in the determination of the liquid limit (Yong and Warkentin, 1975; ASTM D4318). Usually for kaolinite the liquid limit decreases with increasing pore water concentration and increasing dielectric permittivity (Santamarina and Fam, 1995), but at pH = 10 an opposite trend has also been reported (Warkentin, 1961 in Santamarina and Fam, 1995). However, part of this experimental scatter may also be due to methods of measuring the liquid limit (fall-cone test or brass cup; Casagrande or ASTM grooving tool). The Boom clay powder can be classified according to the plasticity chart as a high-medium plastic inorganic clay (CH) (Unified Soil Classification System, ASTM D2487).

The destructured Boom clay powder has an estimated dry unit weight of 10.8 kN/m^3 (e = 1.459). The hygroscopic humidity at a laboratory relative humidity of 47% (corresponding to a total suction of $\psi \approx$ 102 MPa) is around 3.0%, which corresponds to a residual degree of saturation of 5.6% and around 6 Å Stern layer of strongly adsorbed water (refer to section 5.1.1).

2.2.2   Pore water extraction by squeezing technique. Osmotic suction measurement

2.2.2.1   General aspects and experimental procedure

There are several techniques available for pore water extraction for the purpose of determining the amount of soluble salts present in the extracted liquid, which include the saturation extract method, immiscible liquid displacement or gas extraction method and the mechanical squeezing method (Iyer, 1990). The selected procedure for squeezing free pore water was followed according to a similar methodology to that proposed by ASTM D4542. The difference with the standard procedure is that a conductometer has been used instead of the refractometer and that a much lower pressure is applied to the sample (low-pressure mechanical squeezing system). The electrical conductivity of the pore bulk liquid can be used to approximately indicate the total concentration of dissolved salts, which at the same time is related to the osmotic suction of the soil by means of the van't Hoff equation for dilute solutions (Castellan, 1971). Kayyal and Mohamed (1997) have recently used the electrical conductivity method for the determination of the ionic strength and equilibrium concentrations of heavy metals.

Distilled water with an electrical conductivity of 2.9 ± 0.1 µS/cm at 25°C and pH = 5.98 ± 0.02, obtained by filtration and ion exchange resins, was thoroughly mixed with Boom clay powder at an initial hygroscopic humidity of 3% to obtain a plastic state (over the plastic limit) by bringing the water content to 34%, which is related to the storage capacity of the high-porosity packing ($\gamma_d = 13.7$ kN/m³). The addition of excessive water to bring the sample to a nearly reconstituted state, so that an increased amount of liquid can be expelled, may result in the leaching of salts present in the soil with the consequent distortion of the original salt content. The target water content corresponds to a degree of saturation of approximately 63% for the remoulded clay powder, which is assumed to be related to a dry unit weight of $\gamma_d \approx 10.8$ kN/m³.

It is supposed that in the dry Boom clay powder adsorbed cations are tightly held by the negatively charged clay particles in the strongly attracted adsorbed water corresponding to the hygroscopic humidity. Cations in excess of those needed to neutralise the electronegativity of the clay surface and associated anions are present as salt precipitates (Mitchell, 1993). Upon wetting this precipitated salts go into the free solution contained at inter-aggregate level, which is mainly the pore-water being extracted by squeezing technique. Because the adsorbed cations produce a much higher concentration near the adsorbed surface of the clays, estimated in 2.5 to 5.0 M (Bolt, 1956; Iwata *et al.*, 1995), they try to diffuse away in the intra-aggregate level in order to attempt to equalise concentrations throughout. The escaping tendency due to diffusion at this level is restricted by the negative electrical field originated at particle surfaces, which acts as a restrictive semipermeable membrane separating regions of high concentrations midway between particles at intra-aggregate level and low concentrations zones in the equilibrium solution surrounding the peds. The difference in osmotic pressure between these regions is further discussed in section 7.1.1.3.

The pore-water has been extracted using the heavy-walled compaction mould indicated in Fig. 3.4. The air pressure release valve of the piston squeezer is connected to a detachable syringe, where the extracted fluid is collected. Between the piston and the soil a Whatman 42 ashless filter paper ($\varnothing$ 55 mm) and a perforated stainless steel plate with 15 µm pore size were placed, the latter acting as the filter paper support. All these mechanical components were carefully rinsed with distilled water and then air-dried. The remoulded soil sample of approximately 100 g was placed into the cylinder and then covered by the filter paper and the perforated plate. Vertical stress was applied gradually to a maximum of 10 MPa and held for 48 hours until no more water was expelled. The final water content of the specimen was 10.9% with a dry unit weight of 20.5 kN/m³. The amount of water expelled was approximately 15 ml, remaining some quantity in the effluent passage. The procedure was repeated three times in order to collect a representative amount of pore water. The extracted yellow liquid was filtered with a vacuum pump system up to -80 kPa and an ultra-fine previously washed and oven dried Whatman GF/C glass fibre paper filter with retention down to less than 10 µm, in order to retain colloidal flocculated clay particles which could alter conductivity readings. The dry residual of the

filtered liquid was estimated by oven drying at 110°C in 8.33 ppt (g of Σcations + Σanions + Σcolloids + Σcolloidal organic matter - ½ HCO_3^- in 1 kg of water). The yellow colour of the extracted liquid is probably related to the colloidal organic matter. The extracted liquid was observed in a polarising microscope and some colloidal size particle aggregates of 20 μm × 12 μm were detected, being the most representative size of 10 μm × 10 μm.

Calibration curves for different homoionic NaCl salt solutions, prepared as indicated in section 4.1.2 for vapour equilibrium technique, were used to determine the relationship between electrical conductivity outputs and electrolyte concentration in meq/l or ppt. Fig. 2.7 presents this relationship ranging from a solute concentration of 2.13 meq/l to 687 meq/l (0.124 ppt to 38.7 ppt), compared to that presented by Davis and De Wiest (1966), for heteroionic systems. In general, a good agreement is obtained between both curves. According to equations presented in section 4.1.2 the activity of the electrolytic solution can be related to the total suction, which in absence of soil matrix, is only associated with the osmotic component. In this way, a calibration curve that relates electrical conductivity and osmotic suction is presented in Fig. 2.7 for the NaCl solution. This curve is compared with the calibration curve proposed by the USDA Agricultural Handbook No. 60 (1950) (referred in Fredlund and Rahardjo, 1993) for a heteroionic system, showing a quite good agreement.

2.2.2.2 *Experimental results*

The electrical conductivity of the pore water from the soil was (10.11 ± 0.06) mS/cm at 25°C with an pH = 7.64 ± 0.02. The proportion electrical conductivity / dry residual is approximately 1.21 μS/(cm.ppm), which is in accordance with normal values in groundwater (Custodio and Llamas, 1983). An estimation of the concentration of the dissolved salts (cations and anions) of the liquid, based on the electrical conductivity-salinity apparatus calibration curve, is approximately 5.8 ppt (g contained in 1 kg of water) at 20.3°C. The salinity can also be expressed in terms of cation and anion normal concentration: approximately 94 meq/l (94 mmol/l or 5.43 ppt) according to the calibration curve for an homoionic solution of NaCl or 110 meq/l obtained from an empirical expression proposed in Davis and De Wiest (1966) for heteroionic systems, as indicated in Fig. 2.7.

The difference between the salinity and the dry residual of the filtered liquid, i.e. 2.53 ppt, gives an approximate indication of the colloidal concentration. The equivalent molarity of the free pore water is approximately 0.10 M admitting monovalent homoionic samples (Na^+ system) or 0.06 M for bivalent ions (Ca^{2+} system). These values will further be used to incorporate electrolyte concentrations in DDL theory (refer to section 7.1.1.3). The osmotic suction of this pore water containing mixtures of dissolved salts, estimated from the electrical conductivity and according to Fig. 2.7, is approximately $\pi = 443$ kPa obtained from the NaCl calibration curve and $\pi = 383$ kPa according to the USDA Agricultural Handbook No. 60 (1950) (referred in Fredlund and Rahardjo, 1993) for a heteroionic system.

A parallel study of the pore fluid has also been accomplished using SMI transistor psychrometers (refer to section 4.1.4). The osmotic suction of the extracted pore water was measured placing three drops of lixiviate over the suction probe cap, which was zeroed overnight with three drops of distilled water, following a similar process to that used in the calibration procedure and thus minimising the variables influencing the performance of the psychrometers. The average osmotic suction over eight measured values was (410 ± 25) kPa. Fig. 2.8 shows psychrometric and electrical conductivity results of osmotic suction, as well as the relationships between osmotic suction and soil water content obtained by Wan (1996) using the contact and non-contact filter paper technique, in this latter case calculating the osmotic suction as the numerical difference between the total and matric suctions. The measured psychrometric value, as well as the estimated one based on the electrical conductivity, is shown to agree closely with the total minus the matric suction measurements reported by Wan (1996). It can be seen that the osmotic suction appears to be independent of the water content in the range indicated in Fig. 2.8, and the scatter in the results are due to the accuracy of the filter paper technique and to the fact that total and matric suction were measured independently. This close agreement

consistent with other testing results on clays (Krahn and Fredlund, 1972) indicates the reliability of the pore liquid extraction for osmotic suction measurements, as well as certain support of the validity of matric and osmotic suctions being components of total suction. However, the concept of osmotic suction to be independent of water content is not adequate for high moisture levels, since the inter-aggregate concentration is usually accepted to be   proportionally related to the inverse of the corresponding free water content. Iyer (1990) has reported different values of pore water concentrations for the same soil using the saturation extract technique for different water contents and also different concentrations applying varying squeezing pressures, thus suggesting some variation of osmotic suction with soil water content. This author has pointed out that cation concentrations of the squeezed water at pressures less than 20 MPa, which is the case of the present study, remained more or less constant, becoming representative of the inter-aggregate and outer layers diffuse water. At higher squeezing pressures concentration decreased purportedly related to the mixing of the free pore water with the double-layer water.

The osmotic pressure can also be obtained by the van't Hoff equation (Castellan, 1971) admitting a dilute electrolytic solution:

$$\pi = RT\sum(c_i - c_o) = RT(c_i^+ + c_i^- - c_o^+ - c_o^-) \approx 250 \text{kPa} \tag{2.2}$$

where R is the molar gas constant, T the absolute temperature and $\Sigma(c_i-c_o)$ the molar concentration of the solute (both cations and anions) referred to that of pure water (estimated in 0.10 M for a monovalent homoionic species solution). However, this last expression valid only for ideal solutions reports a small value compared to the measured one.

It is also worth noting that the measured values of osmotic suctions are consistent with the range of swelling pressures reported in section 6.5.1 for the stable non-collapsible packings, as well as in Fig. 2.33, suggesting some applicability of the concepts of osmotic suction on compression, swelling behaviour and swelling pressure. This way, a maximum swelling pressure of approximately 0.4 MPa would be expected when imbibing a saturated Boom clay with demineralised water.

2.3   Static Compaction Tests and Powder Preparation Techniques for the Different Soil Structures used in the Experiments

2.3.1   Static compaction tests

2.3.1.1   Test procedures and results

Static compaction tests have been carried out in order to determine the maximum preconsolidation stress of soil structure fabrication at varying dry unit weight, water content and temperature. This way, compaction experiments in mixtures of powder and water can be used to obtain the compression yield loci for the different soil structures. A variable peak stress - constant stroke static compaction procedure has been followed. In this type of compaction, a variable static force is gradually applied to the soil mass confined in a rigid mould, until a specified final volume or dry unit weight is achieved under controlled water content (refer to Fig. 2.9). The force, which is applied by the movement of a piston in a strain-controlled press, varies depending on the water content, soil packing and temperature.

The procedure adopted can be described as follows:
- Air-dried powder under laboratory conditions with a hygroscopic humidity of 3% and passing No.40-425 μm is thoroughly mixed with water to achieve a predetermined water content and allow to stand for 48 h for moisture equilibration in plastic sealed bowls. Five different water contents have been taken: 3.0%, 9.8%, 14.7%, 18.7% and 22.3%.

- The different moist soils with a dry weight of approximately 60 g are charged into the hermetic compaction mould (d = 50 mm) and the heating chamber presented in Fig. 3.4 at the selected temperature (22°C or 80°C). The initial h/d relation is approximately 0.45, but upon advancing the piston it reduces to values less than 0.35, which ensures a low loss of energy input due to boundary friction. The greased mould is then used to compact the soil at a piston travel rate of 0.5 mm/min to the predetermined target volume. The entrapped air is progressively released by the air pressure valve, which is immediately closed in order not to lose water content, specially under high temperature. The force of compaction determined by a load cell and the corresponding piston travel are measured at different intervals of displacements. These readings give the force - stroke or net vertical stress - dry unit weight relationships for a specified water content, which are plotted in Fig. 2.9. Each curve terminates at a specific degree of saturation and when reaching nearly saturated states, the static compaction test is no longer possible and is stopped before the beginning of consolidation.

The information of Fig. 2.9 can be reorganised to interpret the relationship between compaction energy input per unit volume, dry unit weight and water content. The static compaction curves presented in Fig. 2.10 provide the relationships between dry unit weight and soil moisture for a specified temperature and net vertical stress. These results are obtained from Fig. 2.9 drawing vertical lines at the different net vertical stresses to read the target dry unit weights on the ordinate. The modified dynamic compaction test reported by Wan (1996) is also plotted in Fig. 2.10 for comparison. This modified Proctor test gives a maximum dry unit weight of 18.7 kN/m^3 and an optimum moisture content of 15.3%. It can be observed that the points corresponding to optimum conditions lie very close to the $S_r = 90\%$ degree of saturation line. The approximate energy input per unit volume is also presented in the previous figure. This energy can be evaluated from the area under the force - stroke curve up to the selected point at a certain water content and dry unit weight. According to section 6.1.2, the increment of work input per unit volume δW under K_0 condition can be written as the product of the net vertical principal stress (σ_v - u_a) with the work conjugate variable of vertical stress increment $\delta\varepsilon_v$. At a temperature of 80°C the values presented correspond only to the mechanical effect of the compaction process. Matric suction stress variable effects (u_a - u_w) with their work conjugate strain variable $G_s/(1+e).\delta w$, as discussed in section 6.1.2, are not considered since it is assumed that there is no water content variation in the hermetic mould during compaction. The incremental work input per unit volume δW can be approximately estimated as:

$$\delta W = (\sigma_{ij} - u_a \delta_{ij})\delta\varepsilon_{ij} \; ; \quad \delta W = (\sigma_v - u_a)\delta\varepsilon_v \approx (\sigma_v - u_a)_m\left(1 - \frac{\gamma_{do}}{\gamma_{df}}\right) \quad\quad (2.3)$$

where, (σ_v - u_a)$_m$ represents the average net vertical stress during the vertical strain increment, which can be estimated from the initial and final dry unit weights.

With respect to the modified dynamic compaction method, though apparently compacted to a constant energy level of the dropping weight estimated in 2.69 MJ/m^3, part of it is not used effectively for compaction because the soil bulges around the smaller head falling weight principally at a higher degree of saturation. In the case of the static compaction test, the entire soil mass is subjected to a displacement. However, this fact leads to the beginning of consolidation, and static compaction is difficult to achieve in the wet side of optimum. The Proctor compaction partially avoids this effect, since due to the nature of the test it hardly develops to a consolidation phase (Venkatarama Reddy and Jagadish, 1993). Fig. 2.10 indicates that the static compaction process is more efficient than the Proctor method, perhaps because of the higher energy losses associated with this last method. In this discussion, it is implicitly assumed that the energy losses due to boundary friction are similar in both cases. In addition, according the previous figure, it is observed that the dry unit weight change that experiences the soil under different water contents on the dry side in a dynamic compaction (with a standard compactive effort) is less than the corresponding one of a static compaction test with increasing compactive effort as it approaches maximum/optimum conditions. Standard Proctor energy of approximately 0.59 MJ/m^3 is also interpolated in the previous graph for 22°C and 80°C. However, this interpolation is expected to be somewhat shifted with respect to the Standard Proctor, due to the lower efficiency of this last method.

For equivalent compaction energy input per unit volume or for an equivalent net vertical stress, the dry unit weight reached by the hotter specimen is higher than the corresponding at 22°C for the same water content. This fact can be explained due to the viscosity reduction that experiences inter-aggregate water upon heating which affects the frictional resistance, joined to the decrease in the shearing strength of aggregate contacts. Consequently, there is a partial rearrangement of soil structure and a decrease in void ratio until additional contacts are formed to enable the soil to carry the net stresses at higher temperatures. Therefore heating up to a certain limit (≈ 80°C) acts like a lubricating agent, the same as the addition of moulding water, in order to permit the aggregates slip over each other and their movements to a more densely packed position.

Fig. 2.11 shows the compaction curves and the contours of equal suction. Total suction values higher than 3 MPa were determined from vapour equilibrium data and matric suction component were measured from suction controlled tests (refer to chapter 5). As observed, suction increases as water content reduces, being the high suction value lines with values $\psi \geq 3$ MPa nearly vertical. This indicates that at water content values less than approximately $w \approx 15\%$, increasing by compaction the dry unit weight (or in an equivalent form increasing the degree of saturation) does not change significantly the initial total suction value. This is because the loading mechanism affects the macroporosity that does not contain free water, since at these moisture content levels, water is mainly adsorbed or contained in the less bonded diffuse layers at intra-aggregate scale. This way, degree of saturation changes are associated with macroporosity changes under constant intra-aggregate water content. As matric suction values approach the saturation line, the loading mechanism affects inter-aggregate water and the contours of equal suction try to incline in order to converge to the limit condition of $(u_a - u_w) \rightarrow 0$ with $Sr \rightarrow 100\%$. Some small discrepancies are observed due to the different experimental techniques, but the general trend of suction contours in relation with compaction curves are similar to other test results reported by Gens *et al.* (1995) and Li (1995).

2.3.1.2   One-dimensional compression results in the lateral stress measuring system cell

2.3.1.2.1   Testing equipment and procedures

One-dimensional static compaction tests have also been investigated by means of the lateral stress measuring system cell described in section 3.2.3. With this equipment two soil packings at a target dry unit weight of 13.7 kN/m^3 and 16.7 kN/m^3 at a moulding water content of 15% were studied (refer to Fig. 2.10 and Fig. 2.11). The description of the oedometer ring and the calibration cycles for the automatic controlled system is detailed in section 3.2.3. The experimental setup for the compaction tests is presented in Fig. 4.19b. Special attention has been given to the piston travel rate of the strain-controlled compression machine in order not to exceed the response velocity required by the controlling equipment. The conducting system filled with high viscosity silicone oil (100 mm^2/s at 22ºC) induces some retard in the reception of the response action from the motor and the ram pump in order to attain the null strain condition imposed by the strain gauges system. This anomalous condition can be detected during vertical loading due to the fact that the net horizontal stress increment is lower than the expected value under K_{0nc} condition, because this state has probably not been achieved: $\delta(\sigma_h - u_a) < K_{0nc}\delta(\sigma_v - u_a)$. Thus, special care needs to be taken for the accurate measurement of K_{0nc}, since very small amounts of lateral movements can produce certain change in the apparent value of this parameter. The equipment adjustment to solve this problem demands low piston compaction rates. A piston travel rate of 0.4 mm/min has been selected at the beginning of the compaction test, but as the test progresses needs to be corrected in the range of 0.4 to 0.1 mm/min. During unloading the manual system of the press was used in order to achieve small vertical stress unloading steps in equilibrium with the corresponding net horizontal stress.

2.3.1.2.2   Testing results. Suction-preconsolidation stress relationships

Fig. 2.12 and Fig. 2.13 represent the stress paths followed during one-dimensional static compaction (loading and unloading) for the different target dry unit weights starting from a water content of 15% or from hygroscopic condition (only for the high-porosity fabric). The ratio of net horizontal to net

vertical stresses $K_0 = (\sigma_h - u_a)/(\sigma_v - u_a)$ is also plotted for the initial compression and the unloading path in terms of the vertical overconsolidation ratio. It can be seen K_{0nc} is found approximately constant during the monotonic initial compression: $K_{0nc} \approx 0.369$ for the high-porosity packing and a bit higher value $K_{0nc} \approx 0.390$ for the high-density fabric. The general trend of K_{0nc} slightly diminishing with higher porosity has also been observed by Ting *et al.* (1994) on remoulded and artificially sedimented samples. The low K_{0nc} measured values, which contrast with other reported values for remoulded and natural undisturbed saturated clays (Mesri and Hayat, 1993; Senneset and Janbu, 1994; Ting *et al.*, 1994), correspond to a dry side compacted soil composed of rigid and interlocked aggregates, which can support its own weight without needing to push sideways very much in order to prevent lateral movements. However, this load capacity diminishes with water content, tending to somewhat higher values of K_{0nc} near saturation, as indicated in Fig. 2.14 obtained from different test results involving static compaction results at constant water content and suction controlled main wetting and virgin compression results reported in chapter 6. This last trend has also been observed by Senneset and Janbu (1994) for different natural clays at varying water content and Machado and Vilar (1997) for suction controlled tests on lateritic soils. K_0 values for the slightly overconsolidated state corresponding to the in situ conditions are also presented based on estimated data reported by Horseman *et al.* (1987).

If it is supposed that soil behaves isotropically and elastically immediately when unloading, the following expressions apply:

$$\frac{\delta(\sigma_h - u_a)}{\delta(\sigma_v - u_a)} = \frac{\nu}{1-\nu} \; ; \quad K_0 = \frac{K_{0nc}(\sigma_v - u_a)_{max} - \delta(\sigma_h - u_a)}{(\sigma_v - u_a)}$$

$$K_0 = OCR_v K_{0nc} - (OCR_v - 1)\frac{\nu}{1-\nu} = \frac{\nu}{1-\nu} + \left(K_{onc} - \frac{\nu}{1-\nu}\right)OCR_v \tag{2.4}$$

where OCR_v is the vertical overconsolidation ratio and ν the Poisson's ratio. A deduced value of ν from one-dimensional unloading curves for $OCR_v < 2.5$ is approximately 0.19, according to curve fitting data presented in Fig. 2.12 and Fig. 2.13. Following Wood (1990), the elastic unloading path cannot be sustained beyond overconsolidation ratios higher than 2.5. For $OCR_v > 2.5$ another expression has been fitted for these unloading paths in the form of: $K_0 = K_{0nc}(OCR_v)^a$ (Schmidt, 1966). Mayne and Kulhawy (1982) and Mesri and Hayat (1993) proposed the exponent to be a function of the friction angle or the constant-volume friction angle: $a = \sin\phi'$. Curve fitting data is presented in the previous figures. Net horizontal stress relaxation observed under null net vertical stress in Fig. 2.12 and Fig. 2.13 are mainly attributed to incipient passive failure under a Mohr-Coulomb criterion.

Preconsolidation stresses or maximum fabrication stresses obtained for different total suction values and temperatures from static compaction results are plotted in Fig. 2.15 and Fig. 2.16. Total suction values have been estimated from retention curve data, based on vapour equilibrium tests, air overpressure technique and psychrometer results, as presented in chapter 5. Experimental data has been non-linearly fitted to an analytical expression equivalent to that proposed by Alonso *et al.* (1990) for the loading-collapse LC yield locus for isotropic compression. However, preconsolidation stress results are obtained from one-dimensional compression data, therefore the yield locus determined in this way is not the LC yield curve as originally defined. One-dimensional results can be converted to equivalent isotropic data based on a yield surface concept in the deviatoric, net mean stress and suction space. However, one-dimensional data has not been transformed into isotropic results in order to preserve the originally measured values and to the fact that this transformation does not introduce new aspects on the behaviour that is being outlined. Preconsolidation net mean stress has been evaluated assuming a constant value of $K_{0nc} \approx 0.380$ for both temperatures, according to previous results at 22°C. The extrapolation of this value for higher temperatures needs to be further investigated. The equivalent analytical expression applies in the following form:

$$\left(\frac{(\sigma_m - u_a)}{p^c}\right) = \left(\frac{(\sigma_m - u_a)^*}{p^c}\right)^{\frac{\lambda(0)-\kappa}{\lambda(\psi)-\kappa}} \quad ; \quad \lambda(\psi) = \lambda(0)\left[(1-r)e^{-\beta\psi} + r\right] \tag{2.5}$$

where $(\sigma_m - u_a) = ((\sigma_v + 2\sigma_h)/3 - u_a)$ represents the preconsolidation net mean stress, $(\sigma_m - u_a)^*$ the corresponding preconsolidation stress for saturated conditions, p^c a reference stress to normalise and make non-dimensional preconsolidation stresses, $\lambda(\psi)$ a compressibility parameter for changes in net mean stress ($\lambda(0)$ is the equivalent parameter for saturated conditions), ψ represents the total suction value, and r and β are parameters defining the maximum soil stiffness and the rate of soil stiffness increase with total suction, respectively. Some restrictions have been imposed to the following parameters, which have a clearly defined physical meaning: $\lambda(0) \leq 0.150$ and $0.01 \leq \kappa \leq 0.02$ according to previous experimental results reported in section 6.4. A constant reference value of $p^c = 0.10$ MPa has been selected (there is no appreciable change in the reported results if a $p^c = 0.01$ MPa value is also selected). Fig. 2.15 presents the originally measured values as determined from different test results for the 13.7 and 16.7 kN/m^3 packings, where curve fitting lines using an expression similar to Eq. (2.5) have also been plotted. Fig. 2.16 represents the converted mean stress values for different dry unit weights, based on the assumption previously stated. Numerical values reported by the non-linear curve fitting method for this last figure are presented in Table 2.2.

Table 2.2 Numerical values for the suction - mean preconsolidation stress curve fitting results.

T (°C)	γ_d (kN/m^3)	$(\sigma_m - u_a)^*$ MPa	$\lambda(0)$	κ	r	β (MPa^{-1})
	13.7	0.651	0.150	0.01	0.910	0.138
22	14.7	0.841	0.150	0.01	0.831	0.112
	15.7	1.271	0.150	0.01	0.819	0.112
	16.7	2.101	0.136	0.01	0.856	0.123
	13.7	0.601	0.150	0.01	0.919	0.138
80	14.7	0.734	0.150	0.01	0.826	0.139
	15.7	1.187	0.150	0.01	0.824	0.110
	16.7	1.949	0.135	0.01	0.849	0.125

The most sensitive parameter reflecting temperature and packing changes is the saturated net mean preconsolidation stress, according to the numerical values presented in the previous table and as expected from the previous figures. Static compaction results clearly show that the preconsolidation stress at a given suction for the same clay packing decreases with increasing temperature, possibly due to the inter-aggregate shearing resistance aspects pointed out in section 2.3.1.1. The general trend of decreasing preconsolidation stress with increasing temperature has also been observed for saturated sulphide clays by Eriksson (1989), for marine and lacustrine clays by Tidfors and Sällfors (1989) and for saturated Boom clay by Sultan *et al*. (1998). More experimental results concerning this aspect are presented in Fig. 6.70, where extrapolated data from static compaction tests are compared to suction controlled data at different dry densities.

2.3.2   Powder preparation techniques for the different soil structures

Following Mitchell (1993) the term structure refers to the combination of 'fabric' (arrangement of clayey particles) and inter-aggregate 'bonding'. Though the term 'packing' is generally referred to granular soils (Yong and Warkentin, 1975), it can be extended to characterise the fabric of clays composed of aggregates (dry side compacted), since such structure can be considered as a 'packing' of clay units or peds. Therefore, terms like fabric or packing are used to define without distinction the clay structure characterisation.

The testing program has included two main soil structures: high-porosity with collapsible tendency structure upon wetting at $\gamma_d = 13.7$ kN/m^3 and a low-porosity with swelling tendency upon wetting at $\gamma_d = 16.7$ kN/m^3, as suggested by the soaking under constant vertical load tests reported in section 2.6.1. The initial water content has been selected in 15%, which is a reasonable value for the workability of the clay powder on the dry side of optimum. In the same way, this humidity is not associated with an excessive initial suction value ($\psi \approx 2.3$ MPa), which does not involve a large suction change when applying the starting matric suction value of 0.45 MPa in the different equipment. In addition, this water content on the dry side ensures collapsible trends, which are more difficult to develop on the wet side.

Boom clay packings were obtained by uniaxial static compaction of clay powder with water homogeneously dispersed in it. The procedure adopted can be described as follows:
- Boom clay powder (passing No.40-425 µm) is left in equilibrium with the laboratory atmosphere with an average relative humidity of 47 % to achieve hygroscopic water content of approximately 3%.
- The clay powder is put in a controlled relative humidity room (up to 90%) to accomplish water content of approximately 9%.
- The humid clay powder is sprayed with a fine mist of demineralised water and afterwards water is thoroughly mixed in order to achieve the predetermined water content of (15.0 ± 0.3)%. The electrical conductivity measured with a salinity/conductivity system of the demineralised water, obtained by removing ions with cation and anion exchange resins, contained small amounts of dissolved salts (less than 9.5 µS/cm at 25°C or an estimated of less than 0.1 meq/l). This conductivity can be related to that of pure water to an equivalent osmotic suction of less than $\pi < 10$ kPa according to Fig. 2.7. The pH of the sprayed water measured with a pH/mV-meter is about 6.00±0.02, i.e. more acid than the in situ pore water chemistry.
- The mixed powder is passed through a No.10-2000 µm sieve in order to mechanically destroy the clods formed upon wetting. Mixing of the soil powder and water was carried out manually in batches of approximately 500 g.
- A 5-days curing time in sealed bags installed in a humid chamber (relative humidity of 90%) was adopted to ensure homogeneous conditions in the sample.
- The sample was then maintained in the hermetic mould presented in Fig. 3.4 at the selected temperature. This mould is then used to compress the soil at the predetermined dry unit weight. Clay samples are prepared with a maximum deviation of (13.7 ± 0.1) kN/m^3 and (16.7 ± 0.2) kN/m^3. The higher deviations in the low-porosity packing are due to some swelling behaviour after decompression.

The fabrication process at microstructural level can be described as follows. Prior to compaction, the initially hygroscopic powder hydrated at a moulding water content of 15% (dry of optimum) are grouped forming aggregates or peds, whose size, deformability and strength are influenced by the initial suction and temperature (estimated in $\psi \approx 2.3$ MPa at 22°C and $\psi \approx 2.0$ MPa at 80°C). These aggregates of about 7 µm $\times$ 5 µm can be identified in the low-density packing of the microphotographs of Fig. 2.32. During static compaction at dry of optimum, the relatively rigid peds due to soil suction effect resist the compaction pressure without excessive distortion, resulting in a decrease in inter-aggregate pore space due to aggregate slip and a subsequent increase in the dry unit weight and the degree of saturation without an appreciable change in soil suction (refer to Fig. 2.11). Temperature acts as a lubricating agent reducing the shearing strength of aggregate contacts. Water at the fabrication humidity is mainly adsorbed and contained in the diffuse layers, i.e. intra-aggregate water, with small quantities at inter-aggregate scale. As the moulding water content increases, the peds with lower suction values decrease in strength and are prone to suffer more deformation during compaction. Simultaneously the inter-aggregate water begins to fill the macroporosity. With values of water content above optimum, the aggregates are easily distorted and fuse together filling the inter-aggregate voids and presenting a more uniform and dispersed matrix type microfabric, where the peds are indistinguishable (McGown and Collins, 1975; Barden and Sides, 1970).

2.4 Resonant Column Tests

In order to investigate shear rigidity and aggregate-structure interaction and effects for the different soil packings used in the research, resonant column tests have been run to determine low-strain shear modulus at different net confining stress. A similar test procedure to that described in ASTM D4015 has been followed. Specimens of 38 mm diameter and 76 mm height were statically compacted in three layers using a three-piece split mould at a moulding water content of $w = 15\%$ ($\psi \approx 2.3$ MPa) and at the specified dry unit weights of 13.7 kN/m^3 and 16.7 kN/m^3. Membrane enclosed samples were isotropically loaded by air confining media at two different net mean stresses, first at a value of (σ_m-u_a) = 0.20 MPa and then, after running the first resonant column test, at 0.60 MPa for another cyclic torsional loading. These test methods are considered non-destructive when the strain amplitudes are less than 10^{-4} (ASTM D4015) which was the case for the tests (refer to Fig. 2.17), thus being feasible to do several measurements on the same specimen under increasing confining stress. Particular care was taken when attaching the roughened end platens to the specimen in order to ensure complete coupling for torsion, which is assumed if the mobilised coefficient of friction between the aforementioned parts is less than 0.2 for all shear strain amplitudes (ASTM D4015).

The Stokoe resonant column equipment is a fixed-free type under torsional mode of vibration in which the soil specimen is fixed at the bottom platen and free to oscillate at the top (Anderson and Stokoe, 1978). The top end is attached by friction to a rough platen connected to a coil-magnet drive mechanism, which is used to vibrate the specimen at first mode resonance in torsional motion. An accelerometer fixed to the drive plate is used to monitor this motion and a LVDT transducer detects vertical displacements of the specimen during testing. A signal generator supplies a sinusoidal voltage to the coils in the coil-magnet drive mechanism. The magnetic field induced by the current interacts with the one of the permanent magnets, which results in a torsional oscillation of the combined system (specimen top and drive mechanism) with the same frequency. By increasing the frequency of the input signal, the amplitude of the vibration varies until it reaches the first mode of torsional resonance (i.e., at its lowest resonance frequency). This first mode is defined as the lowest frequency at which maximum torsional motion of the top of the specimen in phase with excitation moment is obtained during a sweep of frequencies starting at 15 Hz (Al-Hunaidi *et al.*, 1996). The accelerometer generates a voltage from which the amplitude of vibration at the top of the specimen is computed. A x-y-time oscilloscope or alternatively a digital voltmeter is used to monitor the amplitude and frequency of the amplified accelerometer signal. The phase relationship describing resonance can be established by observing an ellipse on the x-y oscilloscope with the y-axis proportional to the driving voltage and the x-axis proportional to the accelerometer output. A schematic diagram of the test apparatus as well as the experimental setup of the system is presented in Suriol (1993).

The low-strain shear modulus of soil G is determined from the resonant frequency (or natural frequency of the first mode of vibration) f_n, the length of the soil specimen L, the density of the soil sample ρ, and the values of mass polar moments of inertia of specimen I and of drive system I_o, this last value estimated in $I_o = 2.6 \times 10^{-3}$ kg m^2 according to ASTM D4015. The shear wave velocity v_s is calculated on the basis of the theory of elasticity as (Das, 1983a):

$$v_s = \sqrt{G/\rho} = \frac{2\pi L f_n}{\alpha} \; ; \quad G = \frac{4\pi^2 L^2 \rho f_n^2}{\alpha^2} \tag{2.6}$$

where the dimensionless frequency factor α is a function of mass polar moment of inertia of both soil specimen and resonant column drive system and is found from (Das, 1983a):

$$\frac{I}{I_o} = \alpha \tan\alpha \; ; \quad I = \frac{\gamma \pi L D^4}{32g} \tag{2.7}$$

where γ is the unit weight, D the sample diameter and g the acceleration of gravity.

The shear strain γ in each cross section varies from zero along the vertical axis to a maximum at the perimeter of the specimen. The average shear strain $\bar{\gamma}$ occurs at a radius of 2R/3, being R the sample radius. The shear strain amplitude at radius r is calculated from (Suriol, 1993; Al-Hunaidi *et al.*, 1996; ASTM D4015):

$$\gamma = \frac{r\,\delta}{L}; \quad \bar{\gamma} = \frac{2R\delta}{3L} = k_\gamma \frac{DV_a}{3Lf_n^2} \tag{2.8}$$

where δ is the angle of twist estimated using measurements of the resonant frequency f_n and the acceleration levels of drive plate V_a (peak to peak amplitude accelerometer output). Factor k_γ, which is obtained by calibration, takes into account geometric aspects and for the test equipment used in this study has a value of $k_\gamma = 9.78 \times 10^{-4} \, mV^{-1}$.

Variations of shear modulus with shear strain amplitude at various confining net mean stresses are presented in Fig. 2.17 for the different overconsolidated soil packings. Interpolated values of undrained shear modulus for reconstituted normally consolidated Boom clay at different mean stress and strain levels obtained by Coop *et al*. (1995) and Coop *et al*. (1997) with bender elements and local axial gauges are also indicated for reference. Low-strain shear moduli ($\bar{\gamma} < 0.001\%$) for the high-density packing are higher than the corresponding ones of the low-density fabric, as expected for the void ratio influence on this modulus (Hardin and Black, 1968). However, the variation of shear modulus with confining stress for the low-porosity fabric is only marginal due to the overconsolidated state of the sample, which does not allow a further rearrangement of the macrostructure when the high pressure is applied. It is observed that the shear modulus of the high-density packing remains nearly constant up to a shearing strain of 0.001% and then decreases for higher strain levels. This decrease is more obvious at higher confining stress, situation that only can be explained in terms of testing errors associated with the experimental technique. In the case of the high-porosity packing, the shear modulus remains constant up to a higher value of shearing strain (0.004%). Degree of saturation effects on shear modulus are not important because water is mainly contained at intra-aggregate scale, as discussed in section 5.1.1, and capillary effects between aggregates are not of consideration. At higher water content values, capillary effects influencing intergranular stress begin to develop increasing shear modulus up to a maximum value. After this peak and as nearly saturated condition is approached the shear modulus is expected to decrease up to a value similar to that observed under intra-aggregate water condition. Wu *et al*. (1984, 1985) investigated capillary effects on shear modulus of silts and concluded that these effects have the greatest influence on soils having the smallest effective grain diameter. According to their results, low-strain shear modulus increased with degree of saturation up to a maximum around Sr $\approx$ 10% to 20% and then decreased with further increase in moisture, reaching under nearly saturated conditions the same value as in dry conditions. Similar results have been reported by Au and Chae (1980) testing treated expansive soils. Picornell and Nazarian (1998) observed increasing low-strain shear moduli with increasing soil suction in clayey and silty specimens caused by the effect of the receding menisci.

2.5   Mercury Intrusion Porosimetry and SEM Studies for the Different Soil Packings

2.5.1   Background of mercury intrusion porosimetry

2.5.1.1   Introduction

The pore size distribution (PSD) obtained by mercury intrusion porosimetry (MIP) is an essential fabric element, which is related with some soil behaviour characteristics: water, air and heat conductivity properties; adsorption and desorption isotherms (capillary phenomena); and volumetric deformation (rearrangement of fabric units). MIP data is used in this research to provide information about factors influencing fabric changes (effect of mechanical stress due to sample compaction) and

fabric-properties relationships (soil water retention curve related to porosimetry). Predictive equations for the saturated permeability based on the pore size distribution are presented in Garcia-Bengochea *et al.* (1979) (capillary and hydraulic-radius models) and Juang and Holtz (1986a, 1986b) (probabilistic model). Delage and Lefebvre (1984) used the porosimetry technique to investigate fabric changes of a sensitive natural clay during consolidation and to define an entrapped and free porosity on clay structure, Griffiths and Joshi (1989) studied changes in PSDs due to consolidation of different clay types, and Al-Mukhtar (1995) analysed pore space results on a kaolinite clay relative to the effects of mechanical and hydraulic (partially saturated) states. Prapaharan *et al.* (1985) predicted the soil moisture characteristic curve up to a matric suction value of 0.7 MPa based on porosimetry data. Measurements of this distribution are obtained in the upper range of pore size through techniques involving forced intrusion of a non-wetting fluid such as mercury (between apparent pore entrance diameters of about 2.5 nm to 100 μm), or by removal of pore water by suction or air overpressure, and in the lower range by BET tests (Wall *et al.*, 1981), where the nitrogen adsorption is used to investigate pore sizes as low as 10 Å. Another PSD method that has been recently used is the conductometric phase-transition porosimetry (Gunnink, 1991), where the changes in electrical conductance and temperature of saturated porous materials that have been subjected to a cycle of capillary freezing and melting are measured. This method has been satisfactorily contrasted with MIP data in saturated soils (Gunnink and El-Jayyousi, 1993). Indirect methods for PSD determination include the scanning electron microscopy (SEM) and the study of the representative grain size distribution by applying probability theory (Murota and Sato, 1969 in Juang and Holtz, 1986b).

This section presents results obtained from parallel studies of microscope observations and porosimetry to the different statically compacted fabrics used in the research. A quantitative description of the morphology of the porous medium by MIP tests, as well as by the application of matric suction/capillary methods which involve the interpretation of adsorption and desorption isotherms at constant total soil volume, has been carried out to examine the fabric and pore structure. A qualitative observation with a scanning electron microscope complements the overall description of the soil microstructure. Observations at these microstructural levels permit to gain insight into the understanding of higher structural levels and their interrelations from both hydraulic and mechanical viewpoints. One of the objectives is to interpret MIP results in order to define an entrance pore size region separating intra-aggregate and inter-aggregate zones, as well as to provide information about the entrapped and free porosity proportions. This pore size region will be further associated in section 5.1.1 with a transition zone in the retention curves separating regions of intra-aggregate porosity with quasi-immobile water that is little affected by loading processes and inter-aggregate porosity containing free water.

It is convenient to clarify that there are few PSD studies accomplished on artificially prepared unsaturated soils. However, recently, various authors have used a similar methodology to describe laboratory static or dynamically compacted unsaturated soils: Prapaharan *et al.* (1991), Delage *et al.* (1996) and Wan (1996).

2.5.1.2   *Background of Wahburn equation used in MIP*

In this section a formulation is followed to arrive to the Washburn equation (Washburn, 1921 in Meyer *et al.*, 1994) or in an equivalent form to the Laplace equation, which establishes the mechanical equilibrium across an interface of a non-wetting liquid (or a wetting liquid in the case of Laplace equation) and its vapour in a pore. Fig. 2.18 shows a closed system Σ (fixed material content) composed of two closed phases (a non-wetting phase α with higher pressure and a wetting phase β) and the portion of the interface S between them in internal equilibrium at the temperature T. If an infinitesimal reversible change at constant total volume (the system is enclosed by a fixed and thermally insulated bounding surface) is imposed to the interface by moving it to a new position S', then phase α will increase in an amount of volume dV^{α} and phase β will decrease by the same amount $dV^{\beta} = -dV^{\alpha}$. The changes in energy dU^{j} for every close phase j are (Guggenheim, 1967; Castellan, 1971):

$$\text{Phase } \alpha: dU^\alpha = T^\alpha dS^\alpha - p^\alpha dV^\alpha$$
$$\text{Phase } \beta: dU^\beta = T^\beta dS^\beta - p^\beta dV^\beta$$
$$\text{Interface } S: dU^S = T^S dS^S + \sigma^{\alpha\beta} dA^S$$
$$\text{System } \Sigma: dU^\Sigma = \sum_j dU^j = T(dS^\alpha + dS^\beta + dS^S) - (p^\alpha - p^\beta)dV^\alpha + \sigma^{\alpha\beta} dA^S \qquad (2.9)$$

where dS^j represents the entropy change, T^j and p^j are the phase temperature and pressure, $\sigma^{\alpha\beta}$ is the surface energy per unit area or interfacial tension (also called surface tension for a substance-own vapour interface) and dA^S represents the interface area change due to the addition of molecules coming from the wetting phase. The last expression represents the total change in energy of the closed system, where it is assumed internal equilibrium at temperature T. For the close thermally insulated system considering an infinitesimal reversible change: $dS^\Sigma = \sum_j dS^j = 0$ and $dU^\Sigma = 0$. This condition reduces Eq. (2.9) to:

$$p^\alpha - p^\beta = \frac{\sigma^{\alpha\beta} dA^S}{dV^\alpha}; \quad p^\alpha - p^\beta = \frac{2\sigma^{\alpha\beta}}{R}; \quad p^\alpha - p^\beta = \sigma^{\alpha\beta}\left(\frac{1}{R_1} + \frac{1}{R_2}\right) \qquad (2.10)$$

where the change in interface area, as well as the volume change of phase α, can be estimated assuming a conical bounding surface and an spherical interface: $dA^S = 4\pi(1-\cos\delta)RdR$; $dV^\alpha = 2\pi(1-\cos\delta)R^2 dR$ (refer to Fig. 2.18). The last expression applies if the surface is not spherical but has principal radii of curvature R_1 and R_2.

Fig. 2.18 shows the relation between the radius of curvature R, the radius of a capillary pore r and the wetting fluid contact angle θ_w (or alternatively, the non-wetting fluid contact angle θ_{nw}), which is the angle within the wetting liquid (or alternatively within the non-wetting fluid) between the wall of the tube and the tangent to the liquid surface. In terms of the pore radius, Eq. (2.10) becomes:

$$p^\alpha - p^\beta = \frac{2\sigma^{\alpha\beta}\cos\theta_w}{r}; \quad \cos\theta_w = \frac{\sigma^{s\alpha} - \sigma^{s\beta}}{\sigma^{\alpha\beta}} = -\cos\theta_{nw} \qquad (2.11)$$

The term $\cos\theta_w$ is called the wetting coefficient and is defined through the equilibrium requirements of Young's equation (Bear, 1972; Hassanizadeh and Gray, 1993; Grant and Salehzadeh, 1996), in which $\sigma^{s\alpha}$ is the interfacial tension of the solid - non-wetting fluid interface and $\sigma^{s\beta}$ the interfacial tension of the solid-wetting fluid interface.

In the case of MIP technique an absolute pressure p is applied to the non-wetting fluid (mercury) in order to enter the empty pores. For pores of cylindrical shape and parallel infinite plates (fissure-like structure), Eq. (2.11) applies in the form of Washburn equation (Juang and Holtz, 1986a; Griffiths and Joshi, 1989):

$$p = -\frac{4\sigma_{Hg}\cos\theta_{nw}}{d} \qquad (2.12)$$

in which σ_{Hg} is the surface tension of mercury, θ_{nw} the contact angle between mercury and the pore wall, and d is the apparent pore diameter or d/2 the parallel plates distance or the distance between both walls of the fissure. The surface tension used in this study was assumed $\sigma_{Hg} = 0.484$ N/m at 25°C. Small deviations from this value are not significant for the pore size results, since this parameter enters the equation only as a linear term. The contact angle with the clay minerals, which must be more

accurately evaluated due to its influence as a cosine function, was taken as $\theta_{nw} = 140°$ (usually assumed between 139° to 147° for clayey minerals; Diamond, 1970). Delage and Lefebvre (1984) chose $\theta_{nw} = 141°$ for a natural clay, while Griffiths and Joshi (1989) used $\theta_{nw} = 147°$ for illite and kaolinite clays.

For capillary rise or matric potential computation, the wetting liquid phase is free water, i.e. the one that has the lower pressure, and the non-wetting gas phase is humid air. The corresponding contact angle is usually taken as $\theta_w = 0°$. Laplace or Wasburn equation can be obtained involving a reference contact angle θ ($0° < \theta < 180°$) measured through the denser fluid (free water in capillary rise and mercury in MIP). When $\theta < 90°$ the denser fluid is said to wet the solid (water in capillary rise) and when $\theta > 90°$ the denser fluid is the non-wetting one (mercury in MIP). MIP technique as well as capillary pressure are subject to hysteresis as the wetting coefficient $\cos\theta_w$ at equilibrium is a function of the direction of displacement (Bear, 1972; Iwata *et al*., 1995); thus the contact angle may have a different value when the fluid-fluid interface is advancing or receding on a solid surface (rain drop effect). Another mechanism causing hysteresis is the geometry of the void space with bottlenecks (ink-bottle effect). This last effect is of special interest in intrusion-extrusion paths in MIP technique, as further discussed.

The high pressures applied to the samples may result in temporary or permanent alteration in the pore geometry. However, Lawrence (1978) observing similar first and second intrusion curves (after being removed all the mercury of the first intrusion by heating under vacuum), concluded that this technique did not cause any permanent damage to the soil. This last statement could be accepted due to the incompressibility of mercury and to the fact that, although the semi-hydrostatic pressures are large, the unbalanced forces acting to cause damage are only moderate, as the pore size is very small (Reed *et al*., 1980; Griffiths and Joshi, 1989). However, Gunnink and El-Jayyousi (1993) suggest the possibility of certain disturbance of pore structure at high pressures, in addition to the low representativeness of MIP sample compared to phase-transition porosimetry sample.

The assumptions and sources of error of MIP are examined in detail by Diamond (1970); among those limitations are: isolated pores enclosed by surrounding solids are not measured; pores that are accessible only through smaller ones ('ink-bottle' or constricted pores) will not be detected either until the smaller pores are penetrated; and the apparatus may not have the capacity to enter the smallest pores of the sample.

2.5.2   MIP equipment and testing procedures. MIP specimen preparation

MIP tests were carried out on a 'Quantachrome-Autoscan 33' porosimeter in conjunction with a 'Quantachrome Autoscan' filling apparatus, following ASTM D4404 testing procedure to examine the fabric and pore structure of the different soil packings. This equipment has two operating units: the macroporosity filling apparatus from approximately 11 kPa to 155 kPa (absolute pressure in a vacuum chamber) measuring apparent pore diameters from 9.5 µm to 135 µm, where the air sample is initially evacuated by applying a vacuum and surrounded subsequently by mercury; and the high pressure microporosity unit, where the mercury pressure is raised continuously between 0.17 MPa to 227 MPa (apparent pore diameters from 6.6 nm to 8.8 µm).

MIP equipment requires dehydrated cubical samples measuring preferably less than 3×10^3 mm^3 (limited by the sample holder and the cell stem volume). Soil samples were previously prepared and compacted at the desired dry unit weight (13.7 and 16.7 kN/m^3) and at constant water content of (15.0±0.3)%. From each compacted sample, PSD specimens were carefully trimmed into cubes measuring around 10 mm on each side. Subsequently these samples were freeze dried to remove the pore water and then kept in a desiccator until testing. Freeze drying process involves temperature and pressure conditions to eliminate the surface tension forces caused by air-water interfaces, and thus it is assumed that no shrinkage occurs on drying which could alter soil structure. The details of the procedure used in freeze-

drying can be summarised as follows (Ahmed *et al.*, 1974; Delage *et al.*, 1982; Mitchell, 1993; Delage *et al.*, 1996; Cui *et al.*, 1998a). The method consists of quickly freezing the soil specimen to cryogenic temperatures at values less than -130°C to avoid formation of crystalline ice, usually with direct immersion in liquid nitrogen (boiling point: -196°C), followed by true vacuum drying the frozen sample to remove the water by sublimation at a temperature between -60°C and -80°C. The frozen samples were dried in a period of more than 24 hours. The freezing process has shown to produce good results if the cooling operation is conducted quickly, due to the formation of a large number of small crystals, and thus minimising the 9% volume increase of water with its potentially structure-damaging growth, which occurs in natural freezing conditions due to ice crystallisation. Care must be taken in plunging soil samples in liquid nitrogen without any boiling around the immersed soil to improve the rate of freezing of water (Delage *et al.*, 1982; Cui *et al.*, 1998a). Delage *et al.* (1996) improved the technique immersing small pieces of soil in a container of freon 22 cooled close to its melting point (-145°C) by liquid nitrogen, ensuring that freezing takes place in the liquid phase.

The freeze-dried samples were placed in the sample holder and weighed. The dry sample weights for the high-porosity and low-porosity specimens were 4.90 g and 3.80 g, respectively. Prior to the operation of the low pressure unit, samples were outgassed in vacuum (around 5×10^{-2} torr or 10 Pa) for several minutes. Mercury is then allowed to flow into the sample holder. The bulk sample volumes determined in the filling unit for the high-porosity and low-porosity specimens were 3.92 cm^3 (dry density of 1.25 g/cm^3) and 2.40 cm^3 (dry density of 1.58 g/cm^3), respectively. Once filled the macroporosity unit with mercury, the intrusion pressure is raised up to approximately 155 kPa by means of compressed air. The sample is then depressurised to ambient and transferred to the microporosity unit for the high pressure run. For each test the pressure was applied continuously and the intrusion and extrusion data (both pressure and volume) of the two operating units were automatically recorded. To reach intrusion equilibrium in the microporosity unit, a slow pressure built-up rate (7 MPa/min) was selected (De las Cuevas, 1997). Apparent pore size were determined applying corrections for compressibility changes (compressibility of the various components of the system augment the measured intrusion values) and temperature effects (pressure-induced heating and consequent expansion of the system reduces the measured values) as suggested by ASTM D4404 with a blank test.

2.5.3   MIP results and interpretation

The corrected cumulative intrusion and extrusion volumes normalised by sample dry weight (affected by correction factors 1.25/1.4 and 1.58/1.7), both from the filling apparatus and the microporosity unit, are plotted against the apparent pore size in Fig. 2.19 for the different soil packings. A graphical cumulative pore volume distribution normalised by total volume, which is equivalent to the cumulative intruded/extruded porosity n, is also presented in Fig. 2.20. Due to the limited capacity of the microporosity unit to enter the smallest pores, there are some deviations from the theoretical porosity values calculated for the different compacted packings ($\Delta n \approx 0.020$ for the 13.7 kN/m^3 structure and $\Delta n \approx 0.029$ for the 16.7 kN/m^3 structure). This feature confirms the preservation of the soil structure during freeze-drying.

Fig. 2.21 represents the pore size distribution normalised by the total porosity n_o, which is defined as the porosity that can be intruded by the pressured mercury ($n_o = 0.462$ for the low-density packing and $n_o = 0.342$ for the high-density structure). In this case both packings converge to $n/n_o \rightarrow 1.0$ at high intrusion pressures, no matter that there is some small-unintruded pore space left. According to this definition, the n/n_o value is equivalent to Sr_{nw}, which represents the degree of saturation of the non-wetting mercury. From the previous graphs, the high-porosity sample appears to have a trimodal distribution, defining inflexion points at approximately 9 μm, 2 μm to 3 μm and less than 100 nm. The low-porosity specimen has a clear bimodal distribution defined by inflexion points at approximately 0.7 to 0.9 μm and other at a value less than 100 nm. Volumetric intrusions have been classified in macroporosity (pore sizes greater than 1 μm), mesoporosity (between 0.1 μm and 1 μm), microporosity (between 20 nm and 100 nm) and ultra-microporosity or infraporosity (less than 20

nm). According to Fig. 2.21, from pore sizes of 100 μm down to 10 μm (capillary type macropores) only the high-porosity packing presents $Sr_{nw} \approx 7\%$. From 10 μm down to 1 μm (microcapillary type macropores), the pore volume represents the 51% of the total porosity of the low-density packing, while it corresponds only to 23% of the total porosity of the high-density fabric. From 1 μm to 100 nm (mesopores), the pore volume represents the 19% of the total porosity of the low-density packing, and the 26% of the high-density packing. Pore sizes of less than 100 nm (micro and infrapores) correspond to a value of $(1\text{-}Sr_{nw}) \approx 23\%$ for the low-density packing and $(1\text{-}Sr_{nw}) \approx 51\%$ for the low-porosity packing. A more detailed porosity frequency is presented in the histogram of Fig. 2.22. This differential plot or relative frequency histogram takes the incremental increase in intrusion ΔSr_{nw} between the various points against the apparent pore diameter $\log x_m = \frac{1}{2}(\log x_{i-1} + \log x_i)$, which were selected at approximately equally spaced class width of $c = \Delta \log x \approx 0.35$ in order to avoid distortions in the appearance of the semi-log plot. The classification of the different porosity and their corresponding percentages are also indicated in this figure. Fig. 2.23 represents also an incremental plot of ΔSr_{nw} between the different intrusion points reported by the data logger of the equipment. This differential plot leads to a distorted image of the pore size histogram (the inter-aggregate pores are emphasised), because the selected diameter data points at which the change in intrusion is calculated generates a small class width, although approximately equally spaced on the logarithmic diameter axis at $c = \Delta \log x \approx 0.031$. Thus, it is recommended in order to compare results that pore diameters be selected at equally spaced intervals on the logarithmic diameter axis and that class widths be adequately chosen to avoid emphasised pore sizes. In spite of the aspects previously outlined, the high pore mode occurred consistently around 1μm to 2 μm for both fabrics and the fraction of inter-aggregate pores diminished with the compactive effort on the dry side of optimum.

Two types of porosity can be determined by two successive intrusions of mercury or alternatively with an intrusion/extrusion cycle, the latter one being the procedure followed in this research. The first intrusion fills all the accessible and interconnected pore space, thus giving the distribution of the total porosity, whereas on complete releasing of intrusion pressure will let only some mercury out from the non-constricted pores (Delage and Lefebvre, 1984). Some mercury remains trapped in the constricted pores of the soil: $Sr_{nw} \approx 72\%$ in the high-porosity packing and $Sr_{nw} \approx 46\%$ in the low-porosity fabric. A second intrusion will follow approximately the same extrusion path, thus defining the free porosity, which seems not to be significantly changed with the increasing compaction effort as observed in Fig. 2.19. Similar results have been reported by Griffiths and Joshi (1989) studying PSD changes due to consolidation of clays. The difference between the intrusion and extrusion cycle is the entrapped porosity, which accounts for the main reduction in total volume. This constricted porosity arises from the constrictions formed by clayey bridges and irregular shape of the aggregates, which act as 'ink-bottle' necks trapping the mercury in the inter-aggregate pores (local enlargements). Delage and Lefebvre (1984) proposed that the free or non-constricted porosity of the reintrusion volume corresponds to the intra-aggregate pore space, while the inter-aggregate pore space corresponds to the entrapped or constricted porosity. The intra-aggregate porosity detected when pressure is released represents 28% of the total porosity in the low-density packing and accounts for 54% of the total porosity in the high-density fabric, which correspond to an entrance pore size of approximately 150 to 200 nm in the intrusion curve (refer to Fig. 2.21). This last pore size can be accepted for the delimiting value between inter and intra-aggregate zones. This concept is further utilised in section 5.1.4 to define the 'intra-aggregate governing suction' zone of the retention curve, as suggested by Romero *et al.* (1998b) and Romero *et al.* (1999a). The intra-aggregate porosity compare well with relative permeability results presented in section 5.2.2, where quasi-immobile water contained at intra-aggregate scale represents 38% of the total volume of water in soil in the high-porosity packing, whereas it corresponds to 59% in the case of the low-porosity fabric (refer to Fig. 5.1).

Other useful information that can be obtained from PSD tests is the pore size density function f(x), which is a derivative of the pore size distribution represented in Fig. 2.21. Mathematically this last cumulative distribution F(x) expresses what fraction of the pore space has a pore diameter between x and ∞, and f(x).dx gives the fraction of the pore volume contributed by pores with diameters between

x and x+dx, i.e. f(x) is the density of pore volume corresponding to diameter x. Juang and Holtz (1986b) introduced a volumetric pore size density function f(x) defined as:

$$f(x) = \frac{1}{V_t}\left(-\frac{d(V_t - V)}{dx}\right) \;;\quad F(x) = \int_x^\infty f(x)dx = \frac{V_t - V}{V_t} \;;\quad F(0) = \int_0^\infty f(x)dx = 1 \tag{2.13}$$

where x is the apparent pore diameter, V_t is the total volume of pores that exists in the specimen and (V_t-V) is the volume of intruded mercury or the volume of pores with diameter equal to or greater than x. In the terminology previously used this last expression corresponds to:

$$f(x) = -\frac{dSr_{nw}}{dx} \;;\quad F(x) = \int_x^\infty f(x)dx = Sr_{nw} \tag{2.14}$$

Assuming constancy of the surface tension and contact angle, the following relations between the absolute pressure p being applied and the intruded pore diameter x, can be established:

$$p.x = 1.483 N/m \;;\quad dx = -\frac{x}{p}dp \;;\quad f(x) = \frac{p}{x}\frac{dSr_{nw}}{dp} \tag{2.15}$$

However Eqs. (2.13) to (2.15) are not useful for the interpretation of MIP raw data, since pore size x extends over several orders of magnitude and the class width dx reported by the intrusion record is not constant, emphasising the smaller pores. To overcome these distortions, the pore size density function at $\log x_m$ can be defined as follows:

$$f(\log x_m) = -\frac{dSr_{nw}}{d(\log x)} \quad\text{or}\quad f(\log x_m) = \frac{dSr_{nw}}{d(\log p)} = \frac{p}{\log e}\frac{dSr_{nw}}{dp} \tag{2.16}$$

where $\log x_m$ is the midpoint of each class. The class width $c = \Delta(\log x) \approx -\Delta(\log p)$ is approximately constant for the equipment, varying from 0.023 to 0.038. The pore size density function, evaluated calculating the ΔSr_{nw} change divided by the change of two adjacent entrance pore diameters reported by the equipment data logger and plotted at the midpoint between those diameters, is presented in Fig. 2.24.

The density function is found to be trimodal for the high-porosity fabric. A large pore mode occurred at 10µm (possibly related to macrofabric fissures as detected interpreting the porous surface dimension using a fractal scaling of the porosity), an inter-aggregate pore mode at 2 µm and a small pore mode around 10 nm. Changes in soil fabric caused by increasing compaction effort were at the expense of the larger pore modes. Total porosity decreases at increasing compactive effort on the dry side of optimum due to the fact that the large pore mode disappeared and the fraction of large inter-aggregate pores diminished, being the new position of this mode around 0.6 µm to 0.7 µm. Raw data values less than 40 nm of the high-density packing have been filtered by taking an average of the data within a specified width of one value above and one value below the data point.

MIP data can also be interpreted in terms of the fractal character of the different analysed porous media, admitting self-similarity or dilation invariance of the hierarchical void structure. Based on a deterministic three-dimensional Menger sponge model for fractal scaling of porosity, the pore volume V_k after k intrusion steps can be expressed in terms of the porous surface fractal dimension D_s as follows (Korvin, 1992):

$$V_k = V_t(1 - r_k^{3-D_s}) \;;\quad \log\left(-\frac{dV}{dr}\right) \propto (2 - D_s)\log r \tag{2.17}$$

where r_k (or r) is the intruded pore radius after k steps and V_t is the total pore volume for $k \to \infty$. According to Korvin (1992) similar relations can be derived from other porous media and packing models.

By means of Eq. (2.15), this last expression transforms to:

$$-\frac{dV}{dr} = \frac{p}{r}\frac{dV}{dp} \quad ; \quad \frac{dV}{dp} \propto r^{4-D_s}$$

$$\log\left(\frac{dV}{dp}\right) \propto (D_s - 4)\log p \quad \text{or} \quad \log\left(\frac{dSr_{nw}}{dp}\right) \propto (D_s - 4)\log p \tag{2.18}$$

According to this last expression, the fractal dimension D_s of the porous medium can be experimentally obtained from the first derivative of the log-log plot of the pore volume (or non-wetting degree of saturation) with respect to the mercury intrusion pressure dV/dp (or dSr_{nw}/dp) versus the intrusion pressure p. Equivalent expressions in terms of intruded pore volume have also been proposed by Meyer *et al.* (1994). Fractal concepts related to porosimetry studies have been recently applied to rock salt porous media by De las Cuevas (1997). However, to the author's knowledge, there are no published results of fractal concepts applied to pore structure characterisation of artificially prepared clayey soils.

Fig. 2.25 shows the experimental determination of the fractal dimensions of the different porous networks corresponding to both analysed packings. The intervals of self-similarity or scale invariance, which is a basic property of fractal objects, are given by the linear sections of the log-log plots. Two pressure zones are identified in the low-porosity packing: the low-pressure regime (p < 1 MPa) with an unphysical dimension of $D_s = 3.87$, which suggests that pores have a non-fractal pore structure, and the high-pressure regime (p > 1 MPa) with a characteristic fractal dimension of $D_s = 3.09$, which reflects a volumetric structure for pore sizes less than 1.5 µm. Several pressure regimes can be identified in the high-porosity packing: a low-pressure regime (p < 1 MPa) with similar unphysical dimension ($D_s = 3.85$), an intermediate regime (1 MPa < p < 5 MPa) for pore sizes between 300 nm and 1.5 µm exhibiting a fractal dimension of $D_s = 1.88$, which corresponds to a fissure like structure, and a high-pressure regime (p > 5 MPa) for pore sizes less than 300 nm presenting a volumetric structure ($D_s = 3.04$). The two linear regions with different slopes, corresponding to intermediate and high pressure regimes, indicate structural changes in the transition from one interval to the next, which can be associated with the different pore geometries between micro and macroporosity occurring at approximately pore sizes of 300 nm. The sheet-like pores can possibly be related to macrofabric fissures of the high-porosity packing. With increasing roughness, the fractal surface becomes more space-filling tending to higher fractal dimensions (volumetric structure). A summary of values found in the literature of fractal dimension of clay pore surface are reported in Giménez *et al.* (1997). Typical values in the pore range of 1×10^{-2} µm and 10 µm are between 2.49 and 2.90 (Bartoli *et al.*, 1992 in Giménez *et al.*, 1997). Lower values of pore surface fractal dimension between 1.15 and 1.24 were reported by Anderson *et al.* (1996) (referred in Giménez *et al.*, 1997) for pore range between 50µm and 250µm.

2.5.4   MIP - retention curve relationships

MIP can be used in order to determine the matric suction - saturation or water content relationships at constant packings. The mercury intrusion procedure can become assimilated to the desorption path of the soil moisture characteristic curve by applying to an initially saturated sample an increasing external air pressure (non-wetting fluid) to gradually dry the soil. Thus the injection of non-wetting mercury with contact angle of $\theta_{nw} = 140°$ is equivalent to the ejection of water from the pores (desorption curve) by the non-wetting front advance of air with $\theta_{nw} = 180°$ (refer to Fig. 2.18) for the same diameter of pores being intruded. Therefore, the volume of pores not intruded by mercury, i.e.

$Sr = 1-Sr_{nw}$, should be used to evaluate the water content or degree of saturation corresponding to the equivalent applied air overpressure. The relationship between the equilibrium mercury intrusion pressure p and air overpressure or matric suction (u_a-u_w) can be obtained applying Eq. (2.11) for the same diameter d of pores being intruded:

$$(u_a - u_w) = \frac{4\sigma \cos\theta_w}{d} \quad ; \quad p = -\frac{4\sigma_{Hg} \cos\theta_{nw}}{d}$$

$$(u_a - u_w) = -\frac{\sigma \cos\theta_w}{\sigma_{Hg} \cos\theta_{nw}} p \approx 0.196p \tag{2.19}$$

where σ is the water surface tension determined by the expression presented in section 5.1.6 and $\cos\theta_w = 1$ the wetting coefficient for the air-water interface.

The corresponding water content w can be estimated by means of the following expressions:

$$Sr_{nw} + Sr = 1 \quad ; \quad Sr \cdot e = Gs \cdot w \quad ; \quad w = \frac{e}{Gs}(1 - Sr_{nw}) = w_{sat}(1 - Sr_{nw}) \tag{2.20}$$

where Sr is the water degree of saturation and w_{sat} the water content at $Sr = 1$. However, this last expression does not consider the adsorbed water content due to surface adsorption, which can be estimated in approximately 2.2% for 5.5 Å Stern layer according to section 5.1.1. Neither considers the equivalent residual water content corresponding to the non-intruded porosity (Δn in Fig. 2.20). This water content can be approximated to $100\Delta e/Gs = 2.71\%$ in the case of the high-porosity packing and to 2.64% to the low-porosity fabric. This residual water content corresponds to approximately $w_r = 4.90\%$, which is similar to that presented in Fig. 2.26 of 6.0% for a suction value of 45 MPa related to the maximum intrusion pressure of 227 MPa. In order to take into account this residual water content w_r, Eq. (2.20) can be transformed into:

$$w = (1 - Sr_{nw})(w_{sat} - w_r) + w_r \quad ; \quad Sr = (1 - Sr_{nw}) + \frac{w_r}{w_{sat}}Sr_{nw} \tag{2.21}$$

Fig. 2.26 presents adsorption and desorption isotherms for the different soil packings compared to MIP results. Total suction values of the retention curves presented in section 5.1 have been converted to matric suction in order to have comparable results at low suction levels. In general, a good agreement is observed with respect to the shape of the retention curves, thus being feasible to use the pore size distribution to determine the soil moisture characteristic curve. Similar results were reported by Prapaharan *et al*. (1985). However, MIP data follow more closely the wetting paths, when they should have come next to the drying path, which is the moisture curve being predicted. No conclusive explanations have been suggested for these differences, which could arise to the different effects that water and dissolved salts produce on clay fabric compared to a less active mercury intrusion. However, the rapid desaturation of the high-porosity packing could be related to the fissure like structure detected at around 10 μm (refer to Fig. 2.24), which has also been observed in Fig. 2.25 interpreting the porous surface dimension using a fractal scaling of the porosity. Matric suction – saturation relationships at constant packings compared to MIP results are presented in Romero *et al*. (1998b) and Romero *et al*. (1999a).

With respect to the retention curves obtained by vapour equilibrium and air overpressure techniques, presented in section 5.1, they can be used to obtain the density function as well as the pore size distribution of the different clay fabrics. Retention curves data have been fitted to a modified form of the van Genuchten (1978, 1980) expression, as suggested in section 5.1.4, to smooth the steep behaviour of the intercluster water content zone and to take into account a maximum total suction value of a = 274 MPa under null intercluster and free water content. A constant osmotic suction value

of 0.41 MPa has been subtracted from total suction values corresponding to vapour equilibrium technique data, to obtain a matric suction retention curve. The following expression for the degree of saturation Sr in terms of matric suction s is assumed:

$$Sr = \frac{w}{w_{sat}} = \left[1 - \frac{\ln\left(1 + \dfrac{s}{274MPa}\right)}{\ln\left(1 + \dfrac{a}{274MPa}\right)} \right] \left(\frac{1}{1 + (\alpha s)^n} \right)^m \tag{2.22}$$

where the different parameters take the following values for the desorption path using a non-linear curve-fitting algorithm: $\alpha = 3.002$ MPa^{-1} , $n = 1.409$ and $m = 0.216$ for the low-density fabric, and $\alpha = 1.525$ MPa^{-1} , $n = 1.400$ and $m = 0.183$ for the high-density packing.

The corresponding degree of saturation of the non-wetting mercury can be expressed as:

$$Sr_{nw} = \frac{1}{\left(1 - \dfrac{w_r}{w_{sat}}\right)}(1 - Sr) = f_c(1 - Sr) \tag{2.23}$$

where the correction factor f_c takes into account the effects of the non-intruded porosity and the residual adsorbed water content, as it was previously suggested. The function dSr_{nw}/dp can be evaluated from Eqs. (2.19), (2.22) and (2.23) as follows:

$$\frac{dSr_{nw}}{dp} = \frac{0.196f_c\left(\dfrac{1}{1 + (0.196\alpha p)^n}\right)^m}{274MPa\left(1 + \dfrac{0.196p}{274MPa}\right)\ln\left(1 + \dfrac{a}{274MPa}\right)} + \frac{0.196f_c\alpha nm(0.196\alpha p)^{n-1}Sr}{1 + (0.196\alpha p)^n} \tag{2.24}$$

Fig. 2.27 is generated from Eq. (2.24) applying water retention curve fitting data. Although this plot is not a density function it reflects some characteristics of this function, showing a higher peak value around 2 μm for the low-density packing and a depressed peak value around 1 μm for the high-density packing. In the same way, this plot allows to separate two clearly defined zones, for entrance pore sizes of approximately below 150 nm the two curves remain attached and for higher values corresponding to inter-aggregate porosity the two curves show different behaviours. The same trend has been observed for the adsorption isotherms. Thus this pore size of approximately 150 nm can be accepted for the apparent delimiting value between inter and intra-aggregate zones, as it was suggested in section 2.5.3.

Eq. (2.24) can also be used to evaluate the pore size density function at $logx_m$, according to Eq. (2.16). Fig. 2.28 shows the pore size density function evaluated from retention curve data, both adsorption and desorption isotherms. The last one is theoretically more related to MIP data according to the previous discussion, but in this case the adsorption isotherm apparently presents a closer agreement to the mercury intrusion data reported in Fig. 2.24. Both isotherms show a peak value between 300 nm and 2 μm for the high-porosity packing, and a slighter depressed peak around 150 nm for the low-porosity fabric, thus presenting the general trend observed in MIP raw data for the dry-side compression effect in the packing fabrication though only one pore mode is detected.

2.5.5   MIP-saturated permeability relationships

2.5.5.1   *General MIP-permeability model*

Several theories have been developed to try to correlate MIP results with the saturated permeability, such as capillary models, hydraulic radius model and probabilistic models (Garcia-Bengochea *et al.*, 1979; Juang and Holtz, 1986a, 1986b). Obviously, as permeability is a function of many parameters such as the size of the pores, the shape of the channels, the tortuosity, the clay mineralogy, the salinity of pore water and the direction of flow, predictive equations based only on volumetric aspects are unsuitable for estimating permeability (Lapierre *et al.*, 1990). However, predictive equations permit to demonstrate the dependence of permeability on pore size distribution and reflect the changes in soil fabric caused by different compaction energies, and in this sense, it has been incorporated in the present investigation.

The different models are based in the Hagen-Poiseuille equation for laminar flow through a cylindrical capillary of diameter x (Garcia-Bengochea *et al.*, 1979; Lapierre *et al.*, 1990). The main difference arises in the way of how two cross-sections (i and j separated by a distance L) with identical pore size density functions defining a flow region are considered to be connected. The probability $P(x_i , x_j)$ of pores of sizes between x_i and $x_i + dx_i$ on cross-section i to be connected to pores of sizes between x_j and $x_j + dx_j$ on cross-section j, presents the following extreme cases (Juang and Holtz, 1986b):

- For L >> x, the connection can be assumed to be completely random (each section is independent of the other), and hence the probability is $P(x_i , x_j) = f(x_i) f(x_j) dx_i dx_j$. The term f(x).dx represents the fraction of pore volume, which is assumed equal to the area ratio, contributed by pores between x and x+dx, where f(x) is the pore size density function defined in Eqs. (2.13) or (2.14).
- For L → 0 the pores considered are correlated, and hence the probability is $P(x_i , x_j) = f(x_i).dx_i$ or $f(x_j).dx_j$.

Considering that the connection between pores are partially correlated, Juang and Holtz (1986b) proposed a connecting function based on the assumption that pores of diameter x_i on cross-section i have a greater probability of being connected with pores of the same size on cross-section j than they have of being connected to pores of other diameters.

For simplicity, an expression equivalent to the classical capillary concept of correlated pores has been selected for the permeability model, though it is obvious that the porous media is extremely disordered and does not adjust to an ordered concept. However, the first case usually reports low permeability values (Vicol, 1990), that apparently are not representative of the porous media either. It is evident that a transition is more realistic, but its implementation is more difficult due to the appearance of some empirical parameters in the connecting function, which can also affect the indirect estimated values. For a distribution of capillaries, Garcia-Bengochea *et al.* (1979) obtained the following equation for calculating the permeability k_w:

$$k_w = \frac{\rho_w g x^2}{32\mu} \quad ; \quad k_w(x_m) = \frac{\rho_w g n}{32\mu} \sum_i^m x_i^2 \bar{f}(x_i) \tag{2.25}$$

where ρ_w is the water density at a certain temperature, g the gravitational acceleration, μ the coefficient of absolute viscosity of water at a specified temperature, n the porosity of the soil and $\bar{f}(x_i)$ the frequency histogram presented in Fig. 2.22. The second moment about the origin of the histogram represents the number of pores of size x_i multiplied by the pore area. The area frequency of the capillary diameter x_i is admitted to be equivalent to the volumetric frequency, which is the quantity measured in MIP method. The factor n converts the Sr_{nw} values to equivalent ones related to gross cross-sectional areas. The permeability function $\sum_i x_i^2 \bar{f}(x_i)$ reports the following values: 3.4×10^7 nm²

for the high-porosity packing and 6.7×10^6 nm^2 for the low-porosity fabric. The estimated saturated permeability is around 5.0×10^{-12} m/s for the high-porosity packing and around 7.6×10^{-13} m/s for the high-density fabric. These results are presented and compared with other reported data in Fig. 2.36, showing a quite good agreement. Relative permeability values $k_w(x_i) / k_w(x_m)$ for different pore sizes are presented in Fig. 2.29 (x_m represents the maximum pore diameter). It can be observed that the permeability is mainly related to the distribution of the larger pore sizes (i.e. > 1 μm). Pores of sizes less than this threshold diameter are considered negligible in the calculation of permeability. A conclusion that arises from the previous plot is that the permeability is very sensitive to the magnitude and frequency of the large pore mode, and that any factor that varies this part of the distribution, such as a compression, can be reflected in an appreciable change of the permeability. Relative water permeability values based on PSD predictive equations joined to MIP – retention curve relationships, which permit to reflect their dependency in terms of degree of saturation, are presented and compared to inflow / outflow experimental data in section 5.2.2.

In order to introduce the pore size density function as suggested in the second case for correlated pores, Eq. (2.25) transforms to:

$$k_w(x_m) = \frac{\rho_w g n}{32 \mu} \int_0^{x_m} x^2 f(x) dx \qquad (2.26)$$

As previously stated, the permeability prediction is sensitive to the larger pore diameters. Pores less than $x_m = 100$ μm were considered in order to obtain the relationship between the permeability and the MIP parameters. This upper limit of pore size x_m was determined by the low-pressure capacity of the mercury porosimeter. Fig. 2.30 presents the evaluation of the permeability function $x^2 f(x)$ based on raw MIP data. The numerical integration of $\int_0^{100\mu m} x^2 f(x) dx$ reports a value of 3.7×10^7 nm^2 for the high-porosity fabric and 1.3×10^7 nm^2 for the high-density packing. These values are related to a permeability of 5.5×10^{-12} m/s for the high-porosity packing and 1.4×10^{-12} m/s for the low-porosity fabric, which are presented in Fig. 2.36.

Retention curve data can also be used to estimate the relative and saturated water permeability. The permeability function can be evaluated from Eqs. (2.15), (2.23) and (2.24), resulting in the following expression: $x^2 f(x) = 1483 nm MPa \frac{dSr_{nw}}{dp}$. This way, the permeability function has an identical shape to that represented in Fig. 2.27, affected by a scaling factor. The integration of $\int_0^{100\mu m} (1483 nm MPa \frac{dSr_{nw}}{dp}) dx$ reports the following values for the desorption isotherms: 7.0×10^6 nm^2 for the high-porosity packing and 2.8×10^6 nm^2 for the high-density fabric, which correspond to a permeability of 1.0×10^{-12} m/s and 3.2×10^{-13} m/s, respectively. These results are indicated in Fig. 2.36, showing lower values if compared to other test results. However, the adsorption isotherms parameters reflect higher permeability values: 9.2×10^{-12} m/s for the high-porosity packing and 5.3×10^{-12} m/s for the high-density fabric.

As previously suggested, estimations from pore volumetric considerations alone cannot be simply related to the permeability of the soil, and are therefore unsuitable for its estimation. Nevertheless, these raw estimations demonstrate the dependence of permeability on MIP and retention curve data, as well as the consequences of porosity changes. The drastic permeability changes associated with different wetting and drying retention curves are not clearly understood and further investigation on this topic needs to be considered.

2.5.6   SEM technique for direct fabric viewing. Comparisons between porosimetry and microscopy

2.5.6.1   Experimental procedure

Soil packings with a dry unit weight of 13.7 and 16.7 kN/m^3 have been statically compacted at a moulding water content of 15% in order to study the fabric by a scanning electron microscope (SEM). The fabric of an artificially aggregated pellet surface compacted to an estimated dry unit weight of 20.6 kN/m^3 and at a hygroscopic humidity of 3% is also studied.

SEM equipment used in this research is a 'Stereoscan 360' from Cambridge Instruments. Since SEM requires a high vacuum sample chamber (1×10^{-5} torr = 1.33×10^{-3} Pa), the sample must be dry. As in the MIP technique, freeze-drying process was used for the different soil packings to minimise structure changes, which usually accompany water removal by air or oven drying. A similar process to that previously described for the MIP technique was followed. The main difficulty in the SEM study is the preparation of the sample surface, which must retain the undisturbed fabric of the compacted soil. Dry-peel-fracture surfaces of the dry side compacted specimens are considered to be representative of the undisturbed fabric. Surface preparation included gentle blowing and peeling following fracturing. In the case of the pellet surface there was no surface preparation, thus being influenced by the compaction process, showing a preferential orientated fabric not completely representative of the original structure.

SEM electron bombardment of the sample surface causes local charging, which interferes with the viewing procedure. Therefore it is necessary to coat SEM surfaces with a conducting film of colloidal silver and a thin layer of gold palladium (20 nm - 30 nm) in a vacuum evaporator (around 3 kPa), in order to prevent surface charging and loss of resolution (Mitchell, 1993).

Fig. 2.31 presents three photomicrographs of the different packings at a magnification of approximately ×5000. Aggregate of platelets, inter-aggregate and intra-aggregate pores, as well as assemblage connectors (clayey bridges), are presented in the digitised and processed photomicrograph indicated in Fig. 2.32 corresponding to the high-porosity fabric. The constricted porosity (local enlargements represented in black) arises from these clayey bridges and irregularity of the aggregates, which act as 'ink-bottle' necks entrapping the interconnected porosity, as suggested by Delage and Lefebvre (1984).

2.5.6.2   Interpretation of SEM results

The bimodal pore size distribution obtained in MIP tests on the high-porosity samples (the high pore mode that is not considered is assumed to be related to macrofabric fissures) is in agreement with the aggregated structure seen under SEM technique. The aggregates are composed of platelets of approximately 0.5 μm to 1 μm with small intra-aggregate porosity, separated by a porous irregular network at inter-aggregate level. This is more evident in the high-porosity packing. The pellet low-porosity fabric does not present any appreciable inter-aggregate network and the aggregates appear to fuse together, mainly due to the high compaction stress given during fabrication and possibly due to the absence of a surface treatment that could keep out of sight the real structure of the clay. This last concept is based on the proportion of platelets appearing on the plane of the photo, showing more faces than in the other photomicrographs and bringing up the alteration of the pellet surface. The size of the aggregates is around 7 μm × 5 μm, separated by an average inter-aggregate distance of about 1 μm to 2 μm for the high-porosity packing, which is in correspondence with MIP results. Interconnecting clay bridges of the order of 1 μm, crossing and interfering inter-aggregate pores, can also be distinguished in the digitised image of Fig. 2.32. The 16.7 kN/m^3 packing shows some stuck and fused aggregates due to the collapse of inter-aggregate pores during increasing compression. The pores within the aggregates, which are more difficult to distinguish, are theoretically defined by the population measured in MIP tests. The small intra-aggregates pores are probably also compressed in

the low-porosity pellet due to the elevated fabrication pressures and after all macropores have been collapsed.

SEM photomicrographs have been digitised and processed in order to visualise the evolution of the porous network and its change due to the different compaction pressures (60% black has been used to identify the porous network in the three digitised images). Fig. 2.32 shows the representation (pores are black and particles white) of these porosity changes at different stress levels. In the case of the pellet packing with a dry unit weight of 20.6 kN/m^3, the black pores represent 7491 pixels (10971 pixels if other transition colours are considered) with respect to the 132756 pixels of the image, corresponding to a 2-D porosity between 5.6% and 8.3% (the actual porosity is around 22%). The high-density packing of 16.7 kN/m^3 presents 27192 black pixels (37453 pixels if other transition colours are considered) with respect to the 127008 pixels of the image, representing an 2-D porosity between 21.4% and 29.5% (the actual porosity is around 37%). The low-density packing presents 32836 black pixels (42218 pixels if other transition colours are considered) with respect to the 126720 pixels of the image, corresponding to a 2-D porosity between 25.9% and 33.3% (the actual porosity is around 48%). In general, certain agreement is observed between the porosity measured by image processing and calculated by indirect methods. The lower values in the former 2-D case are explained by the excessive amplification of the image representing an area of around 20 µm × 14 µm with respect to the soil REV.

2.6   Swelling-collapse potential of the aggregate packings under applied loads.

2.6.1   Testing procedures and results of swelling-collapse experiments

To investigate mechanical behaviour of aggregate packings a series of conventional oedometer tests have been run at different dry unit weights starting at a hygroscopic humidity of 3% (total suction of about 100 MPa). The test method, which follows ASTM D5333 and D4546, determines the magnitude of one-dimensional swelling or collapse behaviour that occurs when the unsaturated laterally constrained specimens are inundated with water under a given net vertical stress (σ_v-u_a).

The dead-weight loading apparatus with spherical seating loading cap, which complies with the requirements of test method ASTM D2435, is equipped with an oedometer ring 50 mm in diameter and 20 mm in height that fixes in the compaction mould presented in Fig. 3.4. Specimens have been statically compacted at different dry unit weights (12, 17 and 20 kN/m^3) directly in the consolidation ring, previously greased with Teflon grease, up to a final height of 10 mm. The prepared samples and the upper air-dried porous stones were placed in the loading device, and enclosed in a loose fitting plastic membrane to minimise changes in specimen water content due to evaporation during testing. Load increments at natural water content were applied at two hours interval until reaching the target soaking stresses: 10 kPa, 50 kPa, 200 kPa and 1.0 MPa. The specimens were inundated with demineralised water, allowing sample wetting from the bottom in order not to trap air. During the saturation phase the evolution of vertical strain with time has been followed for at least one day and a relatively rapid stabilisation can be observed after less than one hour for the collapse behaviour of the low-density structures. Swelling pattern of the high-density packings has been followed for a longer period of at least 72 hours in order to record some secondary long-term swell and determine the end of the short-term primary swell as suggested by ASTM D4546, and which is being completed after approximately six hours.

Fig. 2.33 shows the magnitude of vertical strain measured after saturation as a function of initial dry unit weight and net vertical stress. Collapsing and swelling regions are clearly defined and separated by a swelling pressure boundary. This plot is completed with data from other test series of Boom clay (Romero *et al.*, 1994). Swelling and collapse behaviour of pellet aggregates with a size varying between 2 mm and 2.2 mm that have been statically compacted at a global dry unit weight of 14 kN/m^3, as well as a mixture of 50% / 50% mass ratio of Boom clay powder and pellets at a global dry unit weight of 15 kN/m^3, have also been represented in this figure.

2.6.2 Experimental method and results of one-dimensional consolidation tests

2.6.2.1 Experimental method

One-dimensional consolidation tests under constant load, following ASTM D2435, were performed to provide complementary data on time-deformation and load-deformation properties of an initially densely packed specimen. The oedometer equipment is the same apparatus that was previously described. The specimen was statically compacted in the greased oedometer ring ($\varnothing$ 50 mm) installed in the compaction mould to a target $\gamma_d = 16.7$ kN/m^3 at a moulding water content of w = 15%, up to a final height of 10.14 mm (diameter to height ratio greater than four in order to minimise friction effects). After enclosing the sample and the upper air-dried porous stone with a loose fitting plastic membrane, the unsaturated laterally constrained specimen was inundated from the bottom with demineralised water under a net vertical stress of $(\sigma_v - u_a) \approx 1.2$ kPa, in accordance to the free swell method proposed in ASTM D4546. A vertical swelling strain of 21.31% has been measured after 120 hours of saturation phase evolution. The starting void ratio of the consolidation test is approximately $e_o = 0.959$, corresponding to a high-porosity packing of $\gamma_d = 13.5$ kN/m^3. The load increment ratio has been selected between $0.3 < \delta(\sigma_v - u_w)/(\sigma_v - u_w)_o \leq 1$, in order to have more data points defining the compression curve. However, the load increment ratio has a high influence on consolidation of clays, resulting in smaller compression for the smaller increment ratio (Das, 1983b). A constant duration of 24 hours for each load increment has been adopted.

Time evolution of soil deformation has been interpreted using a non-linear curve-fitting algorithm, in order to determine the different conventional parameters used in consolidation analysis following Terzaghi's theory. The dial displacement d under an effective stress increment $\delta(\sigma_v - u_w)$ can be theoretically expressed as:

$$d = d_o + \frac{2h}{E_k^{'}}\delta(\sigma_v - u_w)\overline{U}(t,C_v) + 2hC_\alpha \log(t/t_{90})$$ (2.27)

where d_o is the initial compression mainly due to the equipment deformability, 2h the mean thickness of the specimen, $E_k^{'}$ the drained constrained modulus of elasticity, $\overline{U}(t,C_v)$ the average degree of consolidation that is a function of time t and the coefficient of consolidation C_v (Lambe and Whitman, 1979; Das, 1983b), C_α the coefficient of secondary consolidation, and t_{90} the time required for 90% of average consolidation.

2.6.2.2 Experimental results and interpretation

Curve fitting plots compared to experimental data, as well as some back-analysed consolidation parameters with reference to Eq. (2.27), are presented in Fig. 2.34 for selected load steps. Time t_{90} was achieved in approximately 10 min for the first two load steps and around 30 min for the last load steps.

Values of the specific volume v for the loading and unloading sequence are plotted against the effective stress $(\sigma_v - u_w)$ in Fig. 2.35. Since K_0 is approximately constant during virgin compression (refer to section 2.3.1.2) the critical state parameter $\lambda(0)$ defined for isotropic stress states, can be determined with reasonable accuracy from one-dimensional test results: $\lambda_{oed}(0) = 0.096$. Initial compression values d_o have been taken into account for the adequate representation of the compression curve. For one-dimensional unloading K_0 is not constant and therefore there is no simple relationship between κ defined for isotropic stress states and $\kappa_{oed} = 0.037$ value (refer to Fig. 6.57 and Fig. 6.67 for further results). Horseman *et al.* (1987) reported a mean $\lambda(0) = 0.178$ and $\kappa = 0.046$ for intact Boom clay, obtained from one-dimensional consolidation results. Alonso *et al.* (1995) suggested

a value $\lambda(0) = 0.160$ and $\kappa = 0.031$ for an artificially aggregated 2-mm pellet fabric compacted at $\gamma_d = 14$ kN/m^3, obtained from one-dimensional consolidation tests.

The preconsolidation stress $(\sigma_v - u_w)_o^*$ is estimated between 120 kPa and 180 kPa, based on the interception between the virgin consolidation line and the unloading line plotted in the maximum curvature zone, the drastic change in the slope of the $-\delta\ln(\sigma_v - u_a)/\delta v$ and the cumulated strain energy $-\Sigma(\sigma_v - u_a)\delta v/v$ curves versus the vertical effective stress, and the breakpoint of the drained constrained modulus and the effective stress as proposed by Janbu *et al.* (1981) and Crawford (1986). Alonso *et al.* (1995) suggest a value of 160 kPa for an artificially aggregated 2-mm pellet fabric with a packing of $\gamma_d = 14$ kN/m^3. Further results of vertical preconsolidation stresses are presented in Fig. 6.58. In the normal consolidated zone, the coefficient of consolidation and the rate of secondary compression remain approximately constant. The low value of $C_\alpha \leq 0.006$ indicates a medium-low secondary compressibility (Mesri, 1973). The constrained modulus E_k' in the normal consolidation zone varied between 22 MPa and 41 MPa. Assuming isotropy and a drained Poisson's ratio of $\nu = 0.19$, according to previous results (though it could be possible to admit a higher value for a soil skeleton with lubricated contacts), the following expression can be used to obtain an approximate value of the drained Young's modulus E':

$$E' = \frac{E_k'(1 + \nu)(1 - 2\nu)}{(1 - \nu)} \approx 0.91E_k' \tag{2.28}$$

The drained modulus E' is estimated to be 20 MPa to 37 MPa in the normal consolidated range of the test. Horseman *et al.* (1987) give an estimated value of 122 MPa for the slightly overconsolidated state of Boom clay at an in situ effective stress of 2.5 MPa. An extrapolation of the experimental results in the normal consolidation range for the previous effective stress value reports $E_k' \approx 85\text{MPa}$, with a corresponding $E' \approx 80$ MPa.

Saturated water permeability k_{ws} is estimated from consolidation data, assuming Terzaghi's theory of the rate of consolidation as valid (Lambe and Whitman, 1979; Das, 1983b). Values for the compression sequence are plotted against the void ratio in Fig. 2.36. As a first approximation, the logarithm of water permeability decreases linearly with void ratio. Other indirect experimental results obtained from suction controlled tests (refer to section 5.2.2) and MIP technique (refer to section 2.5.5) are also presented. In general, a good agreement is obtained from the different indirect procedures used. Published results for saturated water permeability are plotted in Fig. 2.37.

SCK·CEN saturated permeability results of 50% / 50% mass ratio mixture of powder with high-density pellets ($\gamma_{dpe} \approx 20.6$ kN/m^3) compacted at different overall dry unit weights are also presented. In order to compare these directly measured results it is convenient to convert them to an equivalent macroporosity void ratio, which is more representative of the flow pattern of preferential paths. Such macropores are developed because of the clod structure that exists prior to compaction. The zones between pellets or clods filled with compacted powder offer less resistance to flow and thus act as preferred channels for flow. Upon wetting the artificially prepared pellet structure does not disappear according to observations carried out by the author using SEM photomicrographs, though certain softening of the clods occur due to suction reduction trying to fuse towards a matrix dominant structure. Jayawickrama and Lytton (1992) observed that the permeability to water phase decreased as the level of saturation in the clay increased due to a reduction in the macrochannel size as a consequence of clod swelling upon wetting. Benson and Daniel (1990) presented experimental results of the influence of clods on water permeability of compacted clays. The following proposed expression permits to obtain the initial macroporosity void ratio e_M for a weight ratio pellet-powder $\alpha = W_{pe} / W_{po}$ mixture compacted to a target overall dry unit weight of γ_d:

$$\gamma_{dpo} = \frac{\gamma_{dpe}}{\dfrac{\gamma_{dpe}}{\gamma_d}(1+\alpha) - \alpha} \quad ; \quad e_M = \frac{Gs\gamma_w}{\gamma_{dpo}} - 1 \qquad\qquad (2.29)$$

where γ_{dpe} and γ_{dpo} are the pellet and powder dry unit weights respectively. For an overall packing of γ_d = 16.7 kN/m^3 with a 50% / 50% mass ratio mixture ($\alpha = 1$) of powder with high-density pellets (γ_{dpe} ≈ 20.6 kN/m^3), the overall void ratio is 0.591, whereas the estimated macroporosity void ratio representative of the compacted powder is e_M ≈ 0.894. Probably the artificially prepared mixture of soil behaves between both extreme cases presented in Fig. 2.37, trying to follow the macrochannel trend during the initial condition, when the clod softening due to water diffusion into the aggregated structure has not been reached. At longer periods and elevated stress levels, the aggregated fabric tends to fuse together into a matrix dominant fabric of monomodal porosity. Taking an average e ≈ 0.620 as the in situ void ratio at Mol, Fig. 2.36 suggests a saturated permeability value of around 1.5×10^{-12} m/s to 5×10^{-12} m/s. Conventional oedometer and suction controlled test results are more representative of a vertical permeability value, mainly due to the preferential horizontal orientation of clayey particles during compaction, that follows a similar direction to that expected under natural deposition conditions. Fig. 2.37 suggests a mean value of 2×10^{-12} m/s to 4×10^{-12} m/s for the in situ vertical permeability (SCK·CEN results have been converted to the macroporosity void ratio). A slightly higher value between 3×10^{-12} m/s and 8×10^{-12} m/s has been considered for the in situ horizontal permeability.

Loading after free swelling under a seating pressure in accordance to ASTM D4546 (Method A) recovers the initial void ratio e_o = 0.607 of the specimen at an approximate vertical effective stress value of 0.80 MPa. Because some secondary swell has been accumulated after 120 hours of saturation phase evolution, the loading increments have been considered of 24 hours duration, which include some secondary consolidation. Fig. 2.35 does not include this additional deformation, because the secondary consolidation has not been considered, therefore not being this figure representative for the swelling pressure estimation. The swelling pressure of 0.80 MPa for the 16.7 kN/m^3 packing determined by the free swelling-loading procedure reports a higher value than the estimated 0.60 MPa based on Fig. 2.33 following ASTM D4546 (Method B), as expected from the stress-path dependency of the swelling pressure (Justo *et al*, 1984; Gens and Alonso, 1992). Further details of suction controlled swelling and shrinkage pressure tests are discussed in section 6.5.
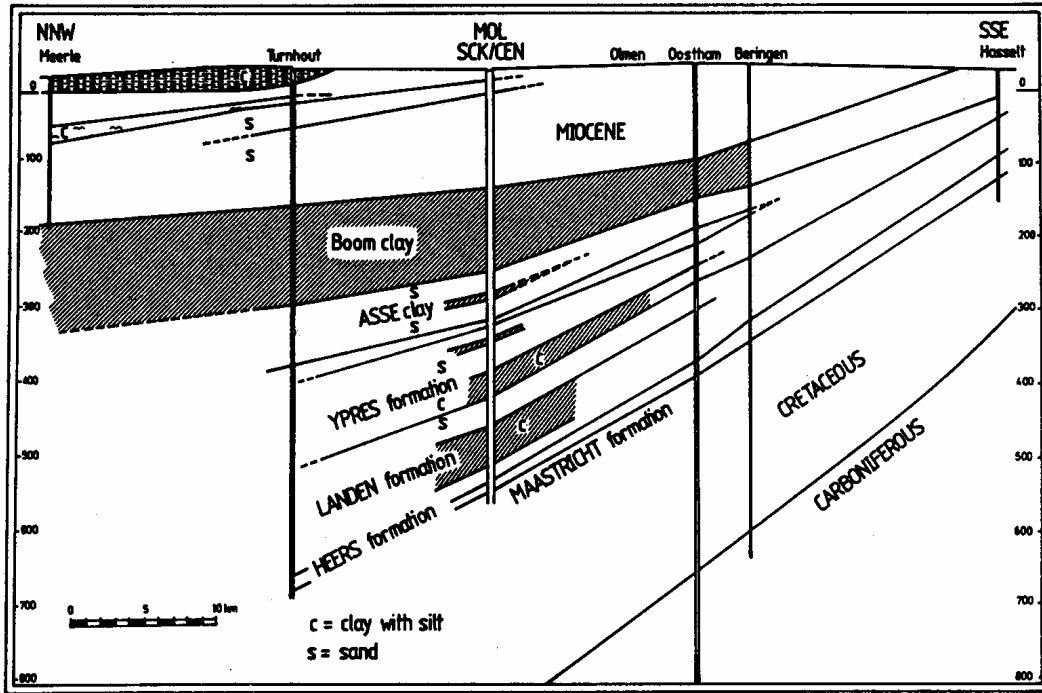
Figure 2.1   NNW-SSE geological cross-section through the Mol site (Horseman *et al.*, 1987).
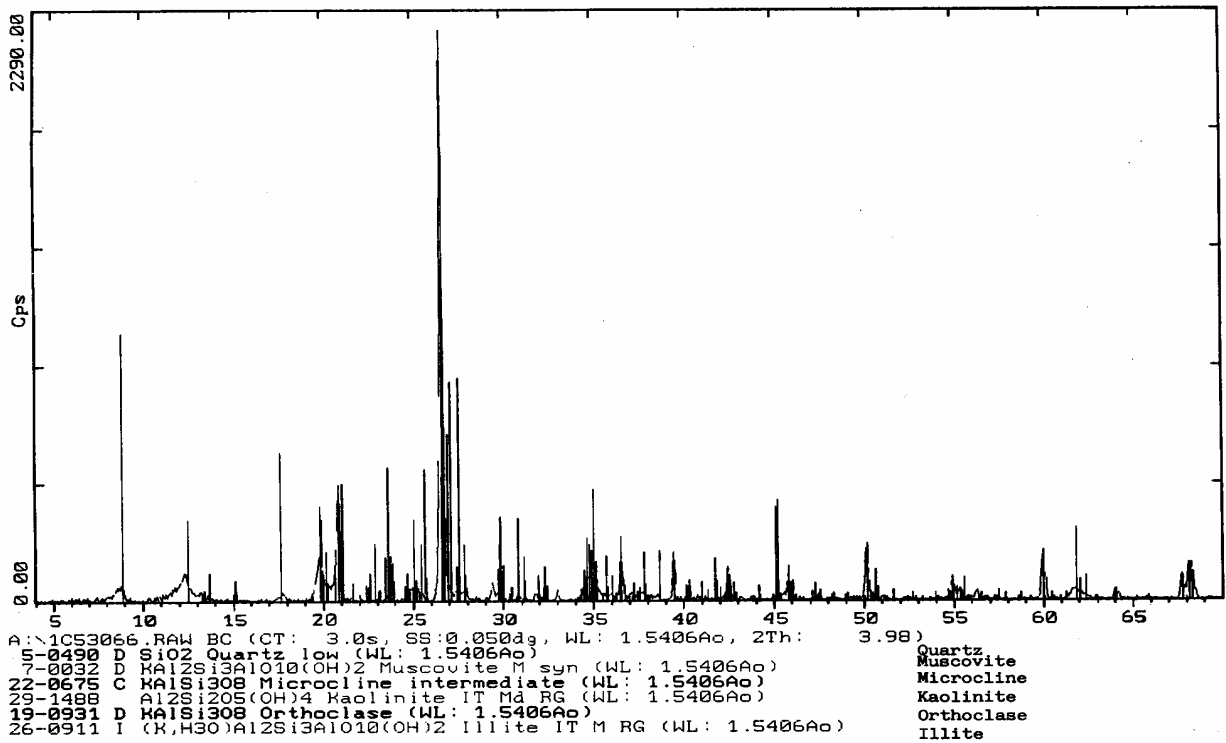
Figure 2.2   X-ray diffraction pattern and mineral identification for the most intense reflections.
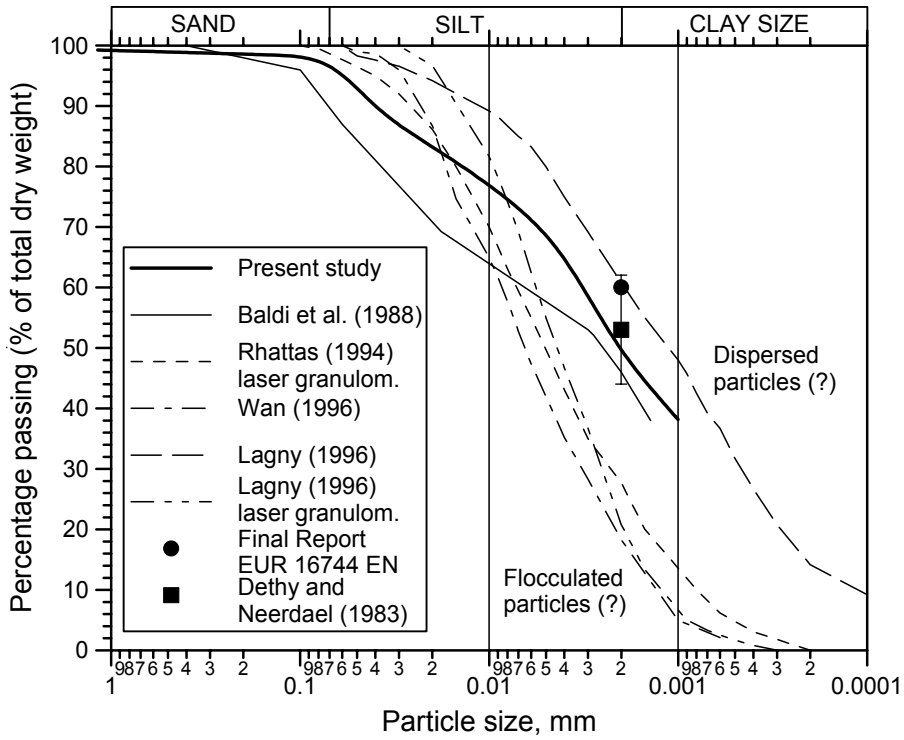
Figure 2.3   Particle size distribution.
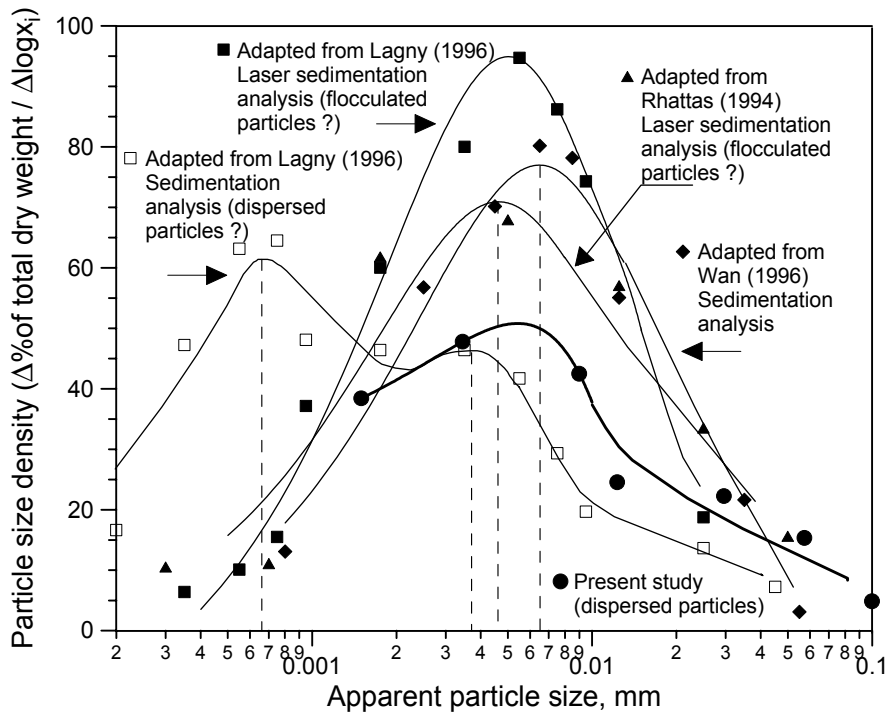
Figure 2.4   Particle size density function.
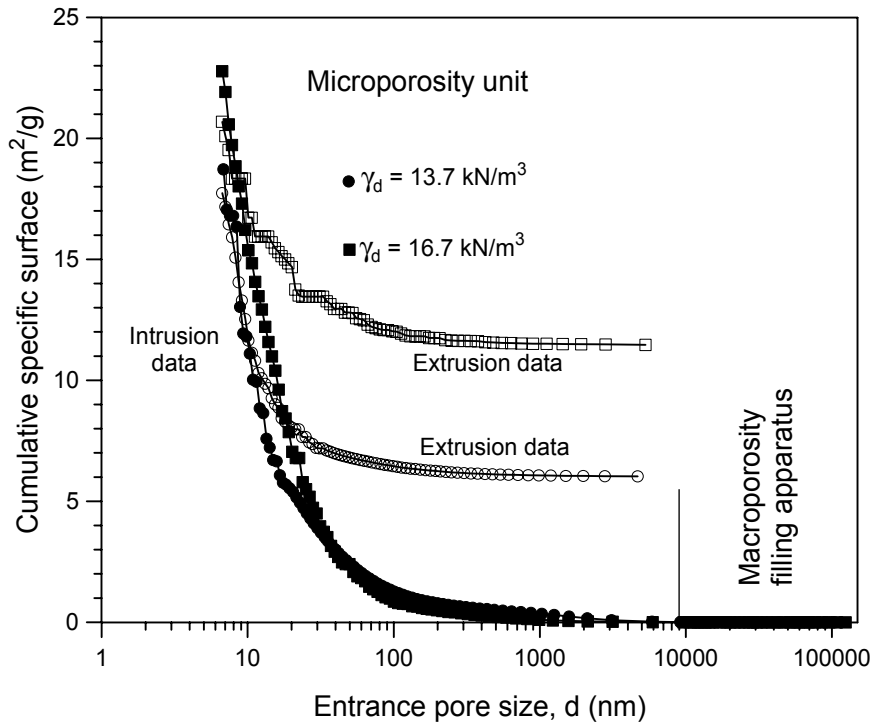
Figure 2.5   Specific surface for different packings using MIP technique.
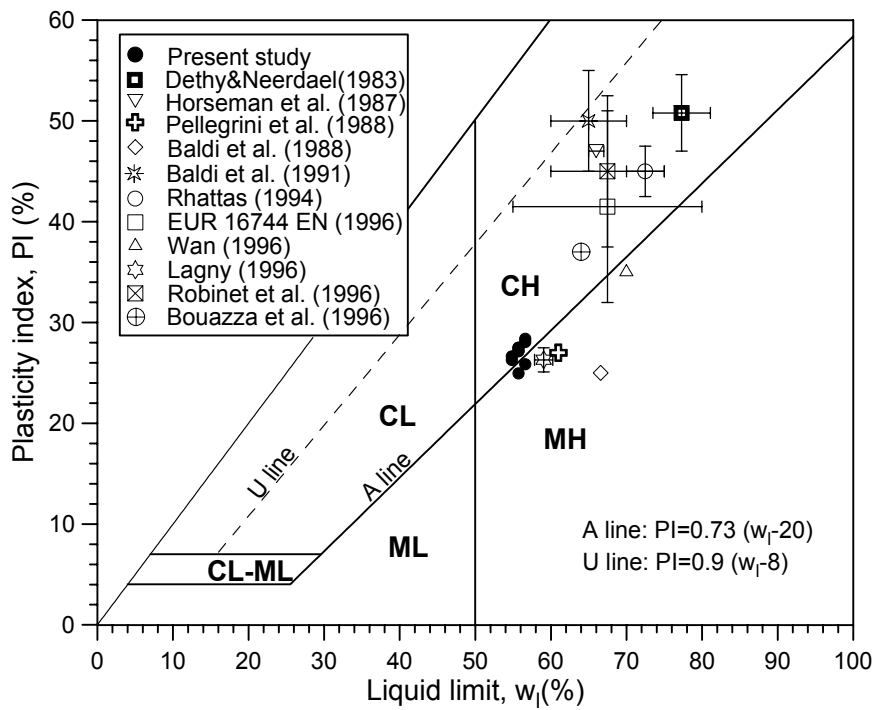
Figure 2.6   Plasticity chart.
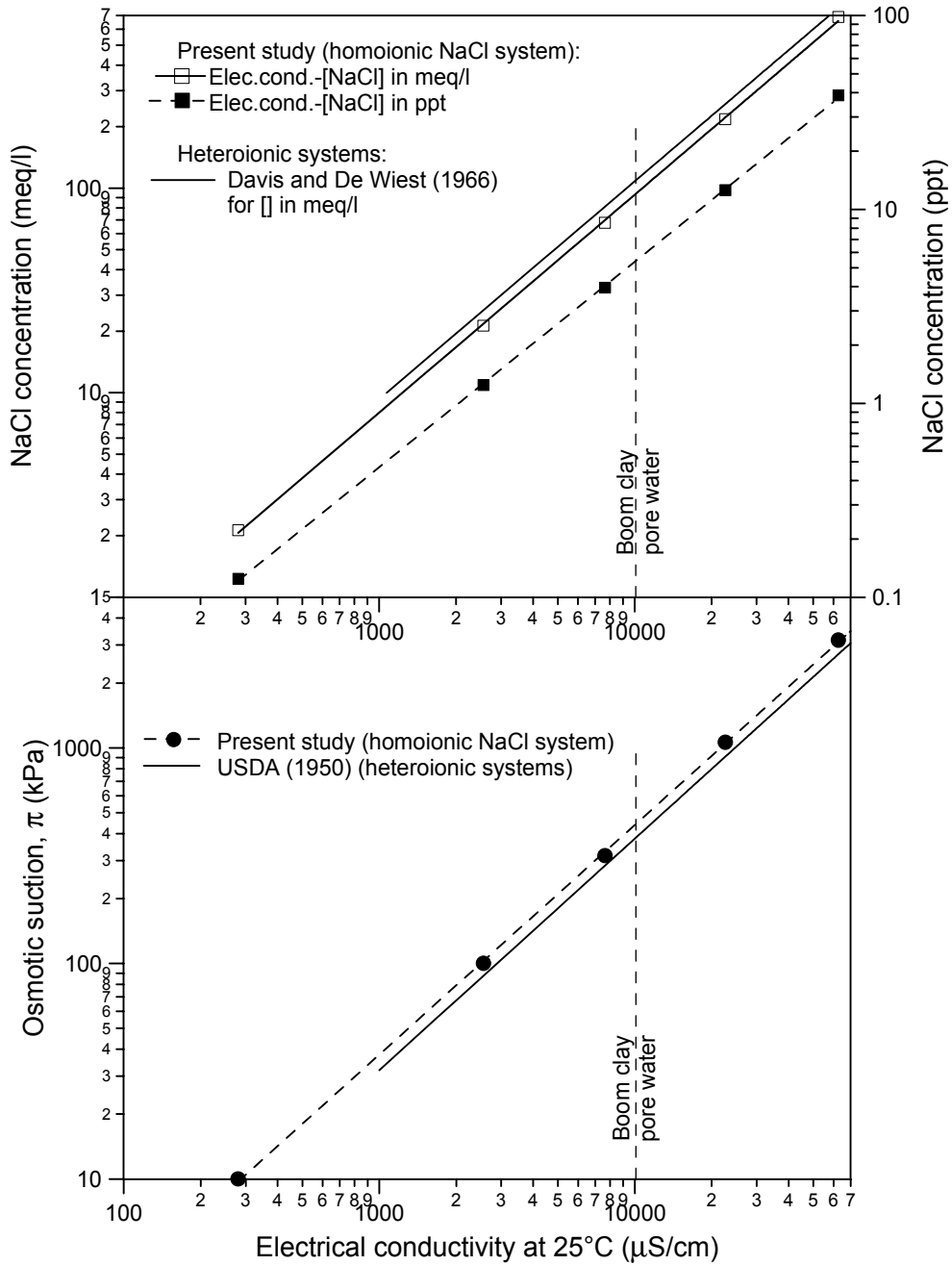
Figure 2.7   Relationship between electrical conductivity and solute concentration for homoionic (NaCl) and heteroionic systems.
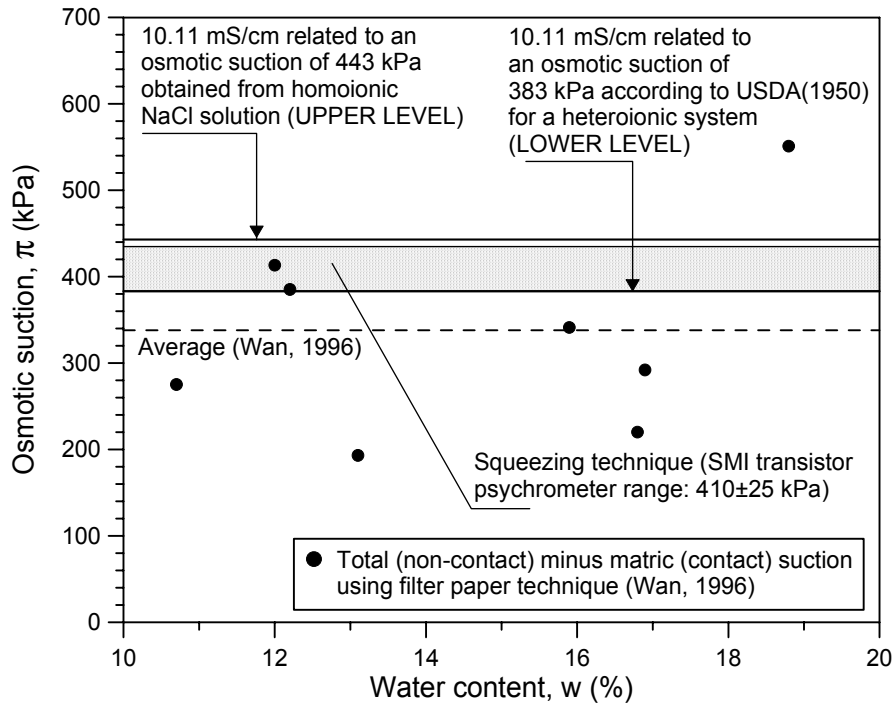
Figure 2.8 Psychrometric, electrical conductivity and filter paper techniques for osmotic suction measurement.
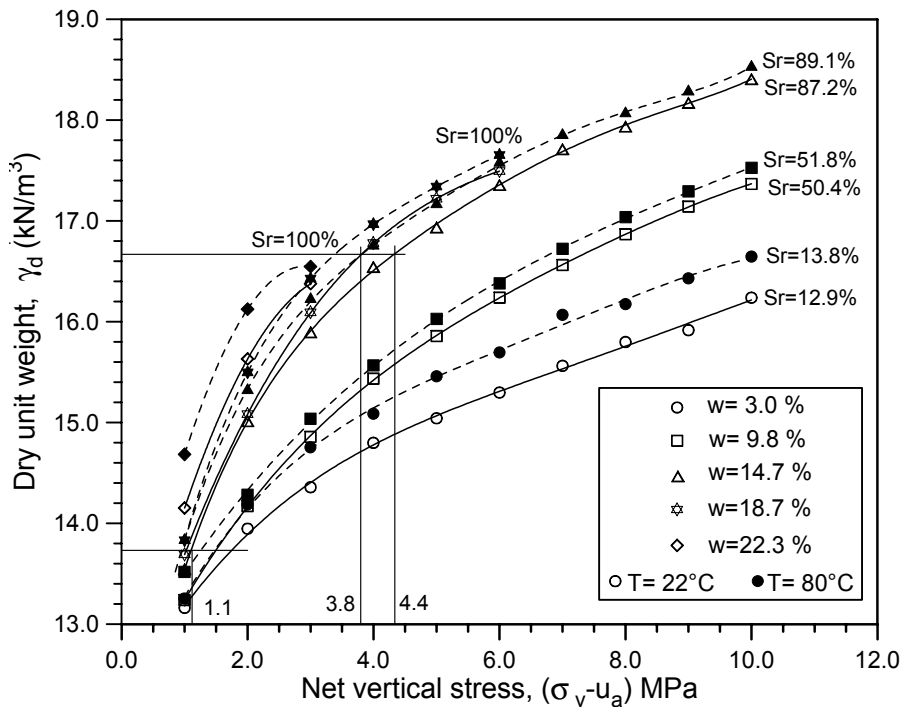
Figure 2.9   Net vertical stress against dry unit weight for different values of moisture content.
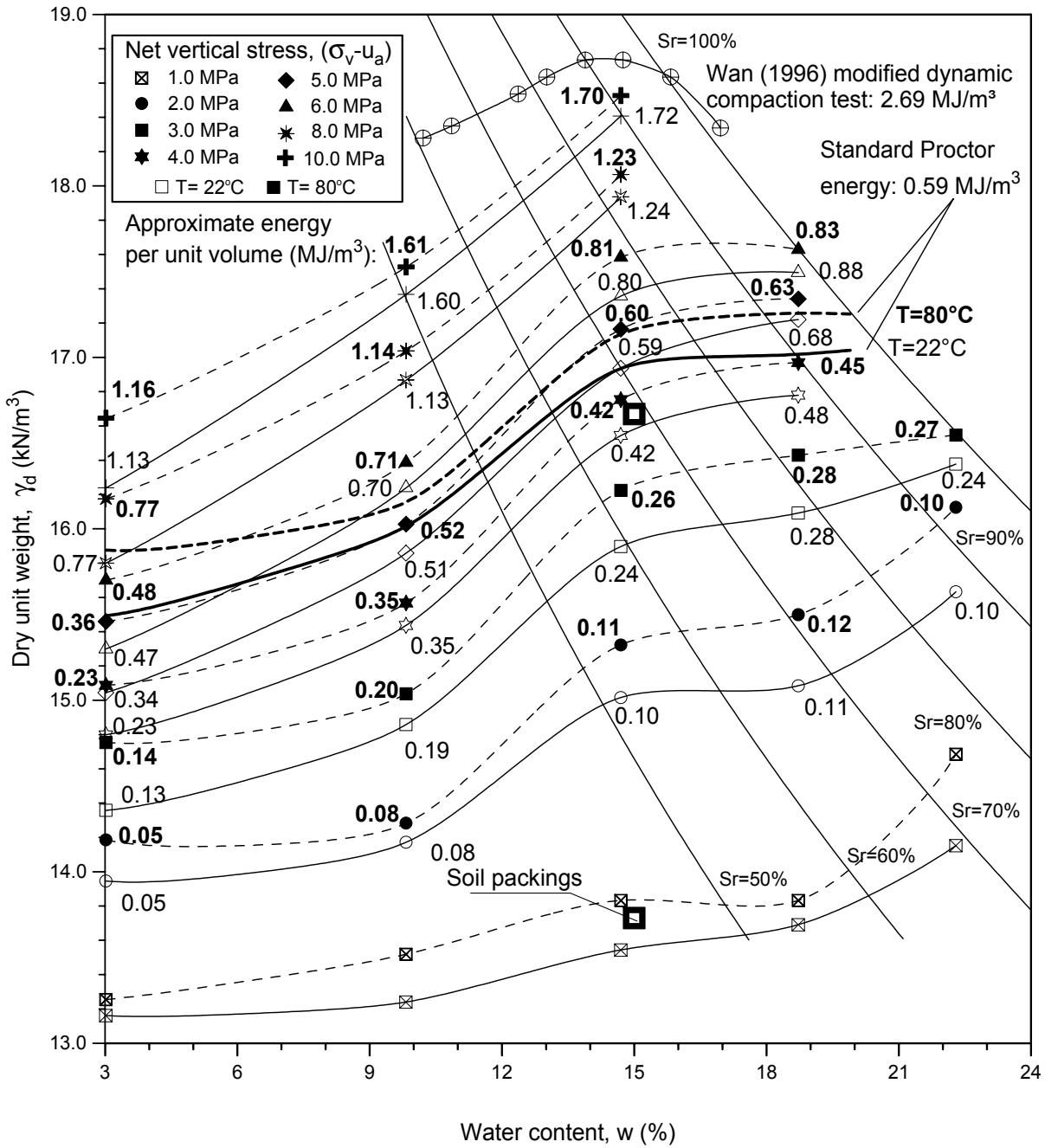
Figure 2.10   Static compaction curves for different stress levels. Energy input per unit volume.
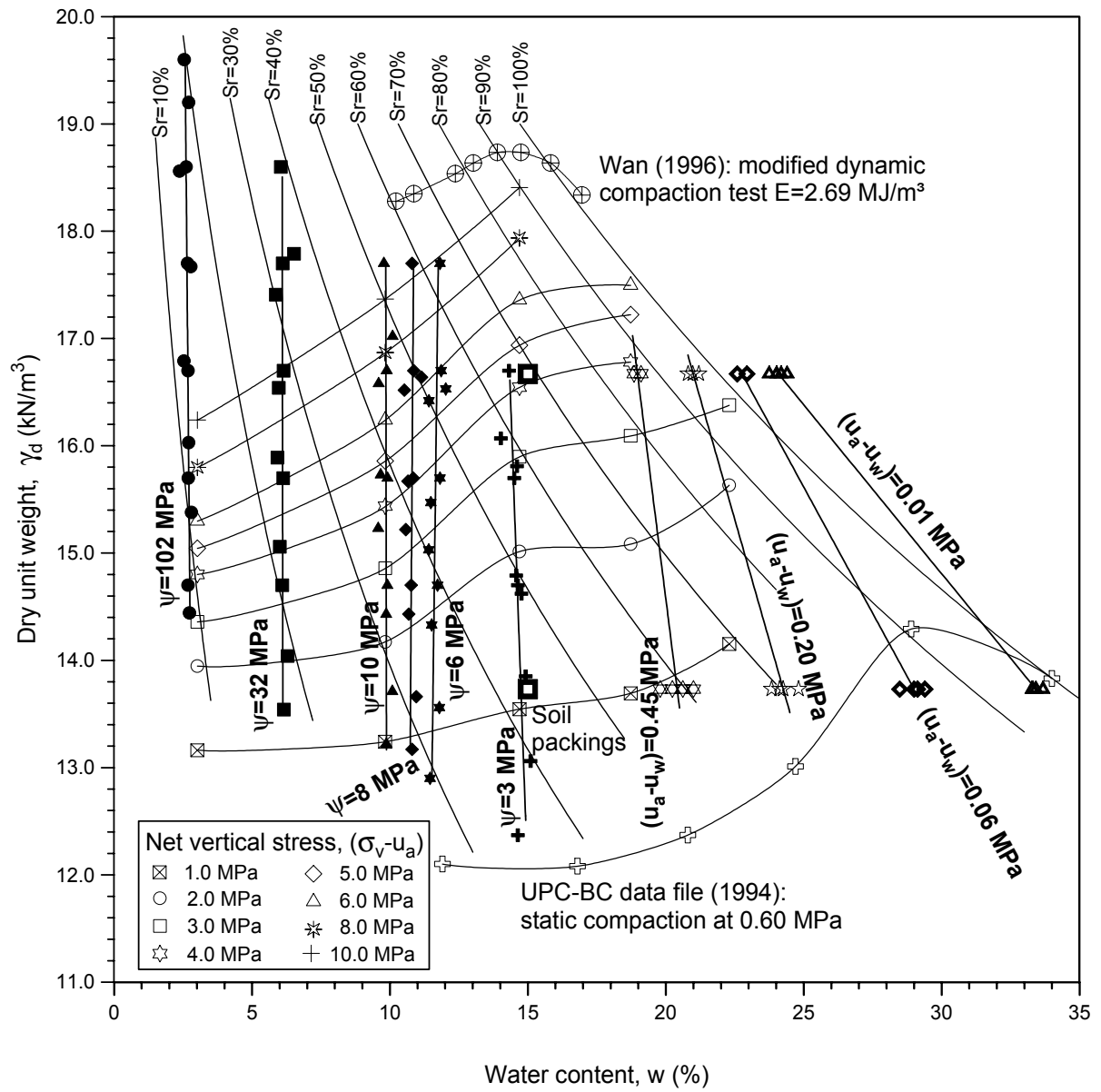
Figure 2.11 Static compaction curves with contours of equal suction.
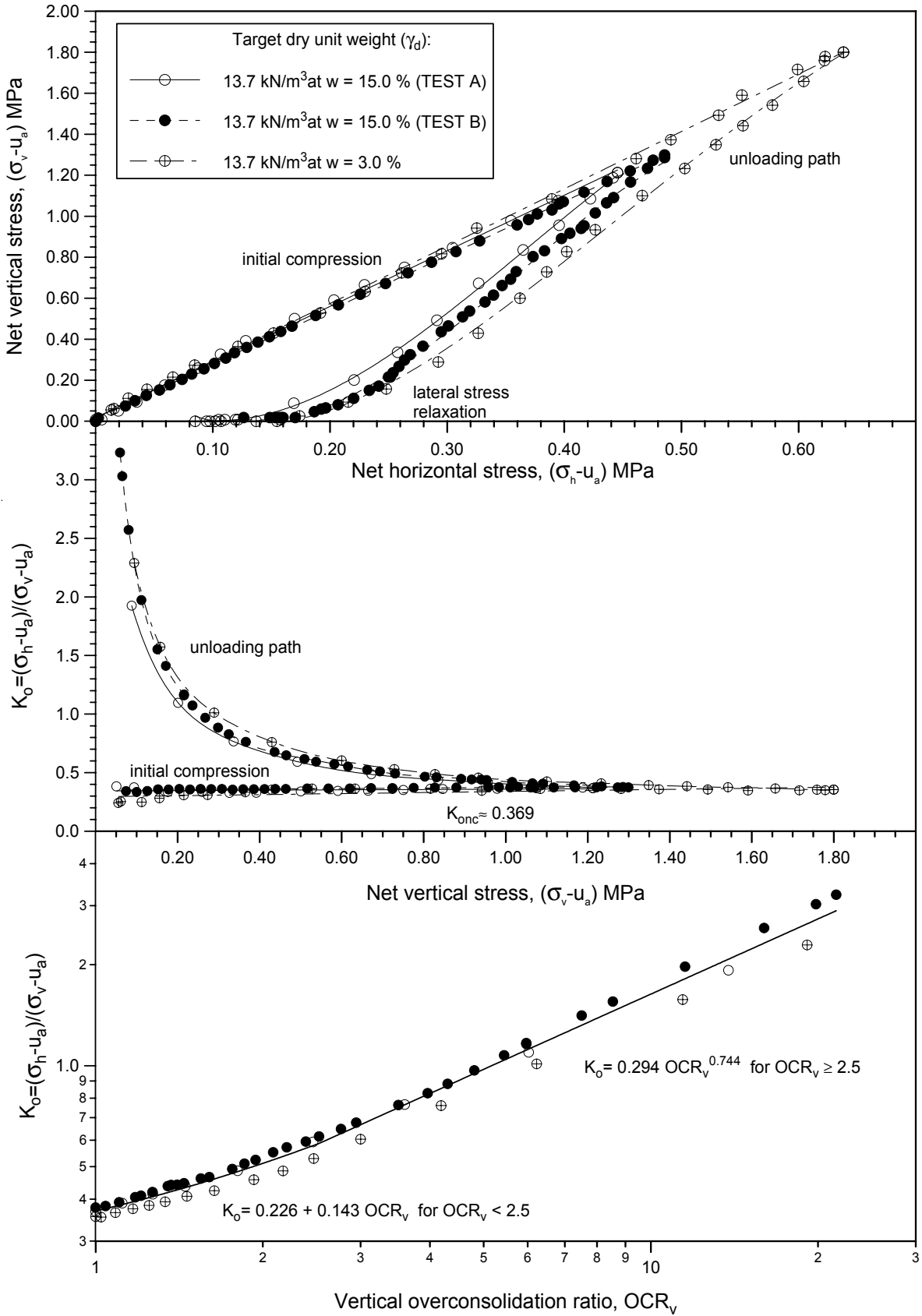
Figure 2.12   Stress paths followed by one-dimensional compression to a target $\gamma_d = 13.7$ kN/m^3. Relationship between K_0 and overconsolidation ratio.
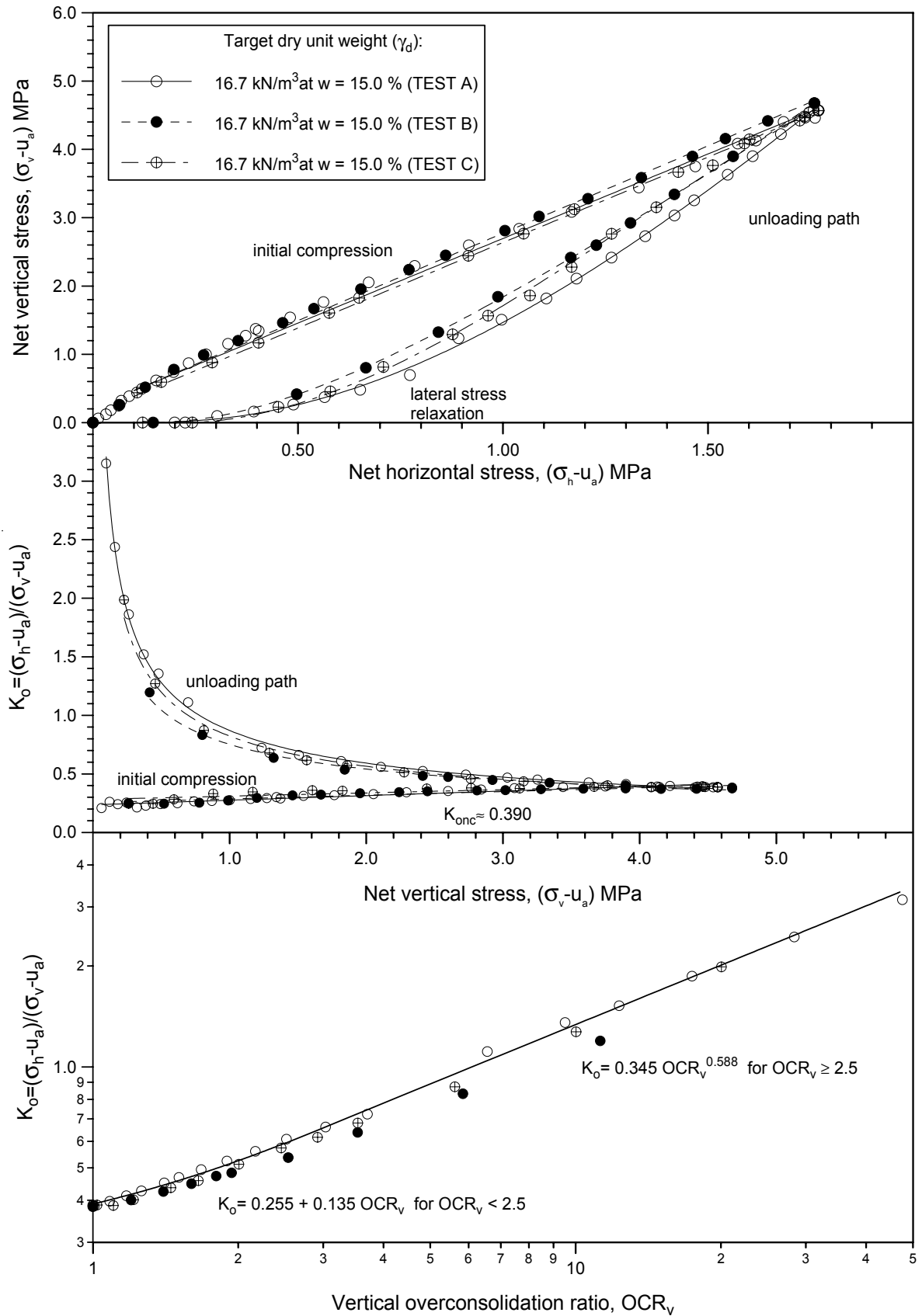
Figure 2.13 Stress paths followed by one-dimensional compression to a target $\gamma_d = 16.7$ kN/m^3. Relationship between K_0 and overconsolidation ratio.
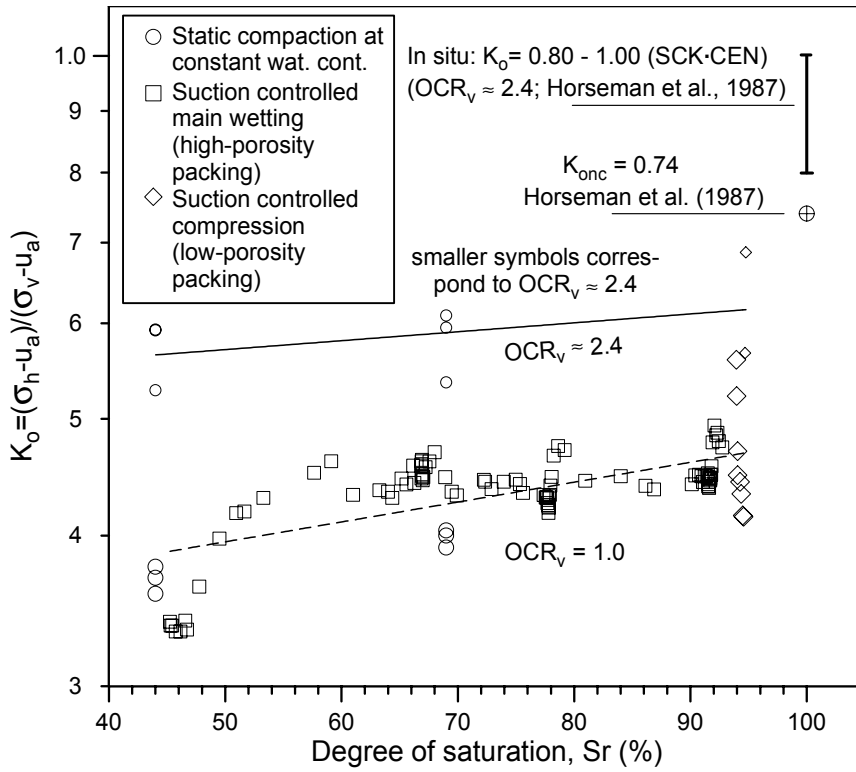
Figure 2.14 Relationship between K_0 and degree of saturation obtained from different test results. Extrapolation to in situ overconsolidation ratio.
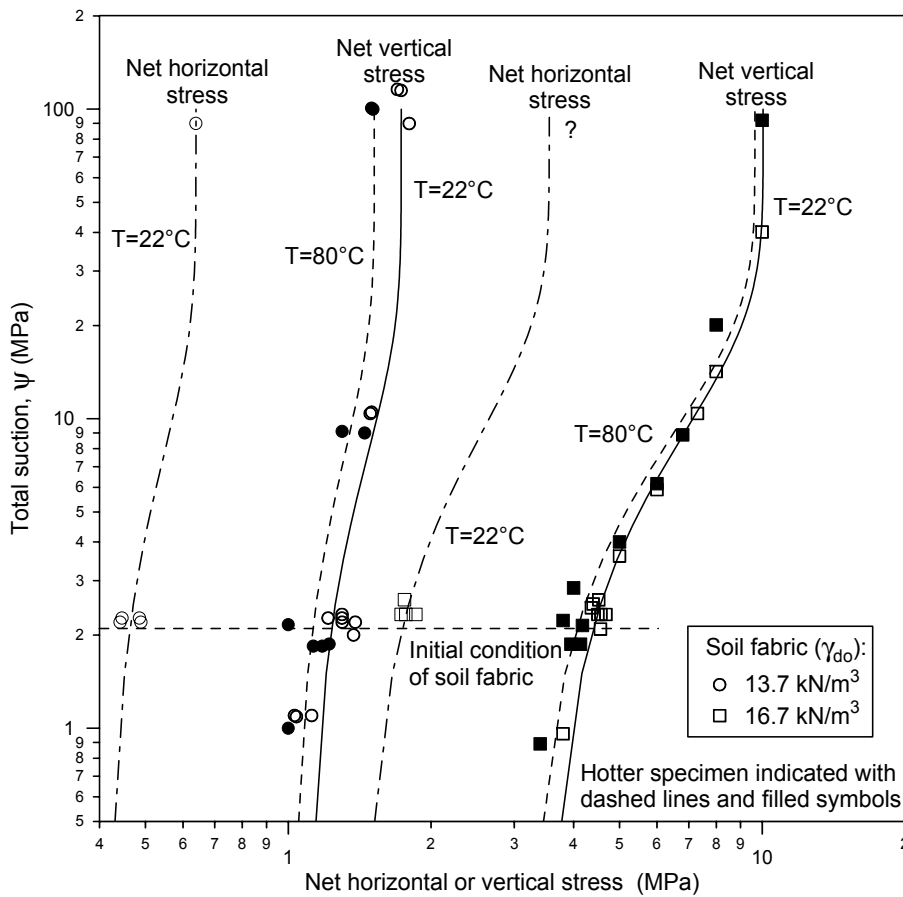
Figure 2.15   Suction - vertical and horizontal preconsolidation stress relationships obtained from static compaction tests at different temperatures.
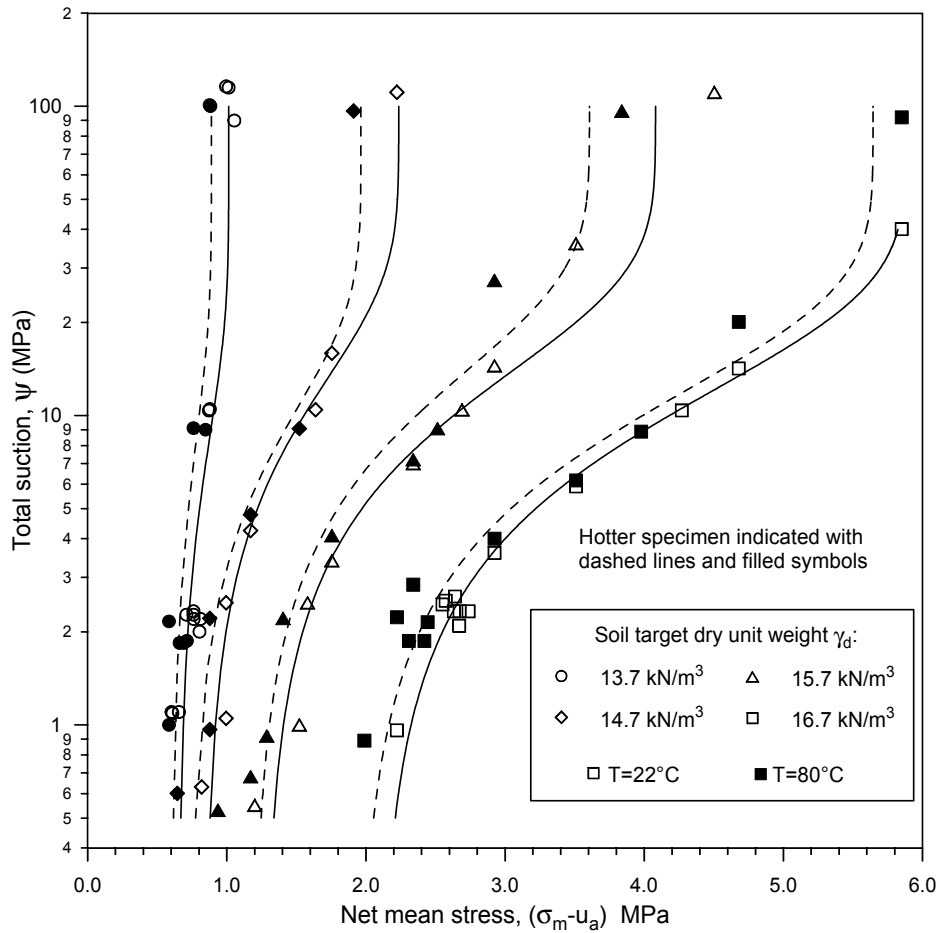
Figure 2.16 Suction-mean preconsolidation stress relationships obtained from static compaction tests at different temperatures.
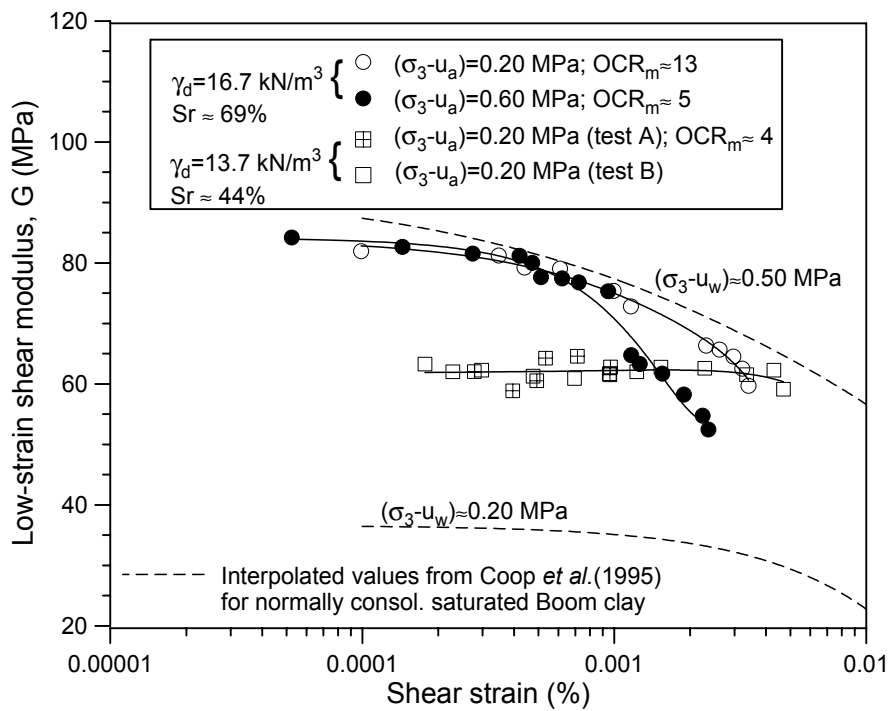
Figure 2.17 Variation of shear modulus with shear strain for the different packings obtained from resonant column tests.
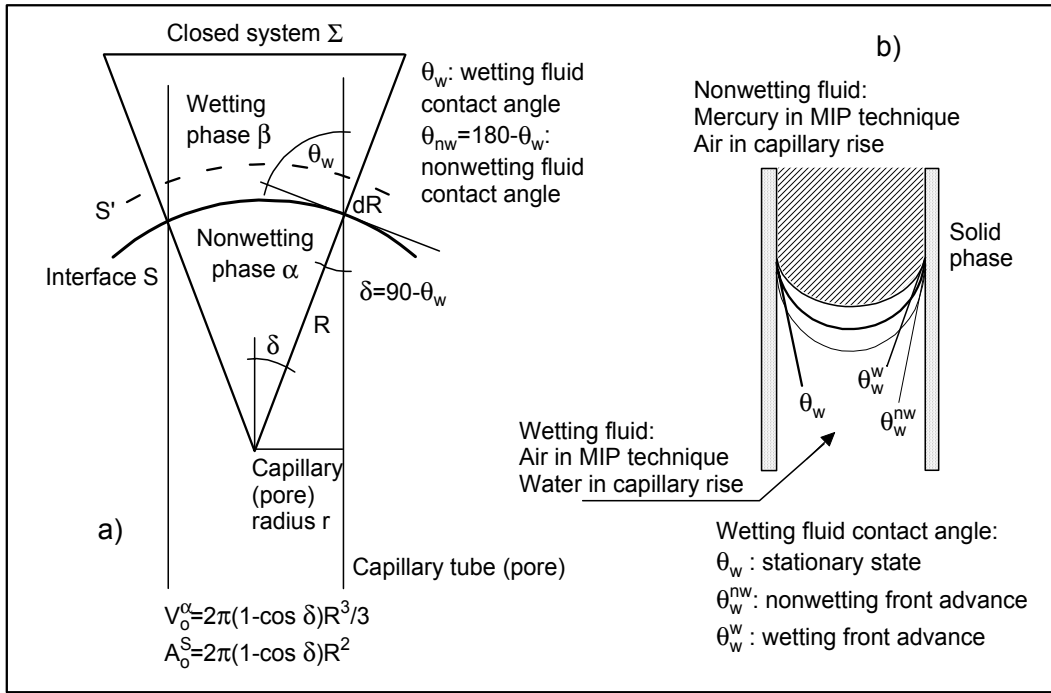
Figure 2.18   Surface phenomena in MIP technique and capillary rise.
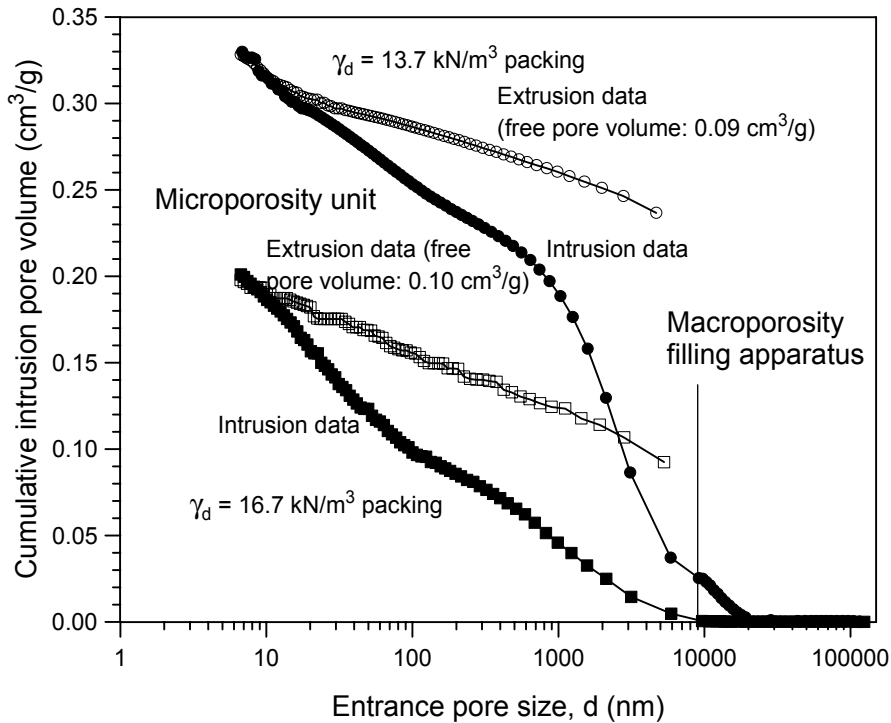
Figure 2.19   Cumulative intrusion pore volume normalised by sample weight.
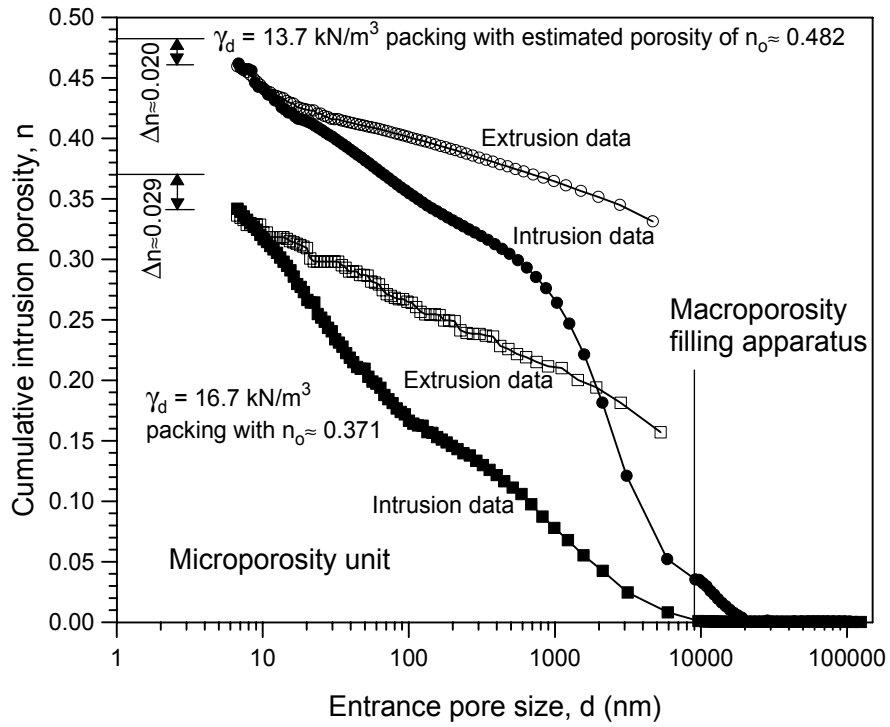
Figure 2.20   Cumulative intrusion porosity.
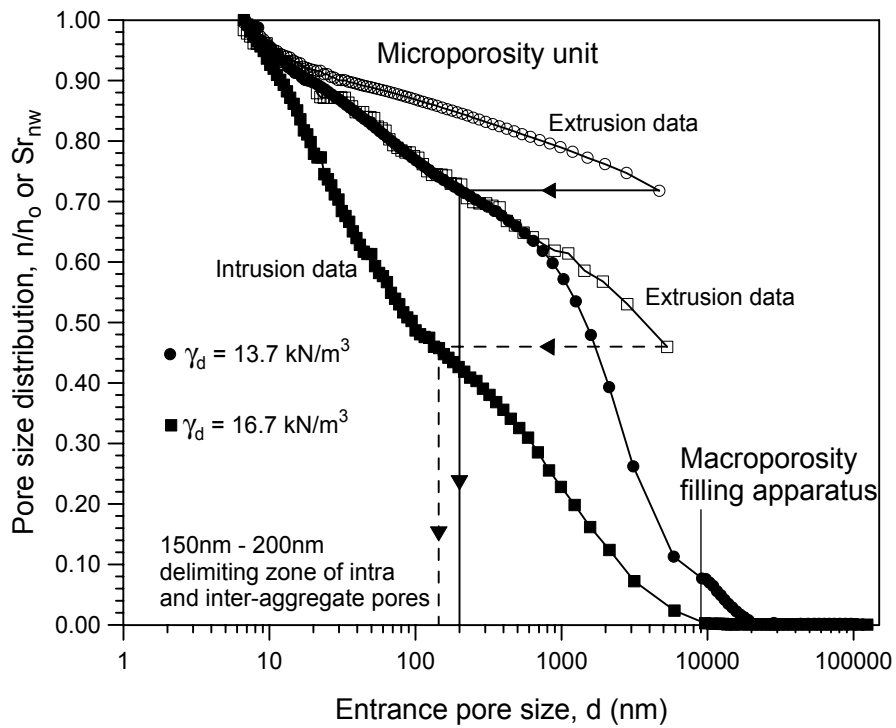
Figure 2.21   Pore size distribution for the different soil packings.
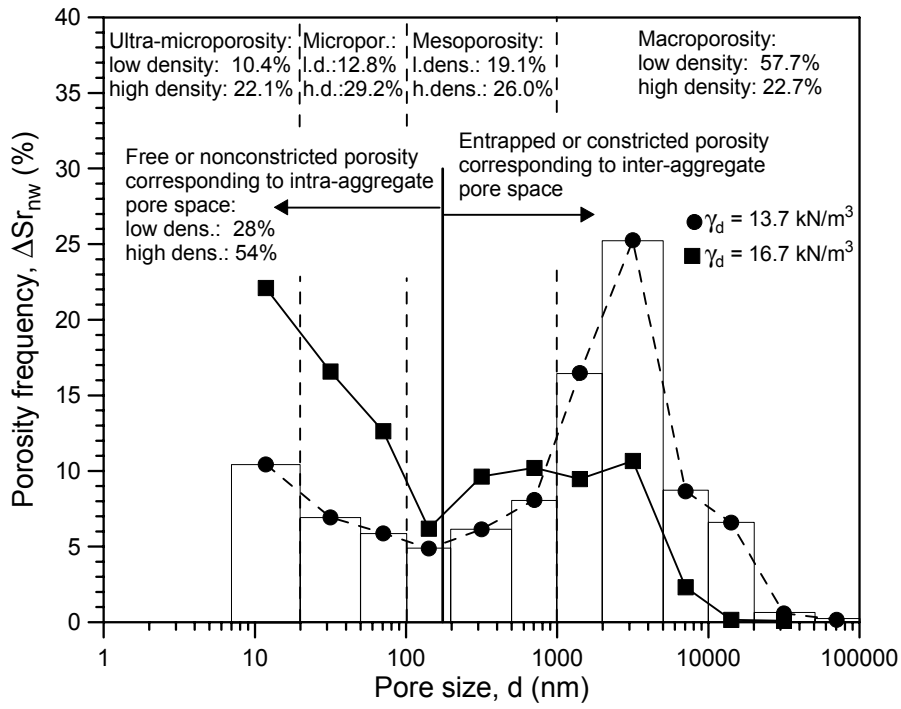
Figure 2.22   Relative porosity frequency (histogram) obtained from classified MIP results.
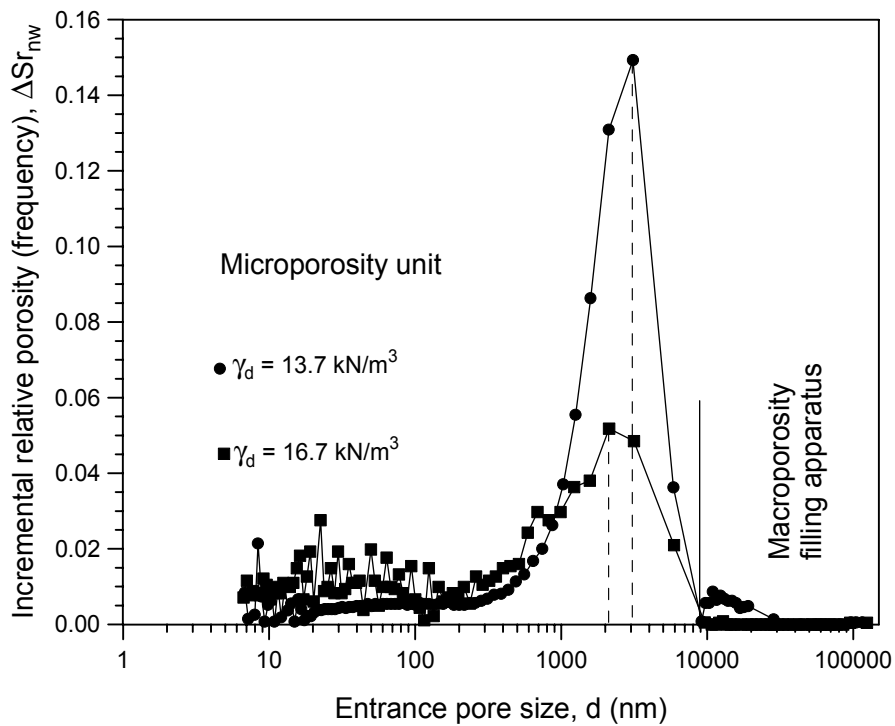
Figure 2.23   Incremental relative porosity (frequency) from MIP raw results.
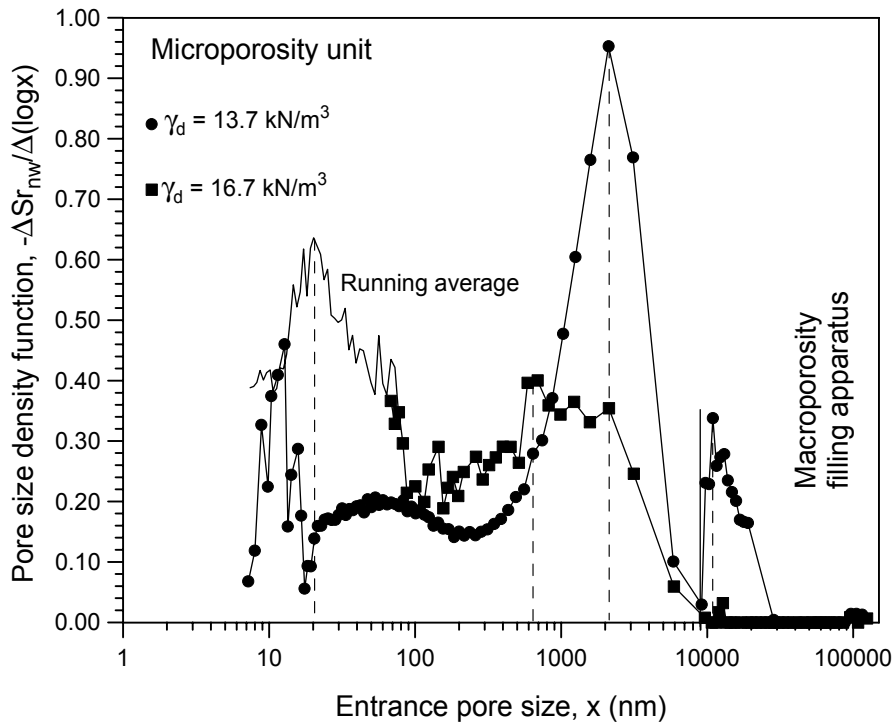
Figure 2.24   Pore size density function from MIP raw results.
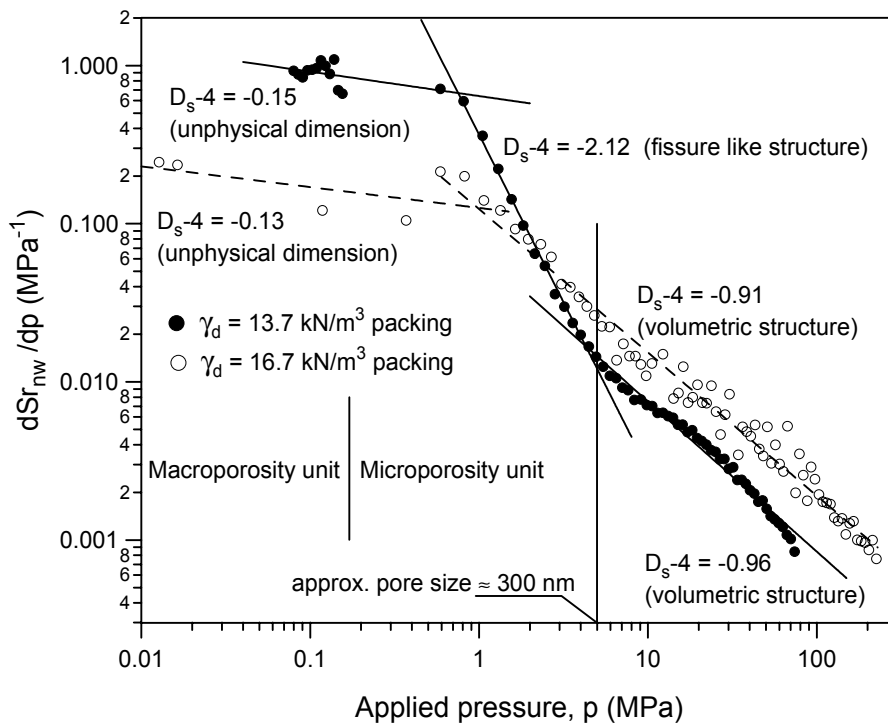
Figure 2.25   Determination of the fractal dimension from MIP raw results.
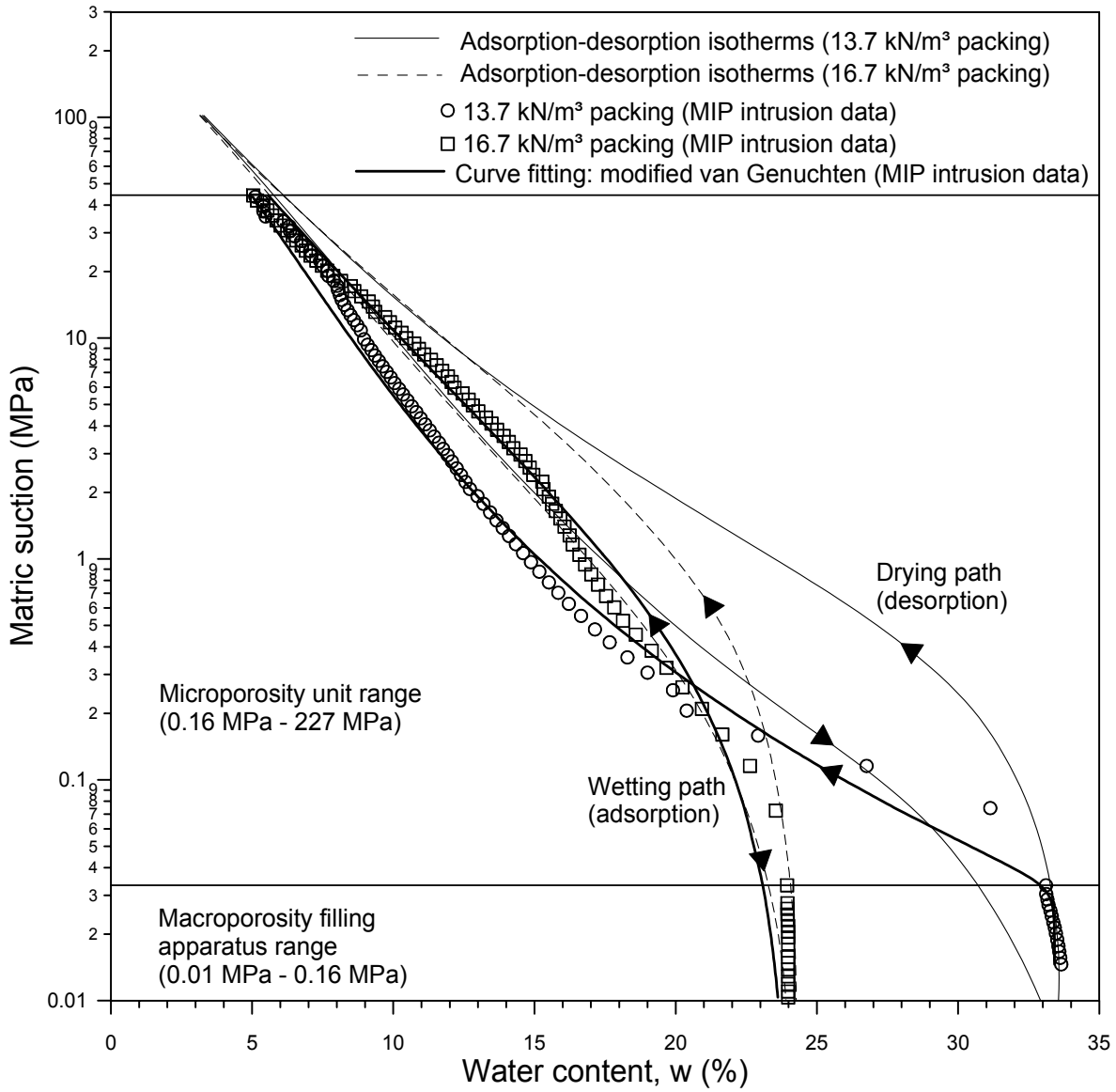
Figure 2.26 Adsorption and desorption isotherms for the different soil packings compared to MIP results.
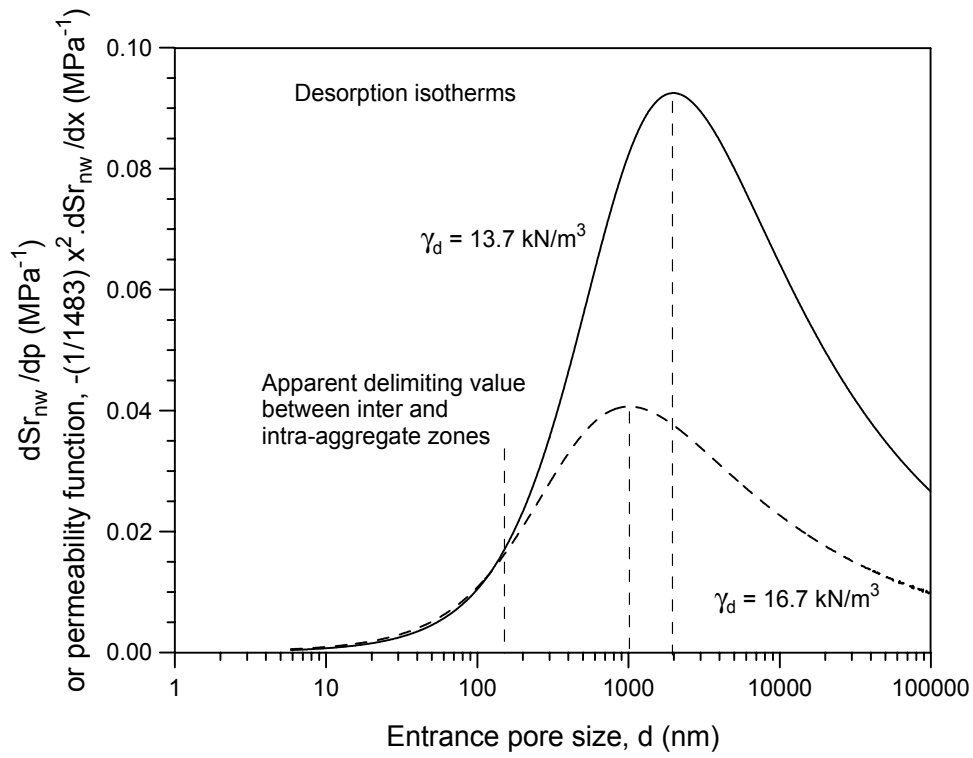
Figure 2.27 dSr_{nw}/dp function obtained from desorption isotherms. Apparent delimiting value separating inter and intra-aggregate zones.
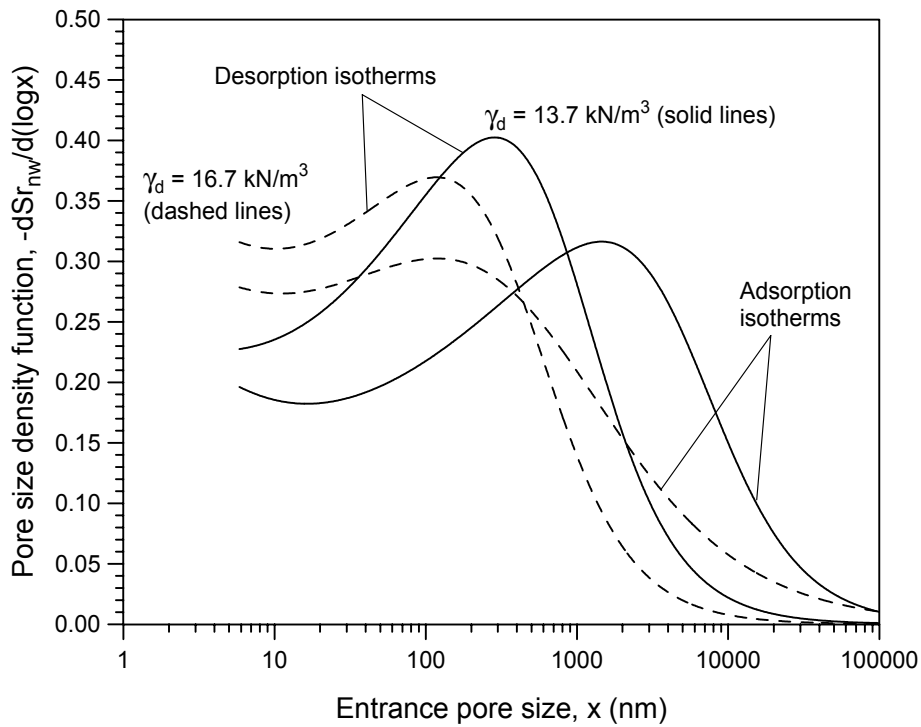
Figure 2.28 Pore size density function evaluated from retention curve data.
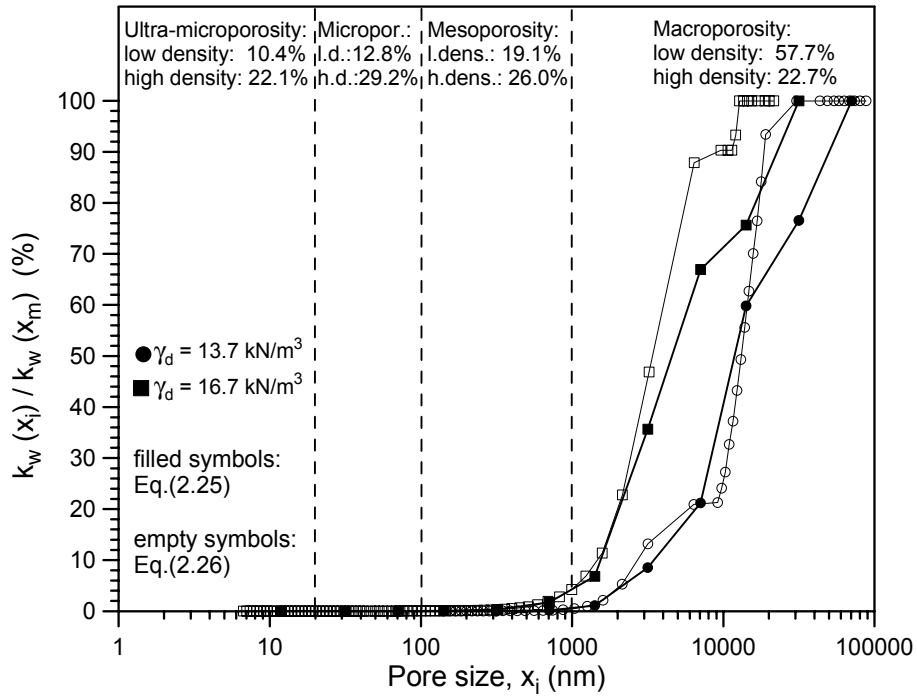
Figure 2.29   Relative permeability for different pore sizes evaluated from classified MIP data.
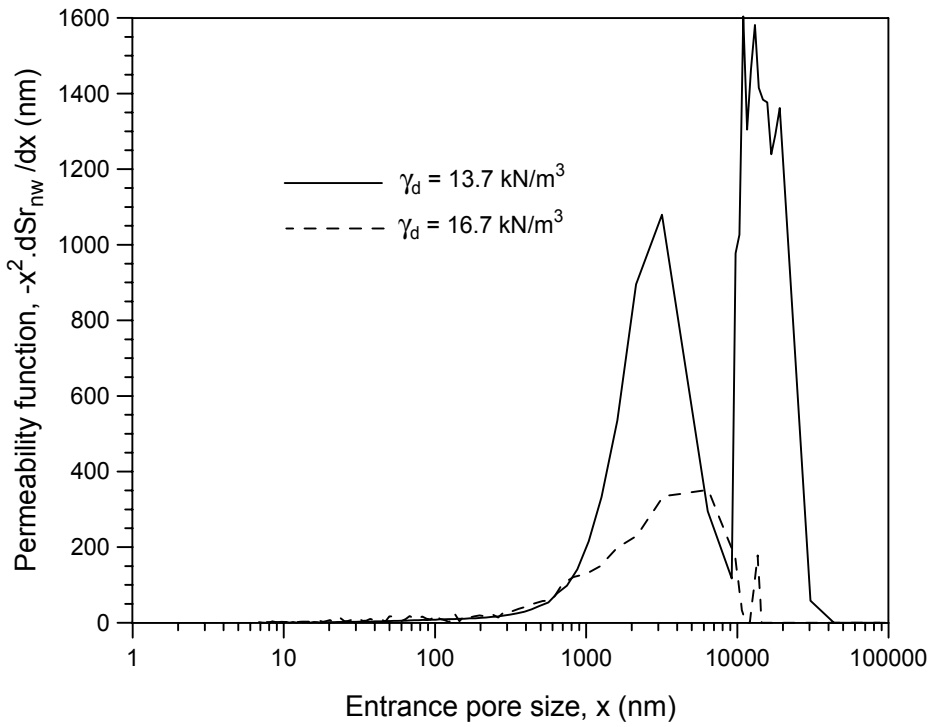
Figure 2.30   Permeability function evaluated from raw MIP data.

w=3%
$\gamma_d \approx 20.6$ kN/m^3
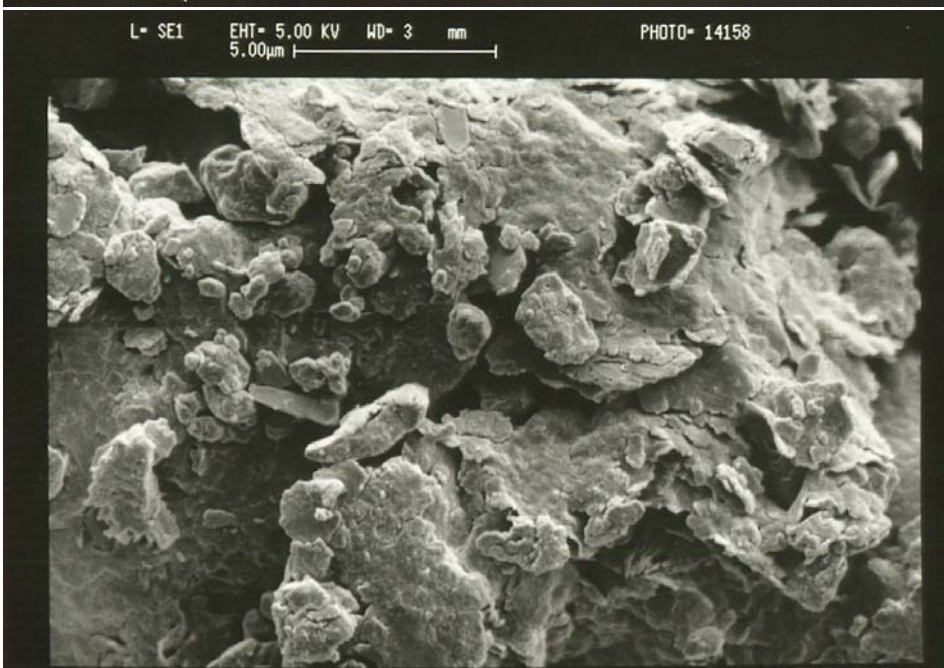
w=15%
$\gamma_d \approx 16.7$ kN/m^3
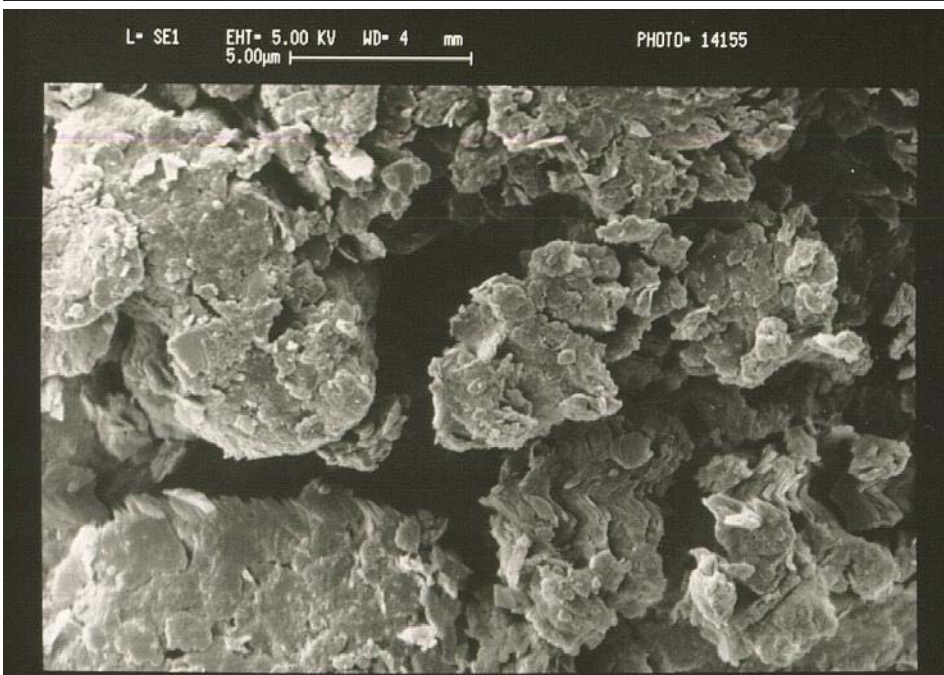
w=15%
$\gamma_d \approx 13.7$ kN/m^3

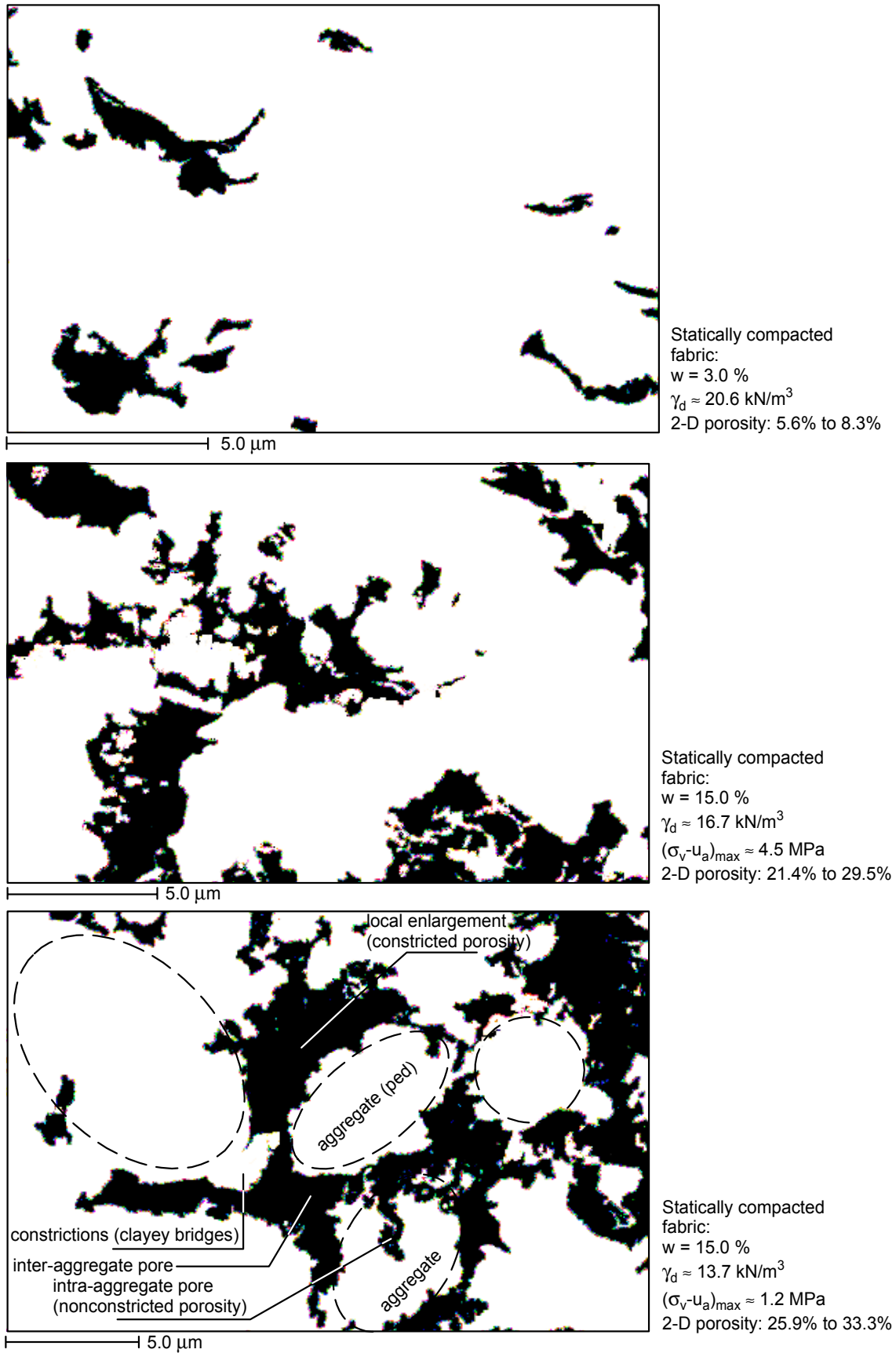Figure 2.31   SEM photomicrographs for different dry side compacted packings ($\times$ 5000).

Statically compacted
fabric:
w = 3.0 %
$\gamma_d \approx 20.6$ kN/m^3
2-D porosity: 5.6% to 8.3%

⊢———————⊣ 5.0 μm

Statically compacted
fabric:
w = 15.0 %
$\gamma_d \approx 16.7$ kN/m^3
$(\sigma_v\text{-}u_a)_{max} \approx 4.5$ MPa
2-D porosity: 21.4% to 29.5%

⊢———————⊣ 5.0 μm

local enlargement
(constricted porosity)

aggregate (ped)

constrictions (clayey bridges)
inter-aggregate pore
intra-aggregate pore
(nonconstricted porosity)

aggregate

Statically compacted
fabric:
w = 15.0 %
$\gamma_d \approx 13.7$ kN/m^3
$(\sigma_v\text{-}u_a)_{max} \approx 1.2$ MPa
2-D porosity: 25.9% to 33.3%

⊢———————⊣ 5.0 μm

Figure 2.32   Graphic representation of porosity changes for the different soil packings. Pores are black and particles white.
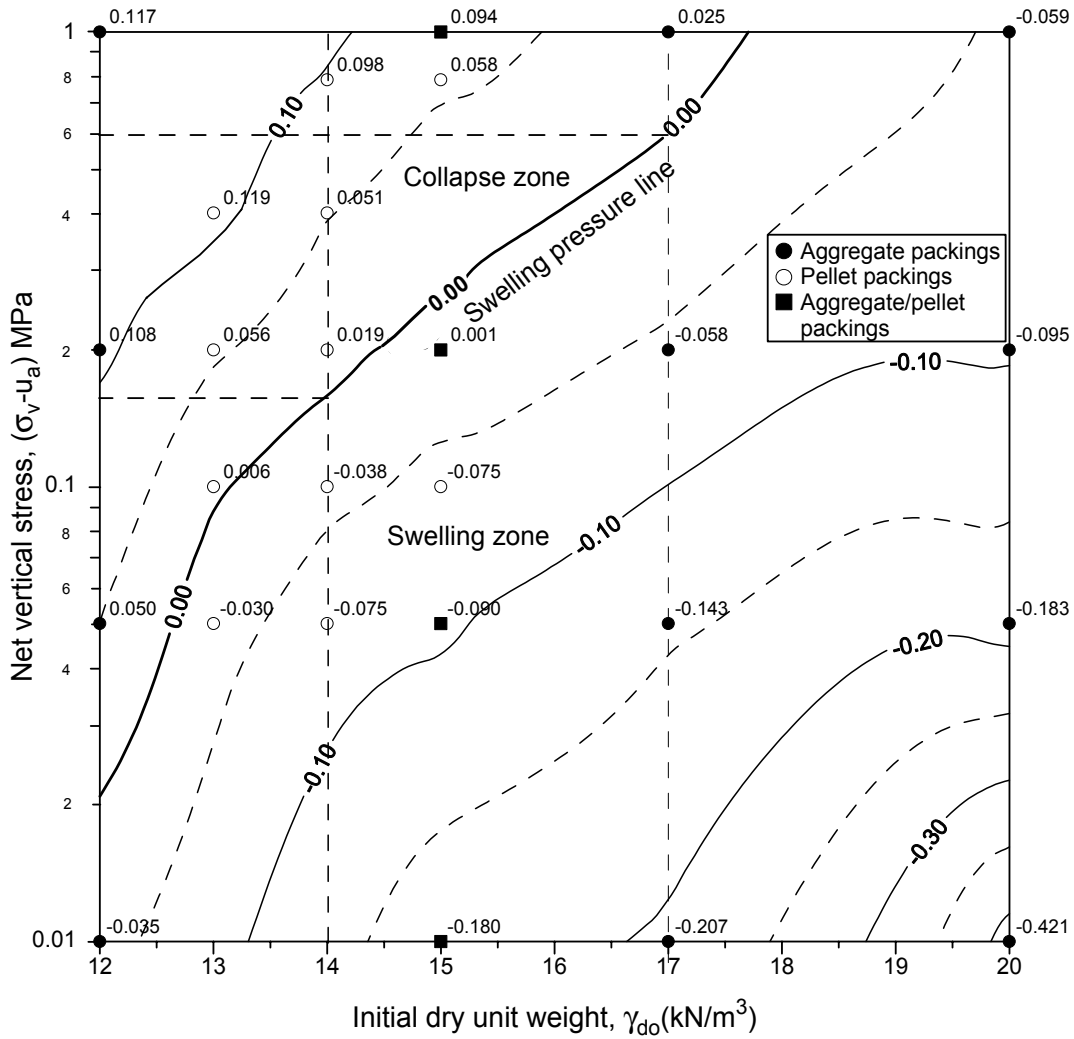
Figure 2.33 Vertical strains in soaking tests for different hygroscopic compacted packings.
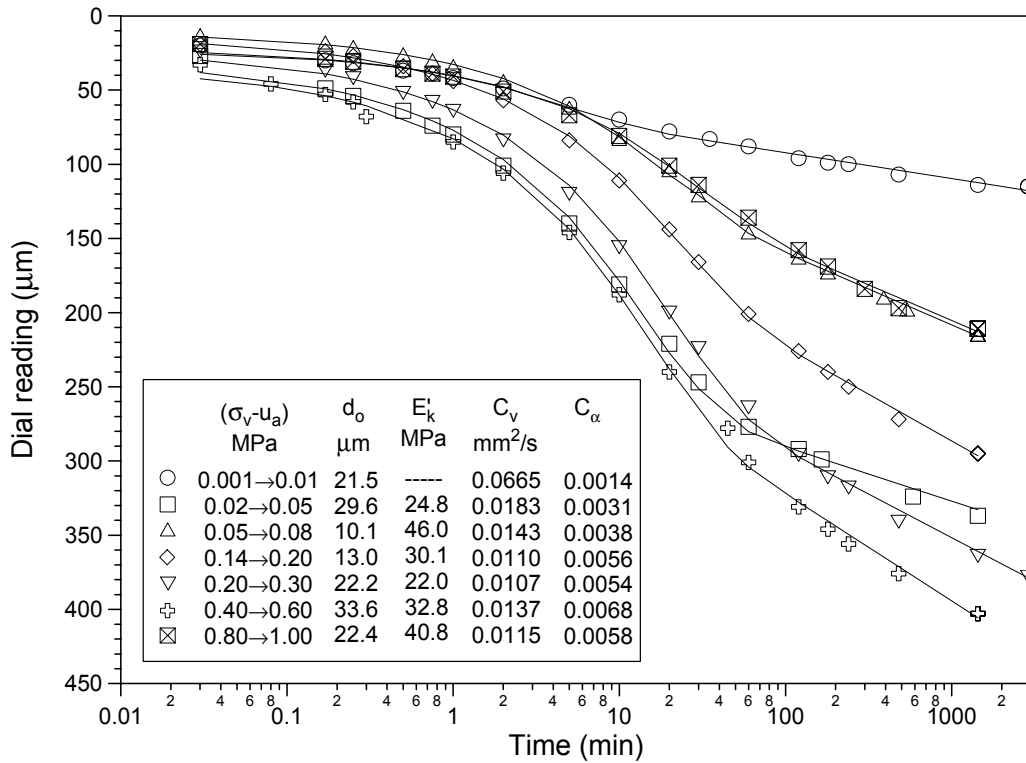

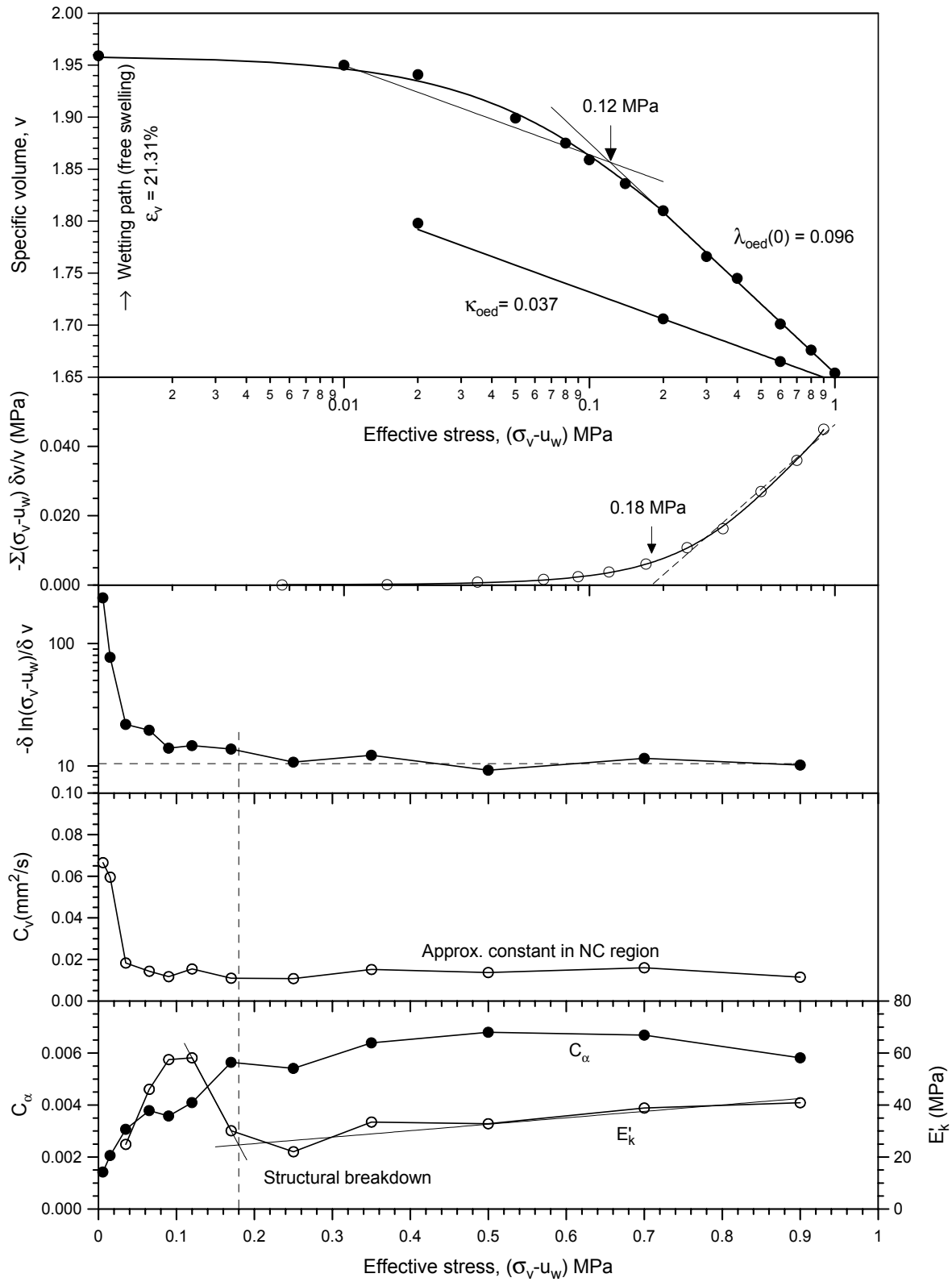Figure 2.34 Sample deformation vs. log(t) for different load increments. Curve fitting results.

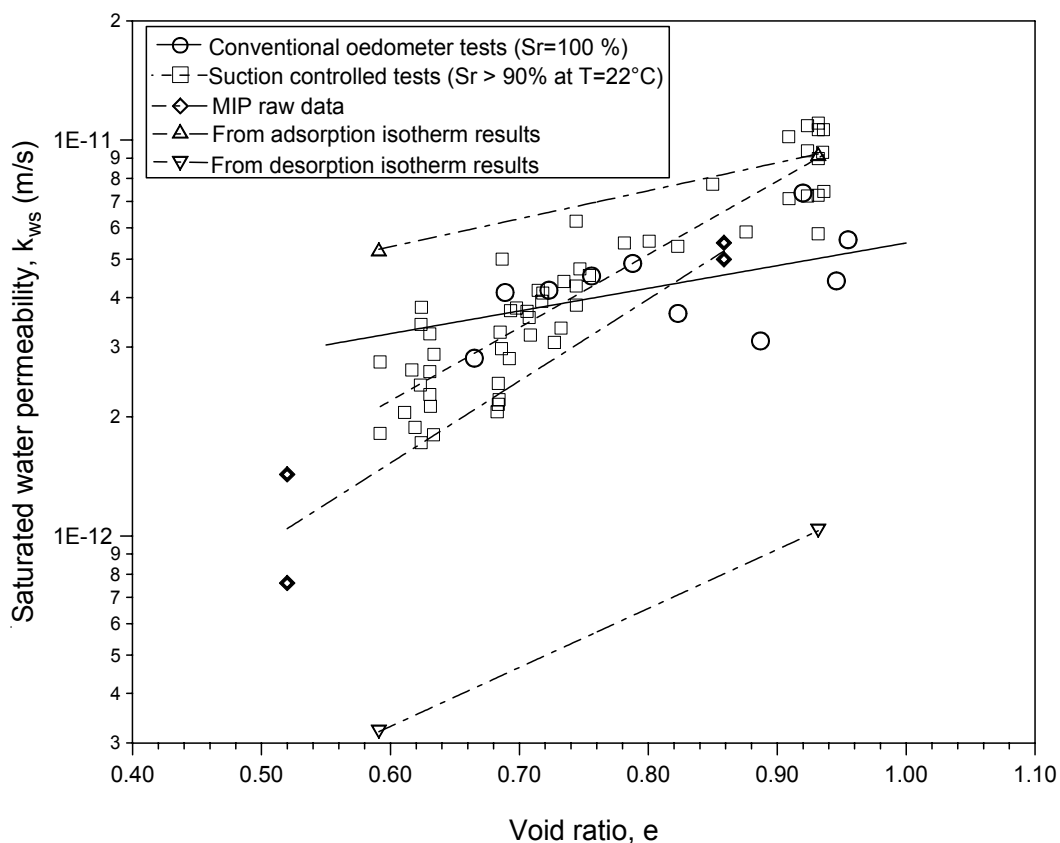Figure 2.35 Conventional oedometer loading-unloading path (saturated sample).

Figure 2.36 Saturated water permeability-void ratio relationship obtained from different testing procedures.
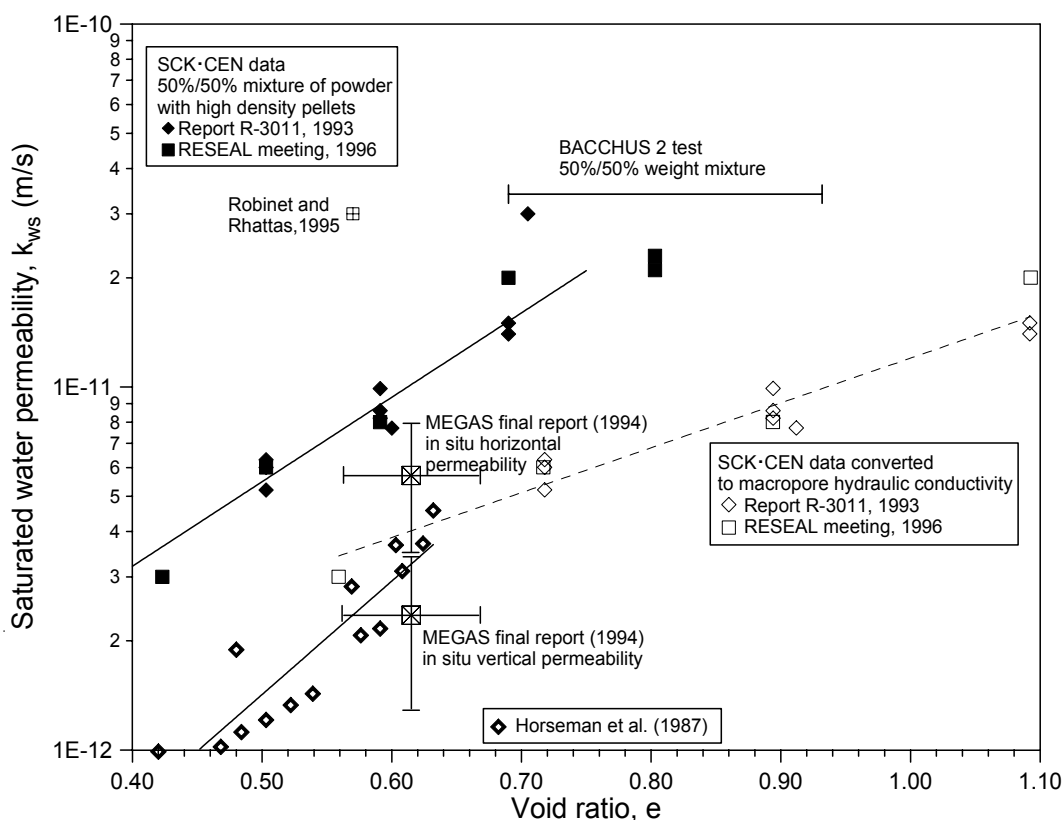

Figure 2.37 Different published results for saturated water permeability. Conversion to macroporosity void ratio.